

## EDITORIAL OFFICE

EDITOR-IN-CHIEF  
**Malcolm J. Crocker**

MANAGING EDITOR  
**Marek Pawelczyk**

ASSOCIATE EDITORS  
**Dariusz Bismor**  
**Nickolay Ivanov**  
**Zhuang Li**

ASSISTANT EDITORS  
**Teresa Glowka**  
**Sebastian Kurczyk**

EDITORIAL ASSISTANT  
**Lauren Harris**

## EDITORIAL BOARD

**Jorge P. Arenas**  
Valdivia, Chile

**Jonathan D. Blotter**  
Provo, USA

**Leonid Gelman**  
Cranfield, UK

**Samir Gerges**  
Florianópolis, Brazil

**Victor T. Grinchenko**  
Kiev, Ukraine

**Colin H. Hansen**  
Adelaide, Australia

**Hanno Heller**  
Braunschweig, Germany

**Hugh Hunt**  
Cambridge, England

**Dan Marghitu**  
Auburn, USA

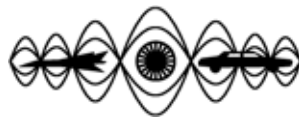
**Manohar Lal Munjal**  
Bangalore, India

**David E. Newland**  
Cambridge, England

**Kazuhide Ohta**  
Fukuoka, Japan

**Goran Pavic**  
Villeurbanne, France

**Subhash Sinha**  
Auburn, USA



# International Journal of Acoustics and Vibration

A quarterly publication of the International Institute of Acoustics and Vibration

Volume 20, Number 2, June 2015

## EDITORIAL

**From Environmental Noise Control to Soundscape Design**  
*Jian Kang* . . . . . 62

## ARTICLES

**A Comparison Between National Scheme for the Acoustic Classification of Dwellings in Europe and in the U.S.**  
*Umberto Berardi and Birgit Rasmussen* . . . . . 63

**A Vibration Energy Approach Used to Identify Temperature Trending in Railroad Tapered-Roller Bearings**  
*Constantine M. Tarawneh, Rafael K. Maldonado, Arturo A. Fuentes and Javier A. Kypuros* . . . . . 69

**Usage of Spectral Distortion for Objective Evaluation of Personalized HRTF in the Median Plane**  
*Fabian C. Tommasini, Oscar A. Ramos, Mercedes X. Hüg and Fernando Bermejo* . . . . . 81

**Stability of a Nonlinear Quarter-Car System with Multiple Time-Delays**  
*Raghavendra D. Naik and Pravin M. Singru* . . . . . 90

**Automatic Selection of the WPT Decomposition Level for Condition Monitoring of Rotor Elements Based on the Sensitivity Analysis of the Wavelet Energy**  
*Cristina Castejón, María Jesús Gómez, Juan Carlos García-Prada, Alberto Junior Ordoñez and Higinio Rubio* . . . . . 95

**Study of Automobile Suspension System Vibration Characteristics Based on the Adaptive Control Method**  
*Ruqiang Mou, Li Hou, Yiqiang Jiang, Yong Zhao and Yongqiao Wei* . . . . . 101

**Vibrations of Completely Free Rounded Regular Polygonal Plates**  
*C. Y. Wang* . . . . . 107

**About the Authors** . . . . . 113

## INFORMATION

**Book Reviews** . . . . . 118



## From Environmental Noise Control to Soundscape Design

---

Environmental noise, including sounds from road/rail/air traffic, industries, construction, public work, and the neighbourhood, is often a main cause of environmental distress in terms of the number of complaints received. The publication of the EU Directive Relating to the Assessment and Management of Environmental Noise (END) in 2002 has led to a number of major actions, including the large-scale noise mapping for major sources and cities across Europe and the identification and protection of quiet areas. It is widely accepted that reducing the sound level is not always feasible and cost-effective, and more importantly, it will not necessarily lead to improved quality of life and people's satisfaction. For example, studies in urban open spaces have shown that when the sound level is below a certain value (as high as 65-70 dB), people's acoustical comfort is not related to the sound level, whereas the non-acoustical factors such as the type of sound sources and characteristics of users play an important role.

Soundscape research, different from noise control engineering, is about relationships between the ear, human beings, sound environments, and society. Research in soundscape covers physical science, engineering, social science, humanity, medicine, and art. It has been mainly developed within the academic disciplines of anthropology, architecture, ecology, design, human geography, linguistics, medicine, noise control engineering, psychology, sociology, and more recently, computer simulation and artificial intelligence. As a global concept, it may also be fruitful to integrate insights from knowledge or values produced by every culture, therefore involving literature and musicology, and more generally, art, aesthetics, law, and religious studies as well. Soundscape research represents a timely paradigm shift in that it considers environmental sound as a 'resource' rather than a 'waste'. It is more powerful than the classic level-based approach, which is only suitable for providing primary needs such as sleep and hearing protection. It becomes even more prominent when a society reaches the highest needs: respect for others and creativity and spontaneity. Soundscape focuses more on the local individual needs and has esteem for those sensitive to noise and other vulnerable groups. It also has ear for cultural aspects and the beauty of natural soundscapes.

Although the term soundscape was introduced in the 1960s, soundscape has mainly received attention in the field of community noise and environmental acoustics by researchers, and

recently by policy makers, in the last decade. The number of people in the field/sector and the number of publications is steadily growing. In recent major international conferences, a considerable number of special sessions on soundscape research have been organised. The importance of soundscape research has been recognised by governmental organisations and national funding bodies, and a series of research projects relating to this field have been, and are being, carried out. There have also been increasing interests in practice, and many cities are currently actively promoting practical exemplar soundscape projects. In addition, the soundscape approach has been applied to preserve and restore archaeological places of great importance where the tourist sensation shall be globally connected to the atmosphere of the historic site.

The recent EU COST Action on Soundscape of European Cities and Landscapes aimed to provide the underpinning science and practical guidance in soundscape, and it has created a vibrant/productive international network of 52 participants from 23 COST countries and 10 participants outside Europe. Five aspects are covered, including understanding and exchanging, collecting and documenting, harmonising and standardising, creating and designing, and outreaching. In the meantime, a working group ISO/TC43/SC1/WG54 was formed in 2008 on the perceptual assessment of soundscape quality, and the Part 1 of this ISO standard, Definition and Conceptual Framework, was published in 2014, where soundscape is defined as 'acoustical environment as perceived or experienced and/or understood by a person or people, in context'.

Although considerable work has been carried out, further research is still needed in more facets; for example, the current research works in soundscape are still in the stage of describing and identifying the problems, and they tend to be fragmented and focused on only a few special cases. In the meantime, large scale practical implementation of the research work has yet to start.

**Jian Kang**  
**Director, IIAV**

---

---

# A Comparison Between National Scheme for the Acoustic Classification of Dwellings in Europe and in the U.S.

**Umberto Berardi**

*Department of Architectural Science, Faculty of Engineering and Architectural Science, Ryerson University, 350 Victoria St, Toronto, ON M5B 2K3, Canada*

**Birgit Rasmussen**

*Danish Building Research Institute, Aalborg University (AAU-CPH), A.C. Meyers Vnge 15, 2450 Copenhagen SV, Denmark*

(Received 20 April 2014; accepted 18 February 2015)

The classification of dwellings according to different building performances has been proposed through many schemes worldwide in recent years. The general idea behind these schemes relates to the positive impact a higher label, and thus a better performance, should have. In particular, focusing on sound insulation performance, national schemes for sound classification of dwellings have been developed in several European countries. These schemes define acoustic classes according to different levels of sound insulation. Due to the lack of coordination among countries, a significant diversity in terms of descriptors, number of classes, and class intervals occurred between national schemes. However, a proposal "acoustic classification scheme for dwellings" has been developed recently in the European COST Action TU0901 with 32 member countries. This proposal has been accepted as an ISO work item. This paper compares sound classification schemes in Europe with the current situation in the United States. Economic evaluations related to the technological choices necessary to achieve different sound classification classes are also discussed. The hope is that a common sound classification scheme may facilitate exchanging experiences about constructions fulfilling different classes, reducing trade barriers, and finally increasing the sound insulation of dwellings.

---

## 1. INTRODUCTION

Recent research has proven how sound insulation deeply correlates with productivity, higher learning outcomes, and concentration.<sup>1-3</sup> However, beyond annoyance or decreased productivity, poor acoustical environments also affect health. The World Health Organization has repeatedly linked the population's exposure to environmental noise with adverse health effects and has established a relationship between traffic noise and an increased risk of cardiovascular diseases.<sup>4,5</sup> At the same time, an emerging body of research has linked the exposure to environmental noise with sleep disturbance, cognitive impairment in children, and Tinnitus, among other human health concerns.<sup>4,6</sup> All of these studies show that the indoor acoustic performance deeply matters for the quality of the built environment.

The majority of countries in Europe have a long tradition of regulatory sound insulation requirements for dwellings, going back to the 1950s in some cases.<sup>7,8</sup> The purpose of these regulations is the protection of health. However, the fulfilment of these requirements does not ensure satisfactory conditions, and the protection is typically insufficient for sensitive persons or in the case of loud neighbours. For this reason, classification schemes have been introduced in several countries to specify higher levels of acoustical comfort. The first classification schemes for dwellings were implemented in the early 1990s.<sup>8</sup> A scheme generally defines a number of classes according to a certain interval of some acoustic indicators that are used to reflect different levels of acoustic comfort.

Findings from comparative studies of regulatory sound insulation requirements and sound classification schemes in Europe show that sound insulation descriptors, regulatory requirements, and classification schemes have a high degree of diversity.<sup>9-11</sup> These studies have concluded that harmonization is needed to facilitate the exchange of data and experience among countries and to reduce trade barriers.

This paper considers that sound insulation requirements are a national issue that cannot be made homogenous worldwide. However, the comparison of the ongoing experience towards a harmonized European classification scheme with the situation in the U.S. would help building stakeholders to familiarize with acoustic classes fitting local needs and conditions.

## 2. CLASSIFICATION SCHEMES IN EUROPE

### 2.1. Existing Sound Classification Schemes in Europe

A sound classification scheme could be defined as a set of a minimum of three classes with different sound insulation performance levels. Using this definition, classification schemes for dwellings exist, at present, in ten countries in Europe.<sup>8</sup> Sound classification schemes indicate different quality classes to meet different needs of activities and quietness.<sup>10</sup> They have generally been developed as technical standards, but sometimes they are already referred to in national laws.

Acoustic class information could be considered as an analogy to energy labelling or other labelling systems. In fact, any

acoustic classification scheme allows specifying acoustic conditions in a way that is similar to other qualities.

Sound classification systems in Europe are national schemes, the majority of which have been published by national standard organizations.<sup>11</sup> An overview of existing sound classification schemes for dwellings is reported in Table 1. For each scheme, information is found about class denotations, relation to the national building code, and classes intended for new and for existing (old, renovated, and other not new) housing, respectively. The schemes specify class criteria concerning several acoustic aspects. These are described in more detail in recent publications for party walls and floors between dwellings<sup>8</sup> and for facades.<sup>10,12</sup>

An international standard or technical specification would help improving awareness, knowledge and communication about the quality of acoustic conditions and hopefully improve housing stock. With this idea, a proposal "acoustic classification scheme for dwellings" has been developed recently in the European COST Action TU0901 with 32 member countries,<sup>13</sup> and the proposal has been accepted as an ISO work item.<sup>14</sup> Table 2 reports a preliminary proposal within this ISO work item. Although the work is just started in the ISO working group and changes will certainly occur, based on the COST action results, Table 1 shows a preliminary classification currently discussed. While several of the national classification schemes also include other building types than housing, the proposed ISO scheme is for housing only.

## 2.2. The COST TU0901 Proposal for a Joint Acoustical Classification Scheme

The main characteristics of the COST TU0901 proposal for an acoustic classification scheme for dwellings are, ISO/NP 1948814:

- It includes class criteria for airborne and impact sound insulation, noise from traffic and other external sources, and noise from service equipment, plus the optional evaluation of the reverberation time;
- It defines six classes (from A to F) with 4 dB steps between classes. For each class, there is a choice between sound insulation criteria down to 50 Hz or the common lower limit of 100 Hz;
- It may be used for describing the acoustic conditions in new as well as in existing housing, before and after renovation;
- It may be used for information to occupants of dwellings, including prospective tenants or buyers;
- It may be considered by the legislators as a basis for a national set of requirements;
- It may be used as reference for sustainability marking or labelling;
- Although descriptors are based on existing ISO standards, ISO 140-4, -5, -7 (now being transferred to ISO 16283, parts 1 to 3) and ISO 717 (2013), a simpler denotation has been used to avoid criteria indicated as a sum.

Comparison of the current sound insulation requirements in most of the European countries show that the requirements fit into class D in Table 2 on average, although with large deviations for service equipment and facades. This shows that the classification scheme includes ratings for dwellings with higher acoustic protection than corresponding to the current minimum ones.

## 3. SOUND INSULATION REGULATIONS IN THE UNITED STATES

### 3.1. National and Local Sound Insulation Codes

The situation in the United States (U.S.) is particularly different from that in Europe. US building codes have historically been developed by organizations of building officials, and have then been adopted as law by jurisdictions. At the end of the last century, the three main building code organizations that represented most U.S. jurisdictions (Building Officials and Code Administrators International – BOCA, International Conference of Building Officials – ICBO, and Southern Building Code Congress International - SBCCI) merged to form the International Code Council (ICC). This is a private organization with membership building code officials. The ICC serves updating the International Building Code (IBC) that may be adopted by states, counties, and localities.

Cities and towns publish noise ordinances that appear as part of their regulations or zoning planning by laws. These are usually emission type regulations as they typically control the sound that a source may produce at a receptor location. On the other side, the building code is intended to set a standard to ensure construction quality, by establishing a minimum sound insulation performance of constructions.

The IBC Section 1207, the one dedicated to noise control, includes the airborne and impact sound isolation performance of constructions that separate dwelling units. The airborne sound isolation performance limit is expressed as a minimum party wall and floor/ceiling sound transmission class (STC) rating of 50, if such a rating has been determined based on sound transmission loss measured in a laboratory, or 45 if determined from noise reduction measured in the field.<sup>16</sup> Similarly, the impact sound isolation performance limit is expressed as a minimum floor/ceiling impact isolation class (IIC) rating of 50, if such a rating has been determined on the basis of impact sound pressure levels produced by an ISO tapping machine and measured in a laboratory, or 45 if it has been determined from tapping machine sound pressure levels measured in the field (IBC, 2012).

Tocci described how the IBC has been modified in some local codes, such as the California Code of Regulation and the Building Code of the City of New York.<sup>17</sup> Generally, these local codes include some more prescriptions than the IBC. For examples, the City of New York requires an STC that is higher than 50 if based on laboratory reports or higher than 48 if field-tested, and an IIC higher than 51 if based on laboratory reports but higher than 49 if field-tested. Emission-type aspects such as the maximum sound power levels for mechanical equipment and the day-night average sound pressure emission level are also prescribed in the New York City and California code, respectively.

**Table 1.** European schemes for the sound classification of dwellings, relation to building codes, and indication of classes intended for new and "old" dwellings. Status June 2013. A new proposal prepared by COST TU0901 and approved as WI within ISO has been included for comparison. Table from Rasmussen and Machimbarrena.<sup>15</sup>

Country	Class denotations <sup>(1)</sup>	CS Reference (latest version)	Link BC to CS	BC Reference to CS	Comment	Classes for new dwellings	Classes for "old" dwellings
DK	A / B / C / D	DS 490 (2007)	+	Class C		A, B, C	D
FI	A / B / C / D	SFS 5907 (2004)	-	N/A	BC = Class C	A, B, C	D
IS	A / B / C / D	IST 45 (2011)	+	Class C		A, B, C	D
NO	A / B / C / D	NS 8175 (2012)	+	Class C		A, B, C	D
SE	A / B / C / D	SS 25267 (2004)	+	Class C		A, B, C	D
LT	A / B / C / D / E	STR 2.01.07 (2003)	+	Class C		A, B, C	D, E
IT	I / II / III / IV	UNI 11367 (2010)	-	N/A	BC ~ Class III	I / II / III / IV	
DE <sup>(2)</sup>	III / II / I	VDI 4100 (2012) <sup>(3)</sup>	-	N/A		III, II, I	None
AT	A / B / C / D / E	ÖNORM B 8115-5 (2012)	-	N/A	BC = Class C	A, B, C	D, E
NL	I / II / III / IV / V	NEN 1070 (1999) <sup>(4)</sup>	-	N/A	BC ~ Class III	I / II / III	IV, V
<b>COST TU0901</b>	<b>A - F and npd</b>	<b>ISO docs<sup>14</sup></b>	<b>N/A</b>	<b>N/A</b>	<b>(5)</b>	<b>A / B / C/D/E/F/ and npd</b>	

Abbreviations: BC = Building Code (regulatory requirements); CS = Classification scheme  
 (1) Classes are indicated in descending order, i.e. the best class first.  
 (2) Moreover, the German Society of Acoustics (DEGA) has published a recommendation (DEGA-Empfehlung 103, "Schallschutz im Wohnungsbau – Schallschutzausweis", DEGA, March 2009) for acoustic labelling of dwellings. The system has seven classes A\*-F and a colour code.  
 (3) The revised version of VDI 4100 published in 2012 changed descriptors from Rw and Ln,w to DnT,w and LnT, as had been discussed for years for the regulations. Also the class criteria were made stricter, and all classes are now stricter than regulations (before the lowest class corresponded to regulations).  
 (4) The classification scheme (including verbal explanations of classes) is described in (Gerretsen, 2009).<sup>16</sup>  
 (5) Proposal prepared by COST TU0901 (2013).<sup>14,17</sup> Submitted as Work Item for international standardization, (ISO, 2014).<sup>15</sup>

**Table 2.** Class criteria for airborne and impact sound insulation as proposed after the COST TU0901. Table from Rasmussen and Machimbarrena.<sup>15</sup>

Type of space	Class A DnT,50 (dB)	Class B DnT,50 (dB)	Class C DnT,50 (dB)	Class D DnT,50 (dB)	Class E DnT,50 (dB)	Class F DnT,50 (dB)
Between a dwelling and premises with noisy activities	≥ 68	≥ 64	≥ 60	≥ 56	≥ 52	≥ 48
Between a dwelling and other dwellings and rooms outside the dwelling	≥ 62	≥ 58	≥ 54	≥ 50	≥ 46	≥ 42
Type of space	Class A LnT,50 (dB)	Class B LnT,50 (dB)	Class C LnT,50 (dB)	Class D LnT,50 (dB)	Class E LnT,50 (dB)	Class F LnT,50 (dB)
In dwellings from premises with noisy activities	≤ 38	≤ 42	≤ 46	≤ 50	≤ 54	≤ 58
In dwellings from other dwellings	≤ 44	≤ 48	≤ 52	≤ 56	≤ 60	≤ 64
In dwellings: from common stairwells and access areas balconies, terraces, bath, toilet not belonging to own dwelling	≤ 48	≤ 52	≤ 56	≤ 60	≤ 64	≤ 70

### 3.2. How Far Are the United States from a Classification Scheme?

Section 3.1 has shown that the normative situation in the U.S. is far from a classification scheme. The main obstacles for this are that:

- the evaluation in the U.S. is mainly based on making a comparison with listed assemblies according to laboratory test reports often obtained through product manufacturers that have tested their products. Only in some local codes (such as the California Code) a report by an acoustical consultant or a field measurement approach may be required. Moreover, the general approach in case of real measurement is that if the STC or IIC ratings are measured, then the IBC permits lower ratings;
- the voluntary approach of the IBC provokes significant differences between jurisdictions, with some having adopted it, whereas others have passed specific legislations to modify or remove the noise control section;
- the IBC only applies to multifamily dwellings and a lack

of prescriptions about other building types exists, including all the non-multifamily residential buildings;

- the criteria are assessed through two single indicators, the STC evaluated above 125 Hz only, and the IIC evaluated above 100 Hz without being able to report low frequencies properties and does not take into account the requirements of the facades.

It can be expected that, at this time, an acoustic classification scheme in the U.S. may only be introduced within the context of sustainability assessment systems for buildings. Over the past several years, the U.S. Green Building Council has endeavoured to migrate the LEED rating system toward a global standard, taking into account various environmental design issues holistically. In fact, in the last few years, the high-performance design community has begun to recognize the importance of acoustical comfort as an important sensory aspect in assessing the indoor environmental quality (IEQ). As part of this recognition, the recent versions of LEED have included some acoustical requirements.<sup>18</sup> As an example, the USGBC first recognized the importance of acoustical comfort within environments for learning and healing, and so LEED for

Schools 2009 and LEED for Healthcare 2009 rating systems featured the following IEQ credits for acoustical performance:

- Schools-2009 EQp3: Minimal Acoustical Performance. Background noise from HVAC must be limited to 45 dB(A), and core learning spaces need a reverberation time below 1.5 seconds;
- Schools-2009 EQc9: Enhanced Acoustical Performance. Project teams are required to limit the background noise to a more challenging 40 dB and to meet ANSI Standard S12.60-2002, except windows, which must have an STC rating of at least 35;
- Healthcare-2009 EQc2: Acoustic Environment. The credit focuses on designing the facility to meet or exceed the sound and vibration criteria outlined in the 2010 Facility Guidelines Institute's Guidelines for Design and Construction of Health Care Facilities and the 2010 Sound & Vibration: Design Guidelines for Health Care Facilities.

In LEED v4, the previous credits have been made more stringent. For example, the prerequisite for schools now specifies a maximum HVAC background noise level of 40 dB(A). A new requirement asks high-noise sites to implement measures to mitigate sound transmission into core learning spaces. With LEED v4, USGBC has also broadened the notion of acoustic performance as an important IEQ issue by introducing a (pilot) credit for exterior noise control and expanding the niche acoustic performance credits into other building types. With the intent of establishing a comprehensive acoustic performance evaluation, USGBC has also proposed a credit in LEED BD+C Homes v4, which deals with "acoustically sensitive" spaces, such as bedrooms and dining rooms. The requirement may be satisfied using a prescriptive compliance path or a performance compliance path; in the first category, requests enforce common IBC prescriptions, by asking that "Attached single family homes and multi-family homes must have party walls with a minimum STC rating of 55. All party wall penetrations must be sealed with acoustical sealant and floor/ceiling assemblies must have a minimum STC and IIC rating of 55". Moreover, this USGBC credit focuses on four aspects:

- HVAC background noise. Mechanical equipment needs to be located strategically to reduce its impact, according to the 2011 ASHRAE Handbook, (Ch.48, Table 1) or AHRI Standard 885-2008 (Table 15). The credit also references to the ASHRAE 2011 Applications Handbook (Table 6) for maximum HVAC noise levels;
- Sound transmission/isolation. Appropriate construction assemblies and design strategies need to mitigate sound movement between spaces;
- Reverberation time. This is based on room type and application and can be affected by space geometry and by the presence and location of sound-absorptive finishes;
- Sound reinforcement and masking systems. These systems help to improve the sound clarity and privacy in an interior.

Another acoustic related credit in the new USGBC systems is in LEED Operations and Maintenance, the "Occupant Comfort Survey". This requires an acoustic evaluation, underlining

the importance of subjective perception for the comfort and wellness in a space.

Although the trend in considering more acoustic aspects in sustainability rating systems, the current LEED system seems far from having a structure to characterize different sound insulation classes.

## 4. DISCUSSION

One of the more controversial aspects in acoustic classification schemes regards the economic implications that may follow the decision to adopt a higher sound insulation class. For example, a few years ago, an acoustic classification scheme was developed as an Italian technical standard UNI 11367 (Table 1).<sup>22</sup> This scheme was never linked to a national law given the controversial effects that it could have had over the construction market.<sup>19</sup> In fact, the general perception of acoustic classification schemes was that the new legislation standard could be very demanding in terms of performance requests and hence expensive in terms of construction over-costs. Studies have shown that this risk is generally overestimated.<sup>20,21</sup> Also, the classification schemes were not intended to become mandatory, but they aimed to define schemes in order to recognize best practices.

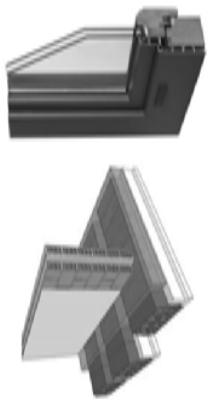
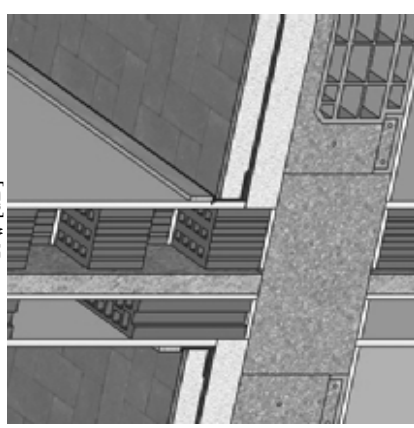
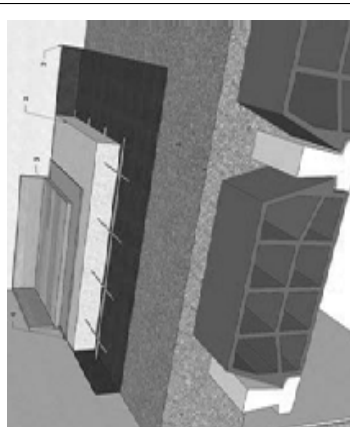
An analysis of the construction costs of technological solutions useful in the same building to achieve sound higher insulation classes revealed an increase of around 1% for a basic improvement in the sound insulation class, and around 4% for achieving the highest quality class pointed in the Italian standard UNI 11367.<sup>19</sup> Results of this analysis are reported in Table 3. The building was a concrete based building, with heavy cavity walls with insulation, and double glass windows; these technologies influence the specific cost necessary for achieving better sound insulation levels, and so the results cannot be assumed to be valid for other building systems. Attention should also be paid to the fact that this analysis did not take into account the costs of proper designing focused on obtaining higher sound insulation, and it only assumed that higher sound insulation standards were obtained through more performing building technologies. However, it is known that during the design most of the insulation problems may be solved, often without cost. Proper acoustic design requires not only adequate construction solutions, but also a rationalization of the internal distribution with a reduction in conflicts between functions and a careful analysis and execution during the construction phases.<sup>19</sup>

Another important aspect that the current discussion about acoustic classifications of dwellings has raised is the opportunity to introduce metrics that help the common public understand the meaning of sound insulation indicators and metrics. This aspect seems to be fundamental in order to rise the attention to more stringent sound insulation requests. An interesting preliminary scheme has been proposed by the COST Action TU0901, and it is reported in Table 4.

## 5. CONCLUSIONS

This paper has presented an overview of existing schemes for the sound classification of dwellings. Systems in place in European countries have briefly been presented to show their

**Table 3.** Acoustic classification according to the Italian standard UNI 11367 obtained for different building technologies. Table from Berardi.<sup>19</sup>

Sound Insulation Class	Facade sound insulation $D_{nT,w}$ [dB]	Airborne sound insulation $R_w$ [dB]	Impact sound insulation $L'_{n,w}$ [dB]	Incremental cost over the IV sound insulation class
<b>IV</b>	 <p>Double cavity brick wall with 12cm brick facing, rockwool insulation and 10 mm internal plaster. 30% façade is glazed surface.</p> <p><math>\geq 32</math></p>	 <p>Heavy cavity brick wall with rockwool insulation and 10 mm plaster on both sides</p> <p><math>\geq 45</math></p>	 <p>Floating floor over a concrete beam and ceramic block floor, with 10 mm plastered. Detail of the floating floor:</p> <p><math>\leq 68</math></p>	-
	<p><b>34</b></p> <p>Internal wall in hollow bricks 20 cm with 5 cm rockwool with a density of 50 kg / m<sup>3</sup></p> <p>Double glass 4/6/4</p>			
<b>III</b>	<p><b>37</b></p> <p>Internal wall in hollow bricks 20 cm with 5 cm rockwool with a density of 70 kg / m<sup>3</sup></p> <p>Double composite glass 8.4/6/5</p>	<p><b>46</b></p> <p>Double wall in hollow bricks (12 + 12 cm) with 5 cm rockwool with a density of 50 kg / m<sup>3</sup></p>	<p><b>64</b></p> <p>with PE polyolefin resin 5 mm</p>	<1%
	<p><b>41</b></p> <p>Internal wall in hollow bricks 20 cm with 7 cm rockwool with a density of 70 kg / m<sup>3</sup></p> <p>Double composite glass 8/16/6.4</p>	<p><b>51</b></p> <p>Double wall in hollow bricks (12 + 8 cm) with 5 cm rockwool with a density of 70 kg / m<sup>3</sup></p>	<p><b>62</b></p> <p>with double PE polyolefin resin 10 mm</p>	
<b>II</b>	<p><b>43</b></p> <p>Internal wall in hollow bricks 20 cm with 10 cm rockwool with a density of 70 kg / m<sup>3</sup></p> <p>Double composite glass 10/12/8.4</p>	<p><b>54</b></p> <p>Double wall in hollow bricks (12 + 12 cm) with 7 cm rockwool with a density of 70 kg / m<sup>3</sup></p>	<p><b>57</b></p> <p>with polyethylene foam and a sheet of lead foil 6 mm</p>	<2%
	<p><b>43</b></p> <p>Internal wall in hollow bricks 20 cm with 10 cm rockwool with a density of 70 kg / m<sup>3</sup></p> <p>Double composite glass 10/12/8.4</p>	<p><b>56</b></p> <p>Double wall in hollow bricks (12 + 8 cm) with 10 cm rockwool with a density of 70 kg / m<sup>3</sup></p>	<p><b>53</b></p> <p>with double polyethylene foam and a sheet of lead foil 12 mm</p>	
<b>I</b>	<p><b>43</b></p> <p>Internal wall in hollow bricks 20 cm with 10 cm rockwool with a density of 70 kg / m<sup>3</sup></p> <p>Double composite glass 10/12/8.4</p>	<p><b>56</b></p> <p>Double wall in hollow bricks (12 + 8 cm) with 10 cm rockwool with a density of 70 kg / m<sup>3</sup></p>	<p><b>53</b></p> <p>with double polyethylene foam and a sheet of lead foil 12 mm</p>	~4%

**Table 4.** Examples of the global indication of what can be expected for some airborne and impact sound sources.<sup>15</sup>

Noise source	Class A	Class B	Class C	Class D	Class E	Class F
loud speech	hardly audible	just audible, but not intelligible	audible, but hardly intelligible	just intelligible	intelligible	clearly intelligible
loud music	not audible	just audible	audible	clearly audible	very clearly audible	loud music
dropping & moving objects	not audible	hardly audible	just audible	audible	clearly audible	very clearly audible

structure. Then, the paper has focused on the proposed "acoustic classification scheme for dwellings" recently developed by the European COST Action TU0901. This proposal will be discussed within an ISO working group. The paper has also summarized the current state of sound insulation requirements in the U.S. The comparison reveals that the U.S. are far from considering an acoustic classification scheme. However, the current development of sustainability rating systems and, in particular, the attention that LEED has recently recognized to some acoustic parameter represents an important step in the U.S. market to go beyond the building code requirements. The hope is that sound classification schemes may facilitate exchanging experiences internationally, reducing trade barriers, and increasing the sound insulation of dwellings.

## REFERENCES

- <sup>1</sup> Leaman, A., Bordass, B. Productivity in buildings: the 'killer' variables, *Building Research & Information*, **27**(1), 4–19, (1999).
- <sup>2</sup> Dockrell, J.E., Shield, B.M. Acoustical barriers in classrooms: the impact of noise on performance in the classroom, *British Educational Research Journal*, **32**(3), 509–525, (2006).
- <sup>3</sup> Scannell, L., Hodgson, M., Villarreal, J.G.M., Gifford, R. The Role of Acoustics in the Perceived Suitability of, and Well-Being in, Informal Learning Spaces, *Environment and Behavior*, doi:0013916514567127, in press, (2015).
- <sup>4</sup> World Health Organization. Guidelines for Community Noise. Edited by Berglund, B., Lindvall, T., Schwela D.H., (1999).
- <sup>5</sup> Van den Berg, M. Neighbour Noise: A rational Approach, *Proceedings of the 2nd WHO International Housing and Health Symposium*. WHO, Bonn, 151–154, (2004).
- <sup>6</sup> Passchier, V.W., Passchier, W.F. Noise exposure and public health, *Environ Health Perspect.*, **108**(1), 123–131, (2000).
- <sup>7</sup> Rasmussen, B. Sound insulation between dwellings – Overview of the variety of descriptors and requirements in Europe, *Forum Acusticum 2011*, Aalborg, Denmark, (2011).
- <sup>8</sup> Rasmussen, B. Sound Classification of Dwellings – Quality Class Ranges and Class Intervals in National Schemes in Europe, *EuroNoise 2012*, Prague, Czech Republic, (2012).
- <sup>9</sup> Rasmussen, B. Sound classification of dwellings in the Nordic countries – Differences and similarities between the five national schemes, *BNAM 2012*, Odense, Denmark, (2012b).
- <sup>10</sup> Rasmussen, B. Sound insulation between dwellings – Requirements in building regulations in Europe, *Applied Acoustics*, **71**(4), 373–385, (2010).
- <sup>11</sup> Rasmussen, B., Rindel, J.H. Sound insulation between dwellings – Descriptors in building regulations in Europe, *Applied Acoustics*, **71**(3), 171–180, (2010b).
- <sup>12</sup> Gerretsen, E. Model-based assessment scheme for acoustic quality classes in buildings, *Proc. NAG/DAGA 2009*, Rotterdam, Netherlands, (2009).
- <sup>13</sup> COST Action TU0901. Integrating and Harmonizing Sound Insulation Aspects in Sustainable Urban Housing Constructions, (2009).
- <sup>14</sup> ISO/TC43/SC2 N1203 NWIP, Acoustics - Acoustic classification scheme for dwellings (Oct. 2013); ISO/TC43/SC2 N1218 Annex to N1203 COST TU0901 Proposal Acoustic classification (Nov. 2013); ISO/TC 43/SC2 N1244 Voting results ISO-NP 19488 Acoustic classification scheme for dwellings (2014).
- <sup>15</sup> Rasmussen, B., Machimbarrena, M. (eds.) Building acoustics throughout Europe, Vol. 1: Towards a common framework in building acoustics throughout Europe. COST TU0901. (2014).
- <sup>16</sup> IBC, International Building Code. International Code Council 2012, International Building Code, Chapter 1207 Sound Transmission, International Code Council, Washington, DC, (2012).
- <sup>17</sup> Tocci, G.C. Noise control in U.S. building codes, chapter 13, Edited by M.J. Crocker, John Wiley & Sons, (2007).
- <sup>18</sup> Berardi, U. Sustainability assessment in the construction sector: rating systems and rated buildings, *Sustainable Development*, **20**(6), 411–424, (2012).
- <sup>19</sup> Berardi, U. Economic evaluation of technological solutions for different sound insulation classes, *neo-EUBIOS*, **37**, 16–21, (2011).
- <sup>20</sup> Garg, N., Kumar, A., Maji, S. Significance and implications of airborne sound insulation criteria in building elements for traffic noise abatement, *Applied Acoustics*, **74**, 1429–1435, (2013).
- <sup>21</sup> Berardi, U., Rasmussen, B. Sound classification schemes of dwellings in Europe and U.S., POMA, *Proc. ASA Conference*, Providence, (2014).
- <sup>22</sup> UNI 11367:2010 Acustica in edilizia Classificazione acustica delle unit immobiliari Procedura di valutazione e verifica in opera (Building Acoustics - Acoustic classification of building units - Evaluation procedure and in-situ measurements).



---

---

# A Vibration Energy Approach Used to Identify Temperature Trending in Railroad Tapered-Roller Bearings

**Constantine M. Tarawneh**

*Department of Mechanical Engineering, College of Engineering and Computer Science, The University of Texas-Pan American, Edinburg, TX 78539-2999, USA*

**Rafael K. Maldonado, Arturo A. Fuentes and Javier A. Kypuros**

*The University of Texas-Pan American, Edinburg, TX, USA*

(Received 16 July 2014; accepted 5 March 2014)

Bearing temperature trending is a phenomenon that has plagued the railroad industry for decades and has resulted in costly train stoppages and non-verified bearing removals. Initial experimental studies conducted at The University of Texas-Pan American to explore this troubling phenomenon identified potential sources for the abrupt changes in temperature exhibited by some railroad bearings. The authors hypothesize that vibration-induced roller-misalignment is the root cause for bearing temperature trending. Hence, subsequent research focused on providing validation for the proposed hypothesis through vibration monitoring techniques. To that end, dynamic testers were used to run railroad bearings at the various speeds and loads that they experience in the field. A “trigger” bearing with a known cup raceway defect was used as a vibration source to induce roller misalignment on neighbouring defect-free bearings. Results show that the vibration energy of a bearing would decrease prior to an increase in temperature. In theory, misaligned rollers would vibrate less, leading to a decrease in the overall vibration energy, while also generating sufficient friction to account for the observed temperature increase. Typically, rollers realign themselves through geometrical thermal expansions or changes in the operating conditions, thus, returning to normal temperature and vibration levels. This paper outlines the research findings.

---

## NOMENCLATURE

$B_d$	mean diameter of a roller
$D_{\text{cone}}$	cone tapered large end diameter
$D_1$	roller large end diameter
$D_{\text{roller}}$	roller mean diameter
$D_s$	roller small end diameter
$L$	cone raceway tapered length
$N_b$	number of rollers
$P_d$	pitch diameter (span between the centres of two opposite rolling elements)
$R_{\text{cone}}$	radius of the cone
$R_{\text{cup}}$	radius of the cup
$\alpha_{\text{roller}}$	roller apex angle
$\theta$	contact angle between the cone raceway and tapered roller
$\phi_{\text{cone}}$	cone raceway tapered angle
$\omega_{\text{cage}}$	fundamental frequency of the cage
$\omega_{\text{cone}}$	fundamental frequency of the cone
$\omega_{\text{in}}$	fundamental frequency of a roller passing over a defect on the cone raceway
$\omega_o$	rotational frequency of the axle
$\omega_{\text{out}}$	fundamental frequency of a roller passing over a defect on the cup raceway
$\omega_{\text{roller}}$	fundamental frequency of the roller
$\omega_{\text{rolldef}}$	fundamental frequency of a roller defect as it contacts the cup and cone raceway
BPMI	ball pass frequency inner race or cone
BPFO	ball pass frequency outer race or cup

BSF	ball spin or roller/cage frequency
FTF	fundamental train/cage frequency
HBD	hot-box detector
PS	power spectrum
PSD	power spectral density

## 1. INTRODUCTION

One of the main concerns troubling railroad bearing manufacturers is the unexplained abrupt increase in the operating temperature of a healthy (defect-free) tapered-roller bearing—a phenomenon referred to in field service as bearing temperature trending. Currently, trended bearings are removed from service since they exhibit similar behaviour to a burn-off bearing at the end of its life. This troubling phenomenon has resulted in many costly delays associated with train stoppages, as well as false bearing removals by wayside temperature monitoring devices such as the Hot Box Detector (HBD). According to data collected by Amsted Rail from 2001 to 2007, an average of nearly 40% of bearing removals are non-verified. A non-verified bearing is one that, upon disassembly and inspection, is found not to exhibit any of the commonly documented causes of bearing failure such as: spalling, water contamination, loose bearings, broken components, lubrication, damaged seals, etc.

HBDs measure the infrared radiation emissions present in a railroad bearing and have been in place since the 1950's. The HBD is set to trigger an alert when a bearing is running 94.4°C (170°F) above ambient conditions. However, a more recent approach adopted by some railroads utilizes the HBD data to compare each bearing's temperature to the average tempera-

ture of all bearings along the same side of the train. If a bearing is running significantly hotter than the average temperature by some predetermined threshold, it is removed from field service and labelled as “trended.”<sup>1</sup>

In addition to the HBDs, acoustic measuring devices known as the Trackside Acoustic Detection System (TADS<sup>®</sup>) have been used in the field to identify defective bearings. The success rate of capturing a defective bearing is heavily based on the severity of the defect. Bearings with large defects known as “growlers” have a much higher rate of being recognized as opposed to bearings with smaller defects.<sup>2</sup> Although nearly five thousand HBDs are currently in service, only fifteen TADS<sup>®</sup> have been implemented in North America,<sup>3</sup> which means a train can run thousands of miles before encountering an acoustic bearing detector. Furthermore, the majority of trended bearings are found to be defect-free, which means that TADS<sup>®</sup> will not detect them.

From the above discussion, it is evident that the existing wayside monitoring equipment utilized in field service does not constitute a true continuous bearing health monitoring system, but rather a sporadic check on the bearing condition. Thus, neither temperature nor acoustic measuring devices, currently in use, can accurately characterize the internal condition of a temperature-trended bearing. To this end, the railroad research group at the University of Texas-Pan American (UTPA) conducted a series of experimental and theoretical studies focused at understanding the bearing temperature trending phenomenon and its root causes, with the main objective of finding ways to distinguish healthy (defect-free) bearings undergoing temperature trending from defective bearings nearing catastrophic failure. The latter will aid the railroad industry in minimizing unnecessary train stoppages and false bearing removals.

## 2. BACKGROUND

Thermal investigations of roller bearings have been carried out for a few decades now.<sup>4–8</sup> These efforts range from purely theoretical works to studies containing a combination of theory and application to purely experimental projects. The theoretical studies examined two abnormal operating conditions: partially or fully jammed roller bearings and a stuck brake. A partially jammed roller bearing is one that rotates with velocities greater than zero but less than the epicyclic speed, while a fully jammed roller bearing is one that has no velocity with respect to the cage. The investigation into the jammed rollers and a stuck brake condition revealed that the maximum temperature within the bearing assembly can reach 268°C (514°F) and 126°C (259°F), respectively, compared to the normal operating condition temperature of 81°C (178°F).<sup>5,6</sup> In a similar study, a dynamic model of the torque and heat generation rate in tapered-roller bearings under excessive sliding conditions was developed using a lumped-parameter approach in the program SHABERTH.<sup>7</sup> This investigation focused on jammed roller bearings, and the model was run with an assumed ambient temperature of 25°C (77°F), a load per row of 80,000 N (18,000 lb), and a rotational speed of 560 rpm, which corresponds to a train speed of 97 km/h (60 mph). The study concluded that the heat generated in the bearing was proportional to the number of jammed rollers and that the heat generation at the roller-end contacts increased with the number of jammed rollers.

In yet another theoretical work, finite element analysis with ABAQUS and FORTRAN was used to model thermally induced failures in railroad class F (6½ × 12) tapered-roller bearings, which resulted from laboratory experiments conducted at high operating speeds.<sup>8</sup> The experiments were conducted by the Association of American Railroads (AAR), and showed that new (defect-free) bearings failed after 200 to 300 hours of operation at a speed of 161 km/h (100 mph) and none failed at 129 km/h (80 mph).<sup>8</sup> The study concluded that the thermal and mechanical instabilities in a railroad roller bearing are directly related to the heat generated at the roller-end contacts. The increase in the heat generation is a direct consequence of the grease starvation mechanism caused by the high operating speeds, which results in a larger friction coefficient.<sup>8</sup>

Understanding that manufacturing tolerances of bearing assembly components are hard to maintain on a large-scale production basis, in the 1970’s Jamison et al. conducted a detailed study of the geometric effects on the rib-roller contact in tapered-roller bearings,<sup>9</sup> as the latter directly influences bearing performance. As anticipated, their findings indicate that out-of-tolerance components can result in abnormal operating conditions leading to excessive friction and rapid wear at the rib-roller contact region, which can cause roller skew and grease starvation that may eventually lead to catastrophic bearing failure. Consequently, a number of other theoretical and experimental studies have been performed to explore the effects of geometrical imperfections and surface irregularities on the vibrational characteristics of tapered-roller bearings under varying axial loading and rotational speeds<sup>10–12</sup> and to detect bearing defects using frequency domain analysis.<sup>13</sup> Gupta investigated the dynamics of a tapered-roller bearing by modelling the general motion of the roller and cage based on the frictional behaviour and cage clearances of the bearing.<sup>14</sup> His study showed that roller skew (misalignment) increases with increasing friction. At relatively high friction and low cage-pocket and guide-land clearances, the roller was found to maintain steady contact with the cage pocket on one side while the contact is cyclic (pivoting) on the other end. Gupta’s findings were later confirmed by an experimental study that was conducted by Yang et al. using specialized capacitance probes to measure and examine the effects of speed and lubrication on the degree of the roller skew (misalignment).<sup>15</sup> It was discovered that the friction between the rib-roller end contact causes the roller’s large end (pointing toward the grease seal) to run ahead of the smaller end (pointing toward the spacer ring), thus, leading to roller misalignment. The degree of the roller skew may vary between rollers, and it increases with increasing speed and the lubrication of the larger end of the roller.

Despite the progress made in understanding the dynamics of tapered-roller bearings, no methods or techniques have been developed to identify temperature trending events that result from vibration-induced roller misalignment. Tarawneh et al. conducted a series of experimental and theoretical studies aimed at exploring temperature trending in railroad bearings, finding the root cause of this troubling phenomenon and devising ways to identify it using vibration analysis techniques.<sup>16–22</sup> The authors first set out to replicate the discoloration of tapered rollers (evidence of heating) observed in the trended bearings removed from service.<sup>16</sup> Theoretical modelling agreed with the laboratory testing results in proving that extreme roller temperatures can occur without noticeably raising the temperature of the bearing cup outer surface—the part of the bearing

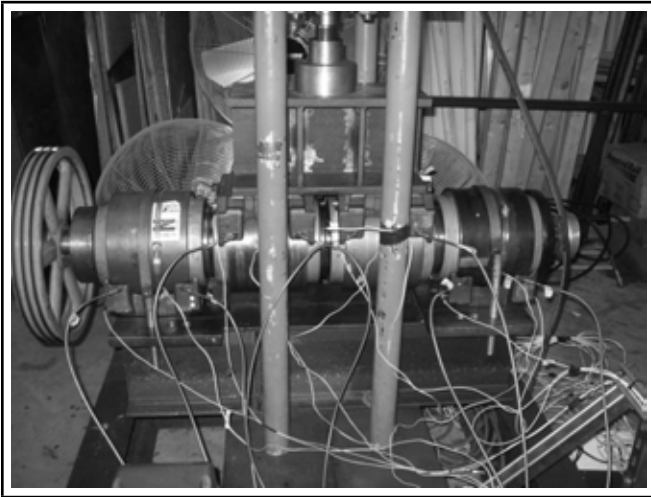


**Figure 1.** A picture of the four-bearing dynamic tester at UTPA showing the sensor placement.

scanned by the current wayside detectors.<sup>17-19</sup> For example, one of the case studies demonstrated that it is possible for three consecutive rollers within a cone assembly to operate at an abnormal temperature of 232°C (which would cause roller discoloration), yet the bearing cup temperature stays at 88.5°C.

With the new understanding of heat transfer paths of tapered-roller bearings based on experimental and theoretical studies,<sup>17-19</sup> Tarawneh et al. next conducted a series of tests on “trended” bearings pulled from field service along with their mates (the bearing on the opposite end of the axle).<sup>20</sup> The latter work was based on eight laboratory experiments performed on a four-bearing dynamic tester, depicted in Fig. 1, with an axle rotational speed of 536 rpm, which is equivalent to a train traveling at 91.7 km/h (57 mph). One experiment featured a trending event in which the bearing cup temperatures of two bearings experienced a 24°C (43.2°F) increase over a period of 50 minutes.<sup>20</sup> This behaviour occurred simultaneously in a field-trended bearing and its mate, which were separated by a control bearing. The synchronized temperature response ruled out heat transfer as the source for the abrupt change in temperature. The only other explanation for the observed phenomenon is vibration induced heating, where the effects of the oscillations of the rollers in the trended bearing travel along the axle and trigger similar behaviour in the mate bearing. Upon disassembly and inspection, a spall was found on one of the cup raceways of the trended bearing, providing evidence that roller vibration could be the root cause of the temperature trending. Subsequent laboratory tests were effective in achieving temperature trending by using a bearing with a known cup raceway defect to trigger vibration-induced roller misalignment, which is responsible for producing excessive frictional heating in short time periods. The aforementioned laboratory findings were validated in a carefully controlled and executed field test.<sup>21</sup> A bearing in field service, unlike the laboratory setting, is exposed to a variety of vibration excitation sources such as wheel impacts resulting from wheel flats, railcar hunting, and rail track defects. Hence, the performed field test utilized defective wheels as the vibration source to initiate temperature trending in the test bearings. The field test was successful in reproducing several bearing temperature trending events, thus, providing further evidence to verify the laboratory results.<sup>21,22</sup>

The authors used vibration-monitoring techniques to identify dynamics likely associated with roller misalignment and

correlate the onset of such dynamics with abrupt changes in bearing temperature. Depending on the relative spacing between the rollers, cage bars and cones, and on the magnitude of the vibration trigger, roller oscillations can be severe and are more likely to lead to rollers being caught misaligned as they enter the loaded region of the bearing. In such cases, the roller’s large end will tend to lead due to the friction between the cone rib and the roller end contact point. Consequently, excessive frictional heating will be generated as the severity and number of misaligned rollers increases. The latter will manifest in a sudden rise in bearing-cup temperature. Friction created by sliding misaligned rollers will reduce the epicyclic speed of the cage, which may also vary based on the severity and number of misaligned rollers. In the presence of misalignment, a roller will occupy more space within the cage pocket causing deformations of the cage and essentially creating a tighter fit throughout the cone assembly. Hence, it is expected that the occurrence of roller misalignment will effectively decrease the level of vibration within a bearing as rollers no longer roll or have space to oscillate within the cage pockets.

Roller realignment can occur for one of many reasons including thermal expansion in the cone assembly components, grease circulation, external vibration sources, etc. During the realignment process, a roller will pivot within the cage pocket as the cage and radial clearance reduces forcing rollers to realign. This behaviour is similar to the investigations conducted by Gupta in which one end of the roller maintains steady contact with one side of the cage pocket while the other end pivots.<sup>14</sup> In this scenario, the constant pivoting interaction between the roller and raceway surfaces may explain why defects tend to generally develop on raceways anywhere between the centre of the roller and the smaller end. The pivoting motion, while detrimental to a bearing’s life, may promote grease flow, decreasing the temperature to or below normal operating conditions. The cyclic behaviour of the roller will affect the rotational frequency of the cage, momentarily speeding up or slowing down depending on the location and impact of the roller within the cage pocket. Overall, the vibration levels are expected to increase due to the pivoting motion of the roller. Hence, it is essential to quantify the total vibration energy of a bearing in order to garner vital information regarding its operating condition.

It has been experimentally observed that a bearing operating at normal conditions maintains a steady level of vibration energy with minor fluctuations. However, a bearing’s vibration energy tends to decrease shortly prior to an increase in temperature and will increase prior to a drop in temperature. This observation proposes a relationship between vibration energy, roller misalignment, and temperature trending events.

The work presented in this paper differs from others in that it focuses on relating the temperature and vibration energy characteristics of a bearing experiencing a temperature trending event in an effort to devise an algorithm that can be used to differentiate between defective bearings nearing the end of their service life and defect-free bearings exhibiting a trending event. To this end, the following methodology was utilized to meet the objectives of this study:

1. The bearing components’ fundamental frequencies were determined from a two-dimensional kinematic model.<sup>21,22</sup>

2. A Fast Fourier Transform (FFT) of the acquired data was performed to identify potential shifts in the fundamental frequency of the cage and its harmonics.
3. The total vibration energy was determined by calculating the area under the Power Spectral Density (PSD) curve.
4. Abrupt bearing heating caused by roller misalignment is demonstrated through:
  - (a) a reduction in the vibration energy levels within the bearing as misaligned rollers tend to deform the cage, thus, creating a tighter fit between bearing components, and
  - (b) a decrease in the rotational frequency of the cage and its overtones due to the excessive friction generated by the sliding rollers at the cone rib and roller end contact.
5. Subsequent decrease in bearing-cup temperature is confirmed through:
  - (a) an increase in the vibration energy level as the cage and radial clearance reduction forces rollers to pivot within the cage pocket in an attempt to realign, and
  - (b) an increase in the rotational frequency of the cage and its harmonics coupled with some fluctuations due to the pivoting motion of the rollers within the cage pockets.
6. Demonstrate the effects of vibration on temperature by proving that changes in vibration energy precede sudden changes in temperature.

### 3. EXPERIMENTAL METHODOLOGY

The experiments were performed using two-dynamic bearing testers. A picture of one of these testers showing the experimental setup and sensor locations is provided in Fig. 1. Each dynamic tester can accommodate four class F ( $6\frac{1}{2} \times 12$ ), class K ( $6\frac{1}{2} \times 9$ ), class E ( $6 \times 11$ ), or class G ( $7 \times 12$ ) tapered-roller bearings mounted on a customized axle. The first tester employs an 18.64 kW (25 hp) fixed-speed motor with a pulley-drive system. Four distinct pulley sizes are used to rotate an axle at angular velocities of 498 rpm, 562 rpm, 618 rpm, and 796 rpm, which correspond to train speeds of 85.30 km/h (53 mph), 96.56 km/h (60 mph), 106.2 km/h (66 mph), and 138.40 km/h (86 mph), respectively. The second tester utilizes a 22 kW (30 hp) variable-speed drive motor managed by a smart controller that can produce equivalent train speeds ranging from  $\sim 5$ –138 km/h ( $\sim 8$ –86 mph). Forced convection cooling over the axle-bearing assembly is achieved with three fans that produce an average air stream of 5 m/s (11.2 mph). Each dynamic bearing tester is equipped with a hydraulic cylinder capable of applying vertical loads ranging from 0 to 150% of a full-operating load [100% load condition simulates a fully-loaded freight car and corresponds to a load of 159,000 N (35,750 lb per bearing) for class F and class K bearings, 122,326 N (27,500 lb per bearing) for class E bearings, and 178,000 N (40,000 lb per bearing) for class G bearings].

The dynamic bearing tester with the variable-speed drive motor is housed in a specially constructed temperature-controlled environmental chamber capable of maintaining a wide range of ambient temperatures from as low as  $-40^\circ\text{C}$

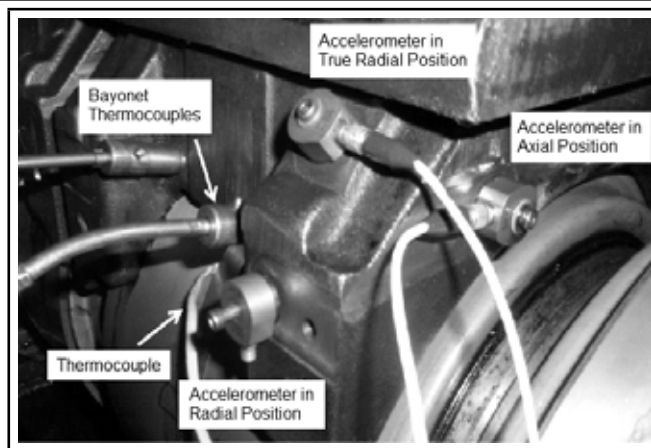


Figure 2. Thermocouple and accelerometer sensor placement.

( $-40^\circ\text{F}$ ) and up to  $55^\circ\text{C}$  ( $131^\circ\text{F}$ ). The environmental chamber is equipped with a commercial freezer unit with a cooling capacity of 7.6 kW. An added feature of the chamber tester is the ability of the smart controller to output the axle torque, speed, and motor power consumption with an accuracy of  $\pm 0.5\%$ .

The bearing adapters are specifically machined to accommodate two accelerometers and two K-type bayonet thermocouples—one on each raceway. The vibration sensors used are single-axis through-hole mount accelerometers with a sensitivity of 10 mV/g, a peak measuring range of  $\pm 500$  g, and a bandwidth of 10 kHz. Two accelerometers were placed either on the pulley or odometer side of an adapter. One accelerometer was located on the side face of the adapter (referred to as the axially-mounted accelerometer). The second accelerometer was placed either on the back face or on the edge slant of the adapter, corresponding to radial and true radial placement, respectively. To verify the accuracy of the bayonet thermocouples, a K-type thermocouple was secured to the centre of the bearing cup using a hose clamp and aligned with the bayonet thermocouples. Two additional K-type thermocouples were placed on the front and back of the test rig to record the ambient temperature. A total of fourteen thermocouples and eight accelerometers were monitored and recorded during testing. Thermocouple and sensor locations are shown in Fig. 2.

For this study, four test speeds ranging from low to high were chosen: 233 rpm, 498 rpm, 560 rpm, and 796 rpm, which are equivalent to train-traveling speeds of 40.23 km/h (25 mph), 85.30 km/h (53 mph), 96.56 km/h (60 mph), and 138.40 km/h (86 mph), respectively. Only class F and K bearings were used for all the experiments discussed in this paper.

The experimental setup was designed to replicate speeds and cargo loads observed in field service. Depending on the specific test conducted, a “trigger” bearing with a known cup raceway defect (i.e., a cup spall) was used to introduce vibration into the axle-bearing assembly in order to promote roller misalignment. The cup spalls utilized in the laboratory testing were either spalls that developed naturally in service and were pulled from the field or artificially-made spalls created in the laboratory by grinding off material from the cup raceway. A picture of one of the naturally-spalled cup raceways used in the laboratory testing can be seen in Fig. 3.

The four bearings mounted on the customized axle were labelled as Bearings 1 through 4 starting at the pulley side. Four tests were conducted for each experiment that utilized a trigger bearing. Referring to Fig. 4, in the first three tests, the location of the cup spall was varied between  $345^\circ$  (just before the load



Figure 3. Cup raceway spall that developed naturally in service and was pulled from the field.

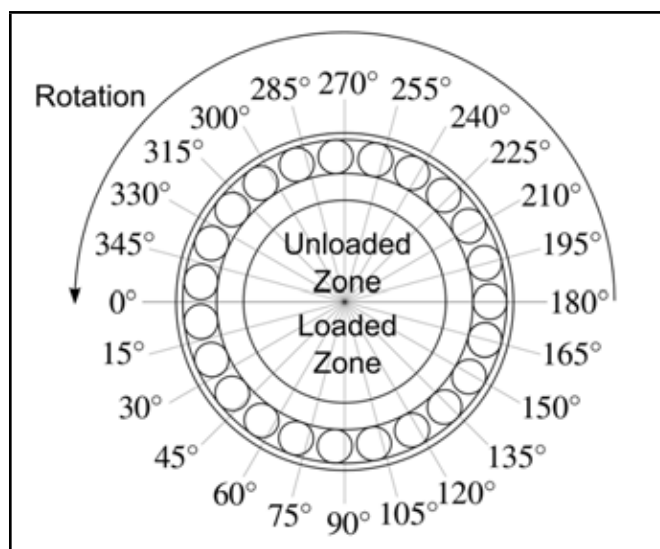


Figure 4. Spall placement diagram for bottom-loaded bearings (inverted for top-loaded bearings).

zone), 0° (at the beginning of the load zone), and 15° (just after the beginning of the load zone); all run at a 17% load simulating an empty railcar. The test generating the most temperature trending events was repeated utilizing a 100% load simulating a fully-loaded railcar, which constituted the fourth and last test of the experiment. A discussion of the data analysis techniques used to acquire the results of this study follows.

#### 4. DATA ANALYSIS

The temperature data was recorded once every 20 seconds, utilizing a sampling rate of 100 samples per second. Hence, each temperature data point is the average of 100 readings. Furthermore, the bearing temperature profiles were generated by averaging the readings of the two K-type Bayonet thermocouples that monitor the temperature of the two raceways within each bearing.

The vibration data was sampled at a rate of 9600 samples per second or 10240 samples per second depending on the data acquisition system used. Due to data storage limitations associated with the prolonged durations of these tests, the data acquisition systems were programmed to record 20 seconds of data and generate a file once every 10 minutes. The raw data file contained the time and acceleration (g) recorded by each accelerometer used during testing. The frequency response was generated by performing an ensemble average of

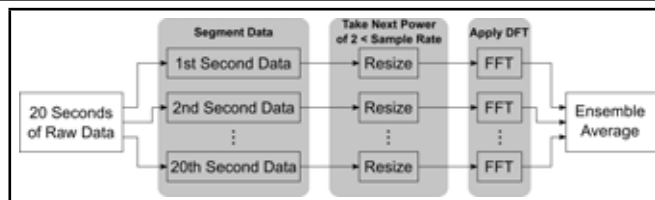


Figure 5. Ensemble averaging process.

twenty, one-second segments of data collected at a constant axle speed (i.e., twenty seconds of raw vibration data was partitioned into one-second intervals). Hence, each one-second segment contained either 9600 or 10240 samples. The discrete Fourier transform (DFT) was calculated for each segment using a MATLAB™ fast Fourier transform function (FFT). The MATLAB™ fast Fourier transform functions are based on a library called FFTW.<sup>23,24</sup> They can be used to compute N-point DFTs. Because the numerical method employed performs fastest when N is power of 2, for each one-second segment, 8192 samples are used to generate the DFT where 8192 is the next power of 2 less than either 9600 or 10240. The mean of the resulting twenty DFTs is then taken to generate the ensemble average. The process described here is illustrated in Fig. 5. For analysis purposes, the resulting amplitude spectrum is plotted up to the Nyquist frequency so that the frequency range is from 0 to half the power of 2 less than the sampling rate (i.e., 0 to 4096 Hz). Note that doubling the sampling rate did not change any of the results or conclusions presented in this study.

In order to identify the level of vibration in a bearing, the *direct approach* was used in order to evaluate the energy contained in an analogue signal,  $x(t)$ , as the magnitude of a signal squared integrated over time, as shown by Eq. (1),

$$E = \int_{-\infty}^{\infty} |x(t)|^2 dt. \tag{1}$$

Furthermore, from Parseval's Theorem, which states that

$$\int_{-\infty}^{\infty} |x(t)|^2 dt = \int_{-\infty}^{\infty} |X(f)|^2 df; \tag{2}$$

it can be shown that the energy density function,  $|X(f)|^2$ , referred to as the energy spectral density, the power spectral density (PSD), or simply the power spectrum (PS), integrated over the frequency range is equal to the energy contained in a signal. In the direct approach, the power spectrum is calculated as the magnitude squared of the Fourier transform, as shown in Eq. (3),

$$PS(f) = |X(f)|^2. \tag{3}$$

The use of Eqs. (1)–(3) allows for a simple manipulation to measure the energy of a signal by determining the power spectrum and integrating over a specified range of frequencies.

Frequency analysis facilitated identification of the bearing components' primary frequencies. There are a total of six fundamental frequencies observed in tapered-roller bearings. All frequencies are dependent on the rotational frequency of the axle ( $\omega_o$ ). Three of the bearing component angular frequencies are the cone ( $\omega_{cone}$ ), the cage ( $\omega_{cage}$ ), and the roller ( $\omega_{roller}$ ) frequencies. The remaining three frequencies correspond to defects or geometrical irregularities on the cup (outer) raceway

**Table 1.** Bearing manufacturer class F / K specified cone dimensions.

$D_{\text{cone}}$ [cm]	18.887
$L_{\text{cone}}$ [cm]	5.034
$\Phi_{\text{cone}}$ [rad]	0.141

**Table 2.** Bearing manufacturer class F / K specified roller dimensions.

$D_1$ [cm]	2.223
$D_s$ [cm]	2.057
$\Theta_{\text{roller}}$ [rad]	0.033

( $\omega_{\text{out}}$ ), the cone (inner) raceway ( $\omega_{\text{in}}$ ), and the roller ( $\omega_{\text{roller}}$ ). These frequencies tend to increase in magnitude when an associated defect or geometric inconsistency is present. Dimensions of the cone and roller as specified by the manufacturer, given in Table 1 and Table 2, respectively, were used to calculate the dimensions necessary to derive the fundamental frequencies. The mean diameter of a tapered roller,  $d_{\text{roller}}$ , is calculated along its centre. The radius of the cone,  $r_{\text{cone}}$ , is calculated from the centre of the cone to the centre of the raceway also known as the centre of the tapered length. The radius of the cup,  $r_{\text{cup}}$ , is calculated as the distance between the centre of the cone and the location where the mean diameter of the roller,  $d_{\text{roller}}$ , comes in contact with the cup raceway. A cross-sectional diagram of a railroad bearing illustrating the locations of the abovementioned measurements is provided in Fig. 6. Final dimensions used to calculate the bearing components primary frequencies are listed in Table 3.

The equations used to obtain  $d_{\text{roller}}$ ,  $r_{\text{cone}}$ , and  $r_{\text{cup}}$  utilizing information presented in Table 1 and Table 2 are provided hereafter as Eqs. (4–6):

$$d_{\text{roller}} = \frac{D_1 + D_s}{2}; \tag{4}$$

$$r_{\text{cone}} = \frac{d_{\text{cone}}}{2} - \frac{L_{\text{cone}}}{2} \sin(\phi); \tag{5}$$

$$r_{\text{cup}} = r_{\text{cone}} + d_{\text{roller}} \cos(\phi + \theta). \tag{6}$$

The equations used to determine the six fundamental frequencies of tapered-roller bearings, Eqs. (7–12), were derived by Tarawneh et al. from a 2-D kinematic model.<sup>21,22</sup> Detailed derivations of these equations can be found elsewhere.<sup>25</sup>

$$\omega_{\text{cone}} = \omega_0; \tag{7}$$

$$\omega_{\text{cage}} = \left( \frac{r_{\text{cone}}}{r_{\text{cone}} + r_{\text{cup}}} \right) \omega_{\text{cone}}; \tag{8}$$

$$\omega_{\text{roller}} = \left( \frac{r_{\text{cone}}}{d_{\text{roller}}} \right) \omega_{\text{cone}}; \tag{9}$$

$$\omega_{\text{out}} = 23 \omega_{\text{cage}}; \tag{10}$$

$$\omega_{\text{in}} = 23 (\omega_{\text{cone}} - \omega_{\text{cage}}); \tag{11}$$

$$\omega_{\text{rollerdef}} = \left( \frac{r_{\text{cup}}}{d_{\text{roller}}/2} \right) \omega_{\text{cage}}. \tag{12}$$

## 5. DISCUSSION OF RESULTS

As mentioned earlier in this paper, experimentally acquired data indicate that a bearing operating at normal conditions maintains a steady level of vibration energy with minor fluctuations. However, during temperature trending events brought on by roller-misalignment, the vibration energy tends to decrease shortly prior to an increase in temperature and will increase prior to a drop in temperature. These observations signify that there is a relationship between vibration energy, roller misalignment, and temperature trending events.

**Table 3.** Class F / K tapered-roller bearing calculated dimensions.

$d_{\text{roller}}$ [cm]	2.140
$r_{\text{cone}}$ [cm]	9.089
$r_{\text{cup}}$ [cm]	11.196

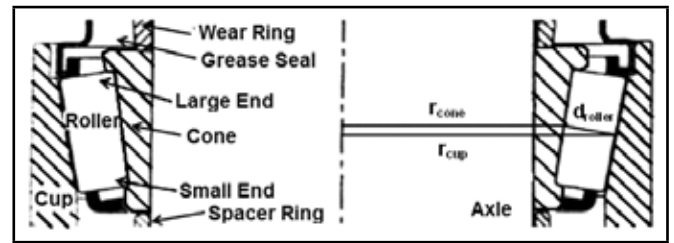


**Figure 6.** Cross-sectional diagram illustrating the locations of the measurements used to calculate the bearing components fundamental frequencies.

To provide evidence of the abovementioned behaviour, a series of laboratory tests were conducted utilizing several different combinations of operating speed and loading conditions, as described in Table 4. For each experiment, the temperature history and the vibration energy plots were generated. Select instances were then identified just prior to an increase or decrease in the vibration energy levels within a specific bearing on the bearing-axle assembly. The corresponding points on the temperature profile of that specific bearing were also determined, which generally preceded the onset of an abrupt change in temperature. The time delay between the initiation of a vibration energy trend and a temperature trend was tracked and quantified to demonstrate the effects of vibration on the bearing temperature.

The rotational frequencies of the dominant cage harmonic ( $\omega_{\text{out}}$ ) were tracked throughout the experimental testing in order to demonstrate the effects of roller-misalignment. Instances in the  $\omega_{\text{out}}$  signal corresponding to an abrupt change in the energy level were identified. A subsequent point in time at the lowest or highest level in energy was chosen to analyse and provide evidence of changes in the rotational speed of the cage. Based on previously performed research,<sup>25</sup> in order to account for slip, the experimentally acquired  $\omega_{\text{out}}$  rotational frequencies were determined by selecting the dominant frequency within  $\pm 1$  Hz for speeds less than 600 rpm and  $\pm 1.5$  Hz for speeds greater than 600 rpm of the theoretically calculated frequency given by Eq. (10). Note that the figures in this paper display the dominant  $\omega_{\text{out}}$  frequency within the range and ignore the side-band peaks that may result from roller misalignment. Table 5 provides the six theoretically calculated fundamental bearing component frequencies, Eqs. (7–12), based on the utilized test speeds.

**Table 4.** Experimental setup description.

Experiment	Load	Speed [km/h] (mph)	Spall [°]	Bearing 1	Bearing 2	Bearing 3	Bearing 4
1	17%	96.56 (60)	345	Normal Poly	Normal Poly	Normal Poly	Steel Trigger
2	17%	96.56 (60)	10	Normal Poly	Normal Poly	Normal Poly	Steel Trigger
3	100%	85.30 (53)	350	Normal Poly	Normal Steel	Normal Poly	Steel Trigger
4	125%	138.40 (86)	N/A	Normal Poly	Normal Poly	Normal Poly	Normal Poly
5	17%	40.23 (25)	N/A	Normal Poly	Normal Poly	Normal Poly	Normal Poly

**Table 5.** Class F / K natural frequencies of tapered-roller bearing components and defects.

Natural Frequency [Hz]	40.23 km/h (25 mph) (233 rpm)	85.30 km/h (53 mph) (498 rpm)	96.56 km/h (60 mph) (560 rpm)	138.40 km/h (86 mph) (796 rpm)
$\omega_{\text{cone}}$	3.88	8.30	9.22	13.27
$\omega_{\text{cage}}$	1.74	3.72	4.13	5.94
$\omega_{\text{roller}}$	16.49	35.25	39.15	56.35
$\omega_{\text{out}}$	40.02	85.53	94.98	136.72
$\omega_{\text{in}}$	49.30	105.37	117.00	168.42
$\omega_{\text{rolldef}}$	18.21	38.92	43.21	62.20

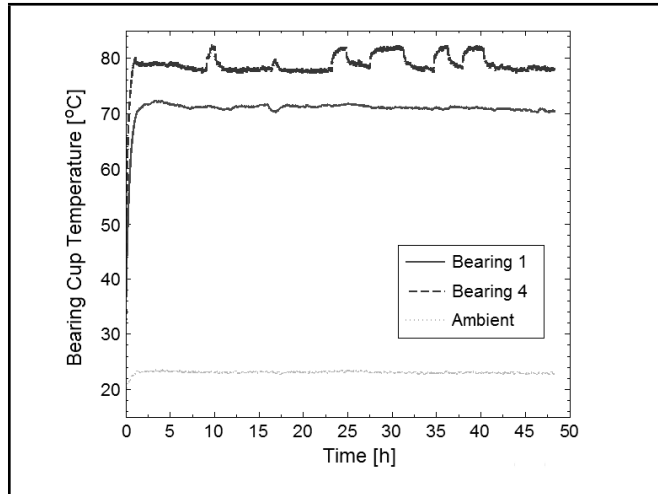


**Figure 7.** Experiment 1 bearing temperature profiles; class K bearings; spall placement: 345° (refer to Fig. 4); speed: 96.56 km/h (60 mph); load: 17% (empty railcar).

## 5.1. Experimental Results

### 5.1.1. Experiment 1

Experiment 1 was carried out at a speed of 95.56 km/h (60 mph, 560 rpm) and a load of 17%, simulating an unloaded railcar. A cup spall on Bearing 4 positioned 15 degrees before the load zone (345° referring to Fig. 4) provided the vibration source for the axle-bearing assembly. The temperature profiles and bearing vibration energies can be seen in Fig. 7 and Fig. 8, respectively. Bearing 4, a bottom-loaded bearing with a spalled cup, displayed multiple fluctuations in temperature. At five different instances, the temperature increased and held steady at approximately the same level before returning to normal operating conditions. The temperature profile for Bearing 4 along with the corresponding vibration energy recorded by the accelerometer is provided in Fig. 9. It can be seen that each increase in temperature is preceded by a decrease in the vibration energy level. The aforementioned phenomenon seems to suggest that roller misalignment, which is what causes the decrease in the vibration energy of the bearing, is also what generates the frictional heating that eventually results in the observed rise in temperature. Note that the vibration energy decreased to similar levels at each of the corresponding five temperature increases.

To further illustrate the abovementioned observations, four select data points were examined—two uptrends and two downtrends. Referring to Fig. 9, energy began to decrease significantly at approximately 8.83 and 34.5 hours into the test. Consequently, the temperature began to increase at approximately 9.08 and 34.68 hours into testing. In each case, vibration energy changes preceded temperature changes by 10.8 to 15 minutes. Conversely, increases in vibration energy oc-

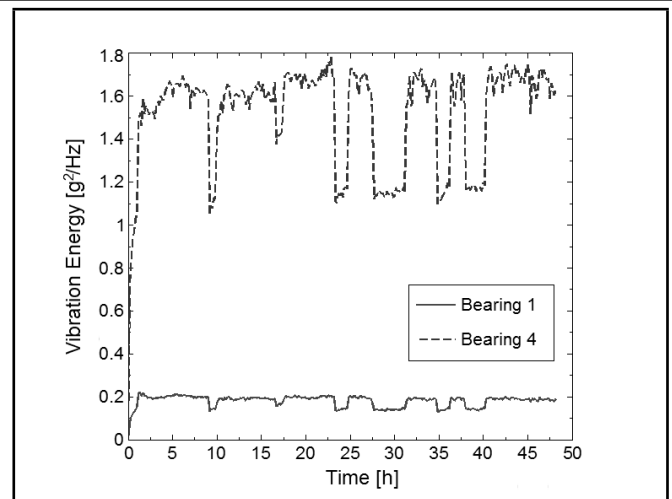


**Figure 8.** Experiment 1 vibration energy captured by radial accelerometers.

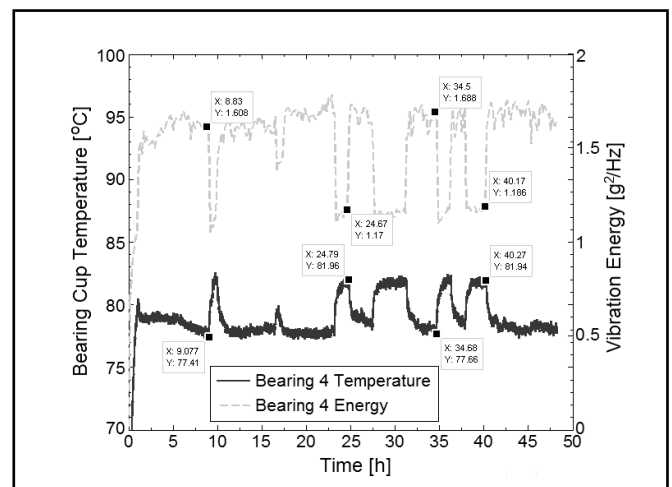


**Figure 9.** Experiment 1 temperature profile vs. vibration energy for Bearing 4.

curing at approximately 24.67 and 40.17 hours into the test preceded decreases in temperature observed at 24.79 and 40.27 hours into the test, respectively. Again, changes in temperature lagged those in vibration energy by 6 to 7.2 minutes. The latter behaviour cannot be explained by changes in lubrication nor thermal expansions of bearing components. The short period between vibration activity and temperature reaction provides supporting evidence that this phenomenon is the result of bearing heating brought on by vibration-induced roller misalignment. Note that, even though the remaining three bearings on the axle displayed changes in their vibration energy similar to Bearing 4, the magnitude of these changes was much smaller, as seen in Fig. 8, and did not result in an increase in the bearing temperature. The latter behaviour can be explained by *cross-talk* between the four bearings that share an axle. Given the fact that Bearing 4 has a significant spall on its outer (cup) raceway, the generated vibration will be picked up by the remaining three bearings, and so do any noticeable changes in that vibration energy. However, since the rollers are not actually misaligned on those other three bearings, no change in temperature accompanies the observed changes in vibration.

In accordance with the hypothesis proposed in this paper, the pivoting motion of a roller can either speed up or decrease the rotational speed of the cage. In order to identify potential shifts in frequency, the total vibration energy of Bearing 4 was plotted alongside the fundamental  $\omega_{\text{out}}$  frequency, as shown in

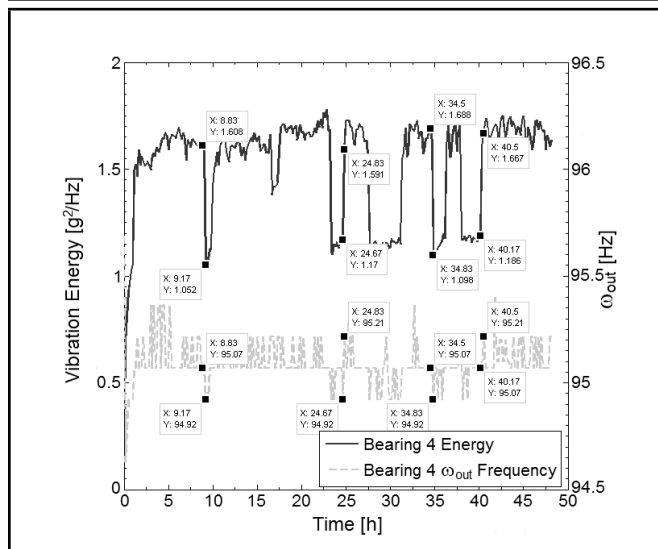


**Figure 10.** Experiment 1 vibration energy vs. the fundamental  $\omega_{out}$  frequency for Bearing 4.

Fig. 10. The  $\omega_{out}$  frequency at the previously selected four data points in the vibration energy (signifying the start of an increase or decrease in temperature) were compared to the next lowest or highest vibration data point available. Referring to Fig. 10, the two data points examined at 8.83 and 34.50 hours into the test occurred prior to a sudden decrease in vibration energy at 9.17 and 34.83 hours, respectively. In both cases, the frequency  $\omega_{out}$  decreased from 95.07 to 94.92 Hz. Conversely, the two points selected at 24.67 and 40.17 hours into the test took place approximately 10 to 20 minutes prior to an increase in the vibration energy. An increase in the  $\omega_{out}$  frequency from 94.92 to 95.21 Hz was observed from 24.67 to 24.83 hours. At 40.17 hours,  $\omega_{out}$  increased from 95.07 to 95.21 Hz within 19.8 minutes. Hence, Fig. 10 demonstrates the shift to lower frequencies (i.e., slowing down) during a temperature uptrend, and a shift to higher frequencies (i.e., speeding up) during a temperature downtrend. The aforementioned is further validation that vibration-induced roller-misalignment is responsible for the temperature trending phenomenon seen in field service.

### 5.1.2. Experiment 2

Experiment 2 was performed at a speed of 95.56 km/h (60 mph, 560 rpm) with a 17% load (empty railcar) and a cup spall on Bearing 4 positioned 10 degrees into the load zone (10° referring to Fig. 4). Bearing 2, a class F defect-free top-loaded bearing, experienced a sharp rise in temperature approximately 60 hours into the test, as can be seen in Fig. 11. To demonstrate the effects of vibration on temperature, the temperature profile for Bearing 2 is juxtaposed in Fig. 11 with the corresponding vibration energy. The vibration energy exhibited a significant decrease moments prior to the abrupt increase in temperature. The vibration energy for Bearing 2 began to drop dramatically at approximately 59.75 hours into the test, which was followed by a rapid rise in temperature that started at approximately 59.92 hours (10.2 minutes later). Again, the most likely explanation for the decrease in the vibration energy of Bearing 2 is roller-misalignment which causes frictional heating resulting from metal-to-metal contact (i.e., rollers sliding on the bearing raceways rather than rolling). The short period between the initial decrease in vibration energy and the onset of the sharp increase in the temperature of Bearing 2 seems to suggest a multiple-roller mis-

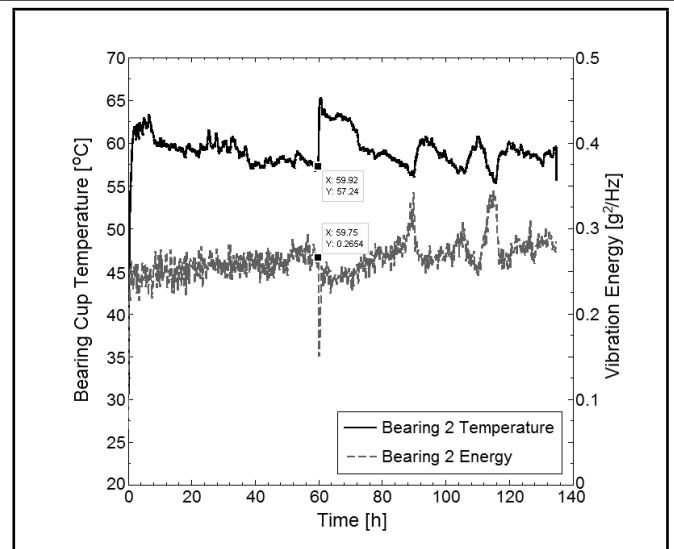


**Figure 11.** Experiment 2 bearing temperature vs. vibration energy; class F bearings; spall placement: 10° (refer to Fig. 4); speed: 96.56 km/h (60 mph); load: 17% (empty railcar).

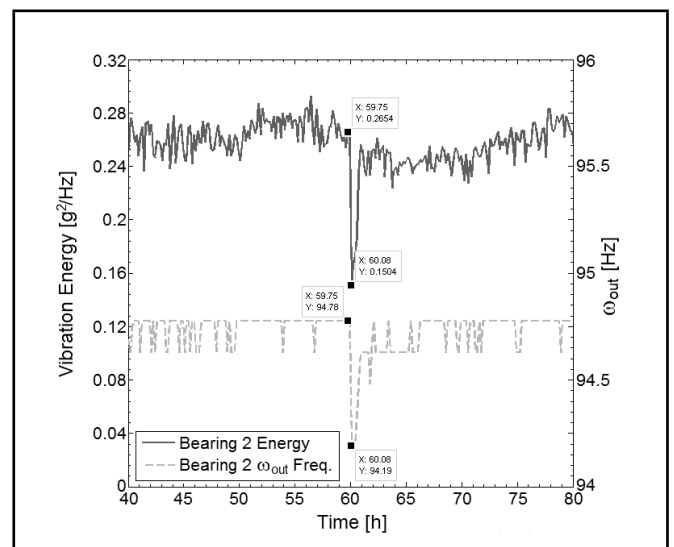


**Figure 12.** Experiment 2 vibration energy vs. the fundamental  $\omega_{out}$  frequency for Bearing 2.

alignment, which can generate significant heating in short time periods.<sup>19</sup> Note that, unlike the previous case of a defective trended bearing, the sudden change in energy at approximately 60 hours into the test did not affect the vibration energy of the other three bearings on the axle.

The fundamental  $\omega_{out}$  frequency for Bearing 2 is plotted in Fig. 12 alongside the vibration energy acquired using the radial accelerometer. It can be seen from Fig. 12 that the major drop in vibration energy observed between 59.75 and 60.08 hours is accompanied by a significant drop in the  $\omega_{out}$  frequency, which decreased from 94.78 Hz to 94.19 Hz during that 20-minute interval. Although there were many small fluctuations in the rotational frequency of  $\omega_{out}$ , none were as big or accompanied by as sharp of an increase in temperature as the one occurring at 59.75 hours. A drop in the  $\omega_{out}$  rotational frequency of approximately 0.6 Hz suggests a multiple-roller misalignment scenario, which explains the abrupt increase in bearing temperature and decrease in the vibration energy caused by the rollers sliding on the raceways.



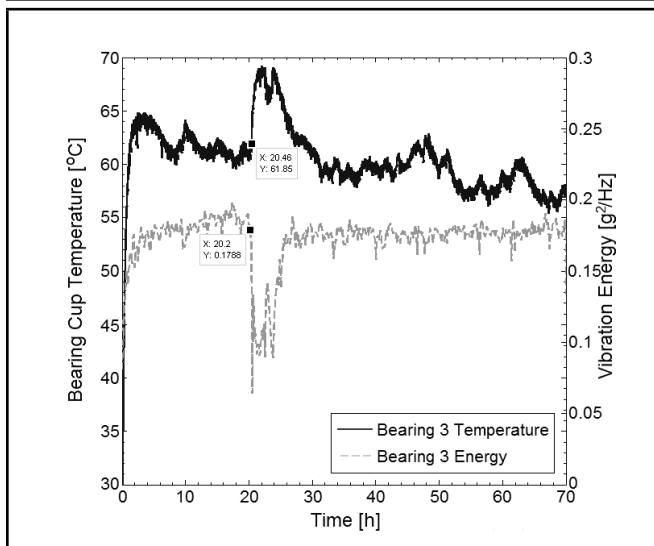


**Figure 13.** Experiment 3 bearing temperature vs. vibration energy; class F bearings; spall placement:  $350^\circ$  (refer to Fig. 4); speed: 85.30 km/h (53 mph); load: 100% (fully-loaded railcar).

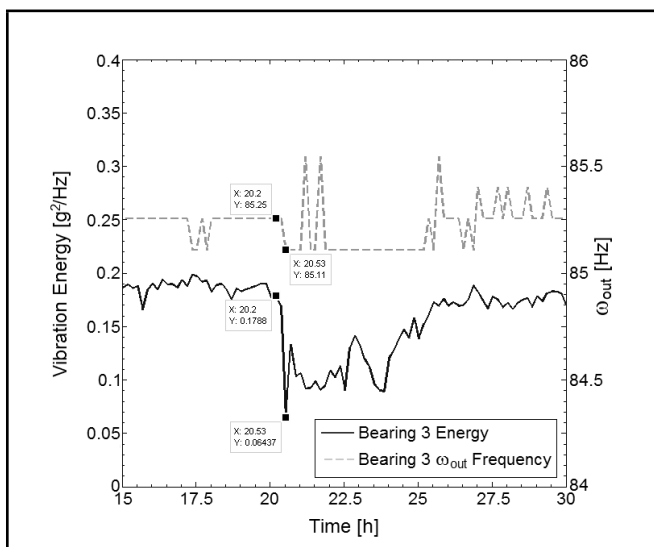


**Figure 14.** Experiment 3 vibration energy vs. the fundamental  $\omega_{out}$  frequency for Bearing 3.

### 5.1.3. Experiment 3

Experiment 3 was conducted at a speed of 85.30 km/h (53 mph, 498 rpm) with a 100% load (simulating a fully-loaded railcar) and a cup spall on Bearing 4 positioned 10 degrees before the start of the load zone ( $350^\circ$  referring to Fig. 4). As in Experiment 2, Bearing 3, a class F defect-free top-loaded bearing, exhibited a rapid increase in temperature approximately 20 hours into the test, as seen in Fig. 13. To exemplify the effects of vibration on temperature, the temperature profile for Bearing 3 is juxtaposed in Fig. 13 with the corresponding vibration energy of that bearing. It can be observed that the energy began to decrease markedly at approximately 20.2 hours into the test, which was then followed by a sharp increase in the bearing temperature that initiated at 20.46 hours (15.6 minutes later). The temperature response time lag can be explained by the thermal time constant of tapered-roller bearings. It takes some time for the bearing cup, where the temperature is being measured, to sense the effects of the frictional heating caused by roller-misalignment and slipping. Depending on the degree of

roller-misalignment and the number of rollers that are caught misaligned, the amount of frictional heating produced within the bearing can vary dramatically.<sup>7,19</sup> The latter accounts for the variations seen in the thermal time constant of the bearing, which can range anywhere from about one minute and up to 25 minutes depending on the severity of roller-misalignment and the number of jammed rollers. Note that the temperature trending experienced by Bearing 3 (a defect-free bearing) did not have any noticeable effect on the vibration energy of the other three bearings on the axle.

The primary  $\omega_{out}$  frequency for Bearing 3 is presented in Fig. 14 next to the vibration energy measured by the radial accelerometer. A drop in the vibration energy of the bearing is observed from 20.2 hours to 20.53 hours into the test. During that period, the  $\omega_{out}$  frequency decreased from 85.25 Hz to 85.11 Hz suggesting a slight decrease in the rotational speed of the roller-cage brought on by roller misalignment. The figure also shows that the decrease in the  $\omega_{out}$  frequency persists throughout the period in which the total vibration energy experiences a downtrend (i.e., between 20 and 25.5 hours in the test), which is indicative of consistent roller-misalignment during that time period. As soon as the vibration energy of the bearing begins to rise again, indicating a return to normal operation of rolling without skidding, the temperature of the bearing starts to drop again.

### 5.1.4. Experiment 4

Experiment 4 is an accelerated class K lifetime test carried out at a speed of 138.40 km/h (86 mph, 796 rpm) with 125% of full-load (simulating an overloaded railcar). All the bearings used in this test were healthy bearings with no known defects. The temperature profiles and bearing vibration energies are presented in Fig. 15 and Fig. 16, respectively. The two outer bearings of the axle-bearing assembly, Bearings 1 and 4, exhibited a noticeable drop in their vibration energy moments before they experienced an abrupt increase in their temperature. The latter suggests a synchronized roller-misalignment event.

Looking at Fig. 17, in which the temperature profile of Bearing 4 is juxtaposed with the corresponding vibration energy, one can notice that the energy began to decrease at approximately 273.5 hours into the test, which was then followed by a sudden increase in the bearing temperature observed at 273.8 hours (i.e., 18 minutes later). Moreover, at approximately 317.3 hours into the test, the vibration energy of Bearing 4 started to increase, which was closely followed by a decrease in temperature at about 317.5 hours (i.e., 12 minutes later). In fact, Fig. 17 clearly demonstrates that each increase in bearing temperature is preceded by a decrease in the vibration energy of the bearing, including the small temperature fluctuation that occurred around 322.5 hours into the test.

The detection of slip caused by roller misalignment is easier to identify in an experiment running at high speeds and loads. Increasing the applied load on bearings decreases the radial clearance, which creates better contact between the roller and the cone and cup raceways. Operating at high speeds and loads tends to increase the bearing temperature, which in turn reduces the viscosity of the grease and shrinks the elastohydrodynamic (EHD) lubricant film that exists between the rolling surfaces. In extreme conditions, grease starvation can occur, which leads to significant roller slipping that results in metal-to-metal frictional heating. As demonstrated earlier, changes

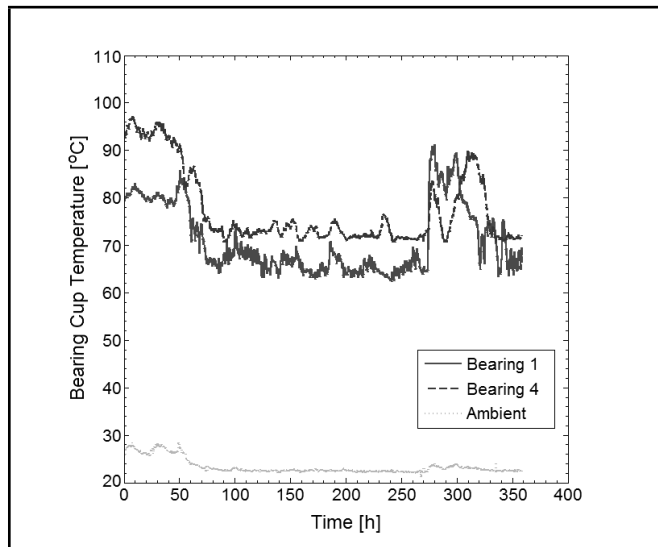


**Figure 15.** Experiment 4 bearing temperature profiles; defect-free class K bearings; speed: 138.40 km/h (86 mph); load: 125% (overloaded railcar).

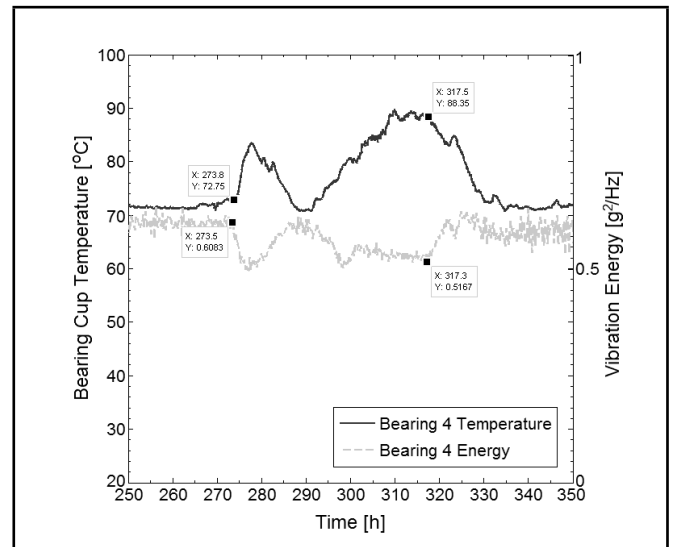


**Figure 17.** Experiment 4 temperature profile vs. vibration energy for Bearing 4.

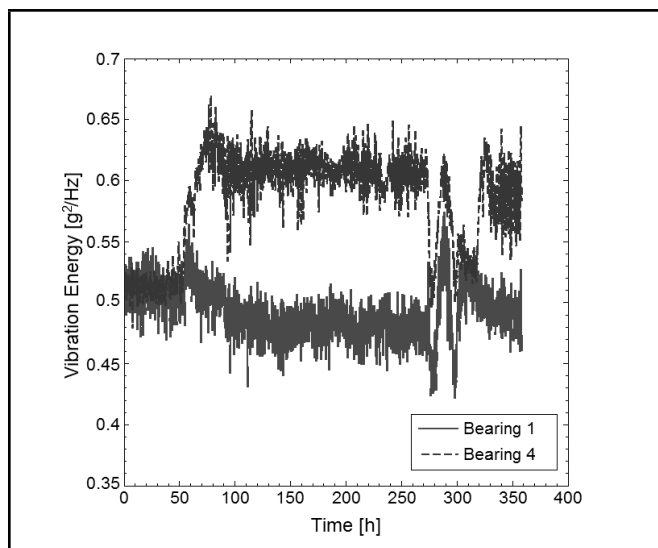


**Figure 16.** Experiment 4 vibration energy captured by radial accelerometers.

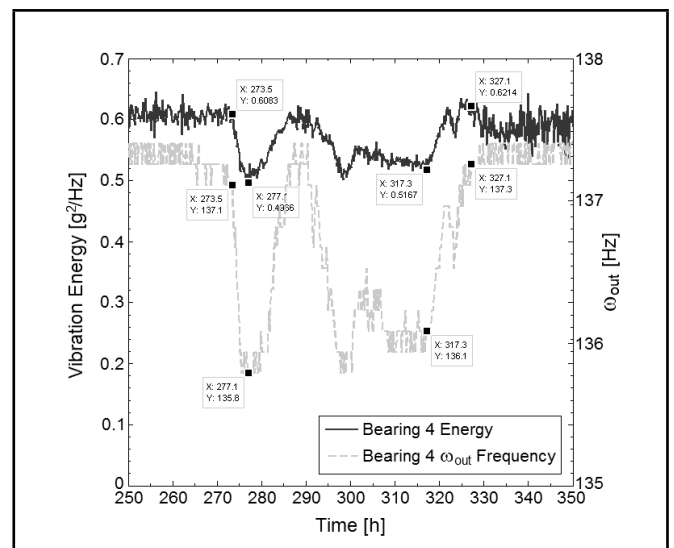


**Figure 18.** Experiment 4 vibration energy vs. the fundamental  $\omega_{out}$  frequency for Bearing 4.

in vibration energy within the bearing precede those in temperature. The decrease in the vibration energy within the bearing is attributed to roller slipping which is demonstrated by a decrease in the fundamental  $\omega_{out}$  frequency. Looking at Fig. 18, a significant decrease of 1.3 Hz is observed in the  $\omega_{out}$  frequency over the period between 273.5 hours and 277.1 hours into the test, which corresponds to the time the vibration energy of the bearing reaches its lowest value. The figure also illustrates how the  $\omega_{out}$  frequency closely mimics the trends exhibited by the vibration energy of the bearing throughout the test. Note that, as soon as the bearing vibration energy returns to normal operation levels (indicating rolling without slipping), so does the  $\omega_{out}$  frequency and the bearing operating temperature.

### 5.1.5. Experiment 5

Experiment 5 was performed at sub-zero ( $-22.5^{\circ}\text{C}$ ) ambient temperature conditions utilizing the bearing dynamic tester housed in the environmental chamber. Four class K healthy (defect-free) bearings were used in this test and were run at a speed of 40.23 km/h (25 mph, 233 rpm) under 17% load simulating an empty railcar. The bearing temperature histo-

ries along with the motor power consumption during the test are provided in Fig. 19, and the corresponding vibration energy plots are given in Fig. 20. The latter two figures provide yet one more example that validates the hypothesis proposed in this paper.

At very low operating temperatures, such as those experienced by the bearings in this experiment, the lubricating grease is very viscous (thick) and creates resistance to the rolling motion, preventing the rollers from normal operation and causing them to misalign and skid along the raceways. Looking at Fig. 20, it can be observed that the grease-induced roller misalignment produces the same effects as the vibration-induced roller misalignment. Whenever roller-misalignment occurs, the vibration energy of the bearing decreases as a result of the reduced epicyclical speed, which is then followed by an increase in the temperature of the bearing resulting from the frictional heating generated by skidding of the roller(s) on the raceways. As the bearing heats, the grease becomes less viscous in the vicinity of the skidding roller(s), thus, allowing the rollers to return to normal operation, which is indicated by the observed increase in the vibration energy of the bearing.

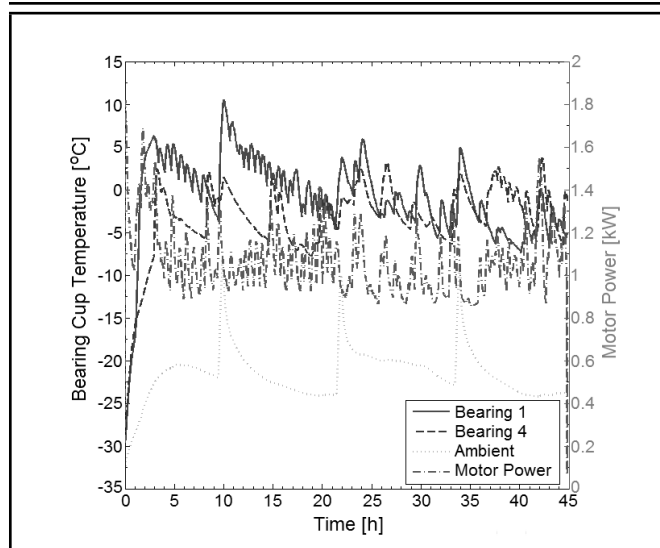


**Figure 19.** Experiment 5 bearing temperature profiles vs. motor power; defect-free class K bearings; freezing ambient conditions; speed: 40.23 km/h (25 mph), load: 17% (empty railcar).

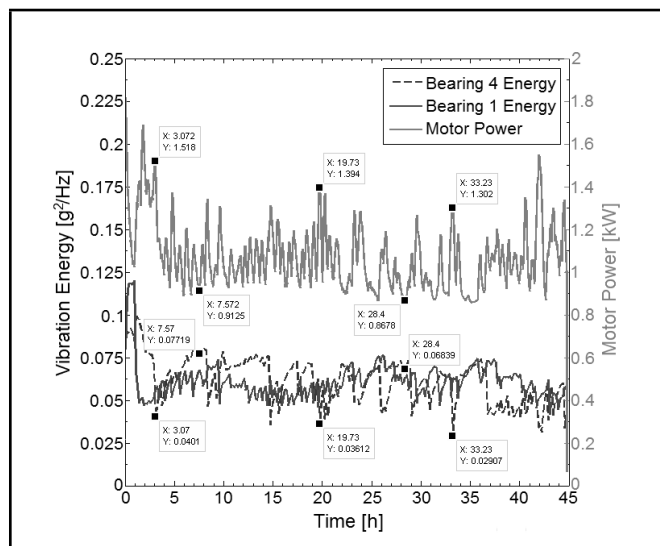


**Figure 20.** Experiment 5 vibration energy captured by radial accelerometers vs. motor power.

The motor power profile, seen in Fig. 19 and more clearly in Fig. 20, supports the abovementioned observations as the power consumption is found to increase prior to a rise in temperature and drops just before the bearing temperatures start decreasing. The increase in power consumption is expected as the motor (which is managed by a smart controller) is trying to overcome the resistance to the rolling motion caused by the roller-misalignment in an attempt to maintain the axle rotational speed within  $\pm 0.5\%$ . As soon as the rollers return to normal operating conditions, the motor power drops, which is then followed by a decrease in the bearing temperatures. Further proof is found in Fig. 20, which illustrates that instances of maximum motor power consumption correspond to instances of minimum vibration energy and vice versa. Note that the abrupt changes in ambient temperature, seen in Fig. 19, are caused by the commercial freezer unit defrost cycle which commences every 10 to 15 hours.

## 6. CONCLUSIONS

The ability to differentiate between defective (faulty) bearings and defect-free (healthy) bearings that are undergoing a temperature trending event is of utmost importance to the railroad industry as this will significantly reduce the number of unnecessary, and very costly, train stoppages associated with *non-verified* bearing removals and/or inspections. This study presents an experimentally validated technique that utilizes the vibration energy approach to identify and differentiate the temperature trending phenomenon exhibited by some defect-free (healthy) bearings in field service.

The technique is built on the hypothesis that, during a bearing temperature-trending event, the vibration energy will decrease prior to a temperature uptrend and will start increasing moments before a temperature downtrend. The aforementioned behaviour is triggered by vibration-induced roller-misalignment. Misaligned roller(s) will slide on the raceways and create a tighter fit between bearing components, thus, slowing the epicyclic speed and producing less vibration than that of pure rolling motion. Meanwhile, the roller-skidding will generate excessive metal-to-metal frictional heating caused by thinning of the elastohydrodynamic (EHD) lubricant film, which accounts for the observed rise in bearing temperature. Once the roller(s) return to normal operation, the vibration energy of the bearing will increase back to its original level and the bearing temperature will start to drop.

This paper provides sufficient experimental proof to validate the proposed hypothesis. The relationship between vibration energy and temperature is further verified by the shift in the  $\omega_{out}$  frequency, which is dependent on the fundamental frequency of the cage. A shift to a lower  $\omega_{out}$  frequency indicates that the rotational frequency of the cage has slowed down from its epicyclic motion due to the friction caused by roller misalignment. A decrease in the bearing temperature or return-to-normal operating temperature would be caused by geometrical thermal expansions and roller realignment. During the reduction in cage pocket and radial clearances, the rollers pivot as they attempt to realign, promoting grease flow and momentarily speeding up and causing fluctuations in the rotational speed of the cage.

The abovementioned behaviour is observed in numerous laboratory experiments, and the technique presented here is consistent in identifying the bearing temperature trending phenomenon. The selected tests discussed in this paper varied from setups containing bearings with known defects that would trigger vibration-induced roller misalignment to experiments conducted with all defect-free bearings run at high speeds and loads or low ambient conditions. Note that roller misalignment is not only triggered by vibrations from neighbouring sources, it can be caused by many factors including inadequate lubrication conditions, grease degradation, loose cone assemblies, high operating speeds and loads, or simply low ambient temperatures that significantly increase the grease viscosity and cause grease-induced roller misalignment.

In the case of a defective (faulty) bearing, the vibration energy levels and the bearing temperature will be noticeably higher than those of normal operation—see Fig. 7 and Fig. 8 and compare the defect-free Bearing 1 to the defective Bearing 4, which contains a spalled cup raceway—and the vibration energy of the bearing will continue to increase as the defect worsens with continued operation. Ongoing work in this area is focused on acquiring vibration signatures at different oper-

ating speeds and loads from a variety of healthy and defective bearings to cover a wide range of defects and abnormal operating conditions. The objective is to create an inclusive vibration energy database library that can be used to contrast defect-free bearings and known bearing cup, cone, cage, and roller defects. The latter work combined with the technique presented in this paper will facilitate the development of a comprehensive bearing condition monitoring algorithm that will contribute to a much improved railway safety while reducing the costly train stoppages and delays associated with false bearing setouts and inspections.

## REFERENCES

- <sup>1</sup> Karunakaran, S. and Snyder, T. W. Bearing temperature performance in freight cars, *Proceedings of the Bearing Research Symposium sponsored by the AAR Research Program in conjunction with the ASME RTD 2007 Fall Technical Conference*, Chicago, Illinois, September 11–12, (2007).
- <sup>2</sup> Anderson, G. B. Acoustic detection of distressed freight car roller bearing, *Proceedings of the 2007 JRCICE Spring Technical Conference*, Pueblo, Colorado, March 13–16, (2007).
- <sup>3</sup> Wiley, R. B. and Snyder, T. Technical Report, From ATSI to TDTI: Existing Technologies Analysis and Statistical Review Future Technologies, Transportation Technology Center, Inc. and Union Pacific Railroad, (2011).
- <sup>4</sup> Farnfield, N. E. Thermal investigations of roller bearings, *Tribology*, **5** (3), 104, (1972).
- <sup>5</sup> Dunnuck, D. L. Steady-state temperature and stack-up force distributions in a railroad roller bearing assembly, M.S. thesis, University of Illinois at Urbana-Champaign, Urbana, Illinois, (1992).
- <sup>6</sup> Wang, H. Axle burn-off and stack-up force analyses of a railroad roller bearing using the finite element method, Ph.D. dissertation, University of Illinois at Urbana-Champaign, Urbana, Illinois, (1996).
- <sup>7</sup> Wang, S., Cusano, C., and Conry, T. F. A dynamic model of the torque and heat generation rate in tapered roller bearings under excessive sliding conditions, *Tribology Transactions*, **36** (4), 513–524, (1993).
- <sup>8</sup> Kletzli, D. B., Cusano, C., and Conry, T. F. Thermally induced failures in railroad tapered roller bearings, *Tribology Transactions*, **42** (4), 824–832, (1999).
- <sup>9</sup> Jamison, W. E., Kauzlarich, J. J., and Mochel, E. V. Geometric effects on the rib-roller contact in tapered roller bearings, *ASLE Transactions*, **20** (1), 79–88, (1977).
- <sup>10</sup> Sunnersjö, C. S. Rolling bearing vibrations—The effects of geometrical imperfections and wear, *Journal of Sound and Vibration*, **98** (4), 455–474, (1985).
- <sup>11</sup> Gupta, P. K. On the dynamics of a tapered roller bearing, *Journal of Tribology*, **111** (2), 278–287, (1989).
- <sup>12</sup> Su, Y.-T., Lin, M.-H., and Lee, M.-S. The effects of surface irregularities on roller bearing vibrations, *Journal of Sound and Vibration*, **165** (3), 455–466, (1993).
- <sup>13</sup> Ohta, H. and Sugimoto, N. Vibration characteristics of tapered roller bearings, *Journal of Sound and Vibration*, **190** (2), 137–147, (1996).
- <sup>14</sup> Su, Y.-T. and Lin, S.-J. On initial fault detection of a tapered roller bearing: frequency domain analysis, *Journal of Sound and Vibration*, **155** (1), 75–84, (1992).
- <sup>15</sup> Yang, Y., Danyluk, S., and Hoepflich, M. A study on rolling element skew measurement in a tapered roller bearing with a specialized capacitance probe, *Journal of Tribology*, **122** (3), 534–538, (2000).
- <sup>16</sup> Tarawneh, C., Cole, K., Wilson, B., and Reed, M. A metallurgical and experimental investigation into sources of warm bearing trending, *Proceedings of the 2008 IEEE/ASME Joint Rail Conference*, Wilmington, Delaware, April 22–24, (2008).
- <sup>17</sup> Tarawneh, C., Cole, K., Wilson, B., and Freisen, K. A lumped capacitance model for the transient heating of railroad tapered roller bearings, *Proceeding of the 2007 ASEE-GSW Annual conference*, March 28–30, (2007).
- <sup>18</sup> Tarawneh, C., Cole, K., Wilson, B., and Alnaimat, F. Experiments and models for the thermal response of railroad tapered roller bearings, *International Journal of Heat and Mass Transfer*, **51**, 5794–5803, (2008).
- <sup>19</sup> Tarawneh, C., Fuentes, A. A., Kypuros, J. A., Navarro, L. A., Vaipan, A. G., and Wilson, B. M. Thermal modeling of a railroad tapered roller bearing using finite element method, *Journal of Thermal Science and Engineering Applications*, **4** (3), 9–19, (2012).
- <sup>20</sup> Tarawneh, C., Wilson, B. M., Cole, K. D., Fuentes, A. A., and Cardenas, J. M. Dynamic bearing testing aimed at identifying the root cause of warm bearing temperature trending, *Proceedings of the 2008 ASME RTD Fall Technical Conference*, RTDF2008–74036, Chicago, Illinois, September 24–26, (2008).
- <sup>21</sup> Tarawneh, C., Kypuros, J. A., Wilson, B., Snyder, T. W., Fuentes, A. A., and Gonzalez, B. A. A collaborative on-track field test conducted to verify the laboratory findings of bearing temperature trending, *Proceedings of the 2009 ASME Joint Rail Conference*, Pueblo, Colorado, March 3–5, (2009).
- <sup>22</sup> Tarawneh, C., Kypuros, J. A., Fuentes, A. A., Wilson, B. M., Gonzalez, B. A., Rodriguez, G., and Maldonado, R. K. Vibration signatures of temperature trended bearings in field and laboratory testing, *Proceedings of the 2009 ASME RTD Fall Technical Conference*, RTDF2009-18038, Ft. Worth, Texas, October 20–21, (2009).
- <sup>23</sup> FFTW, Retrieved from <http://www.fftw.org>, (Accessed January 14, 2013).
- <sup>24</sup> Frigo, M. and Johnson, S. G. FFTW: An Adaptive Software Architecture for the FFT, *Proceedings of the International Conference on Acoustics, Speech, and Signal Processing*, **3**, 1381–1384, (1998).
- <sup>25</sup> Gonzalez, B. A. A study of the effect of vibration on railroad bearing temperature, M.S. Thesis, University of Texas Pan-American, Edinburg, Texas, (2010).

---

---

# Usage of Spectral Distortion for Objective Evaluation of Personalized HRTF in the Median Plane

**Fabián C. Tommasini**

*Facultad de Matemática, Astronomía y Física (FaMAF), Universidad Nacional de Córdoba, Argentina.  
Centro de Investigación y Transferencia en Acústica (CINTRA), Unidad Asociada del CONICET, Universidad Tecnológica Nacional, Facultad Regional Córdoba, Argentina.*

**Oscar A. Ramos**

*Centro de Investigación y Transferencia en Acústica (CINTRA), Unidad Asociada del CONICET, Universidad Tecnológica Nacional, Facultad Regional Córdoba, Argentina.  
Consejo Nacional de Investigaciones Científicas y Técnicas (CONICET), Argentina.*

**Mercedes X. Hüg and Fernando Bermejo**

*Centro de Investigación y Transferencia en Acústica (CINTRA), Unidad Asociada del CONICET, Universidad Tecnológica Nacional, Facultad Regional Córdoba, Argentina.*

(Received 28 November 2012; accepted 10 July 2014)

Measuring the head-related transfer functions (HRTFs) for each subject is a complex process. Therefore, it is necessary to develop procedures that allow the estimation of personalized HRTFs. It is common to estimate the weights of the principal component analysis (PCA) of a group of subjects based on some anthropometric parameters using multivariable regression modelling. Moreover, to objectively evaluate the goodness of fit between the original HRTFs and the personalized ones, the spectral distortion (SD) is usually used too. However, its suitability in the median plane, in which the spectral profiles are crucial to localize a sound source, has not yet been demonstrated. This paper analyses the validity of the SD as a measure of the quality of the HRTF personalization in the median plane, from the localization point of view. The HRTFs were modelled from the weights estimated by multiple linear regression and artificial neural networks (ANNs). The SD was used to compare the HRTFs measured with those estimated. Likewise, the level of fitting accuracy of characteristic resonance and notches in the median plane was also compared. Despite the fact that the SD scores of ANNs are lower than those of the multiple linear regression and are similar to those reported by other studies, the errors obtained from analysing both central frequencies and levels for resonance and notches could be discriminated.

---

## 1. INTRODUCTION

The purpose of the acoustic virtual reality (AVR) is to recreate the hearing experience that a person would undergo in a real environment, thus provoking a feeling of immersion in that environment. The principle that supports acoustic simulations states that acoustically equivalent stimuli produce equivalent sensations.<sup>1</sup> That is to say, if the biologically correct signals are applied to a listener's eardrums by means of headphones, it will be possible to stimulate the listener's feeling of immersion in the modelled environment.<sup>2</sup>

In an AVR system, the sound source, the room, and the listener must be modelled. Basically, the sound source is specified by the directivity characteristics and the frequency response; the room by its impulse response between a sound source and a receiver; and the listener by the head-related impulse responses (HRIRs) in the time domain, or the head-related transfer functions (HRTFs) in the frequency domain.

Due to the separation between both ears, the sound waves travel different paths, causing an interaural time difference (ITD), and, according to the position of the sound source, one of the ears may remain hidden by the head, thus also originating an interaural level difference (ILD). These two phenomena, together with the frequency spectra, are cues that humans use

to localize a sound source in space.<sup>1</sup>

Each HRTF contains all the transformations produced in a sound wave before reaching a listener's eardrums when interacting with the head, pinna, torso, and shoulders. It is different for each ear and varies systematically with the location of the sound source. It is known that a HRTF not only depends on this, but also on the subject's anatomical characteristics: head and pinna size, and shoulders and torso width, among others.

If the HRTFs used correspond to the listener, the source is perceived as compact, external, and well defined in a position in space. By contrast, if they belong to another individual, the source is perceived as diffuse, located in the interior of the head, and the front-back confusion increases.<sup>1,3</sup> This means that it is essential to measure a subject's own HRTFs to experience a genuine perception of space. However, these measurements are complex and expensive and require special equipment. Therefore, it is necessary to develop procedures that allow estimating personalized HRTFs by means of simpler and less expensive approaches.

Different studies have addressed the problem of personalizing the HRTFs in different ways. A review of the methods can be consulted in Xu et al.,<sup>4</sup> in which seven potential methods for HRTF personalization were identified. One of these methods obtains the relation between some individual's anthropo-

metric measurements and the log-magnitude of the HRTFs by the multiple linear regression method (e.g.<sup>5-9</sup>). Based on the fact that the influence of the head, pinna and torso is of complex characteristics, other authors resort to non-linear regression methods.<sup>10, 11</sup>

To objectively evaluate the goodness of fit between the original HRTFs and the personalized ones, the spectral distortion (SD)<sup>12</sup> is usually used, i.e., the euclidean distance between two spectra integrated in the entire frequency range. This value is often used as an index that indicates the personalization error in order to determine whether a set of personalized HRTFs is acceptable or not.

Generally, HRTF modelling may produce sound timbre changes and localization errors.<sup>13</sup> For example, every single dB change in the high midrange will be audible and will change the perceived sound timbre.<sup>14</sup> The SD could represent the differences in timbre between measured and personalized HRTF. In a similar direction, Mahé et al.<sup>15</sup> used the SD to assess the transmitted speech across a telephone link. They proposed an equalizer that reduces the SD between the received and transmitted speech, which perceptually means a better timbre correction for some speakers. However, from the localization point of view, the suitability of the SD in the median plane has not yet been demonstrated. The aim of this paper is to analyse the validity of the SD as a measure of the quality of the HRTF personalization in the median plane. Personalized HRTFs will be modelled using multiple linear regression and artificial neural networks—both methods usually used in horizontal plane.

Below, Section 2 explains the methodology followed: the HRIR database used, the preprocessing applied and the selection of the relevant anthropometric parameters. Section 3 describes the methods used: multiple linear regression and artificial neural networks. Section 4 shows the results discussed in Section 5. Finally, Section 6 presents the conclusions.

## 2. METHODOLOGY

### 2.1. The Database

The public-domain HRIR database measured in the Center for Image Processing and Integrated Computing (CIPIC) of the University of California was used.<sup>16</sup> It contains the HRIRs of 47 subjects in 1250 positions in sphere per subject and per ear. The location of the sound source is specified by the azimuth angle  $\theta$  (25) and the elevation angle  $\phi$  (50) in an interaural-polar coordinate system, with reference to the interaural axis that goes through both ears. The HRIRs are sequences of 200 points sampled at 44.1 kHz, compensated in the free-field, and measured to the blocked entrance of the ear canals. The subject remained seated at the center of a hoop with a radius of 1 m. The elevations vary uniformly in steps of  $5.625^\circ$  between  $-45^\circ$  and  $+230.625^\circ$ . The azimuth angles are  $-80^\circ, -65^\circ, -55^\circ$ , from  $-45^\circ$  to  $+45^\circ$  in steps of  $5^\circ, +55^\circ, +65^\circ$  and  $+80^\circ$ . Azimuth  $0^\circ$  and elevation  $0^\circ$  corresponds directly ahead of the subject; azimuth  $0^\circ$  and elevation  $+180^\circ$  behind the subject; negative azimuth to the left and positive ones to the right of the subject; negative elevations and those higher than  $+180^\circ$  below the interaural axis ahead and behind, respectively.

The CIPIC database also includes 37 anthropometric parameters (Table 1) measured of just 35 subjects. The anthropomet-

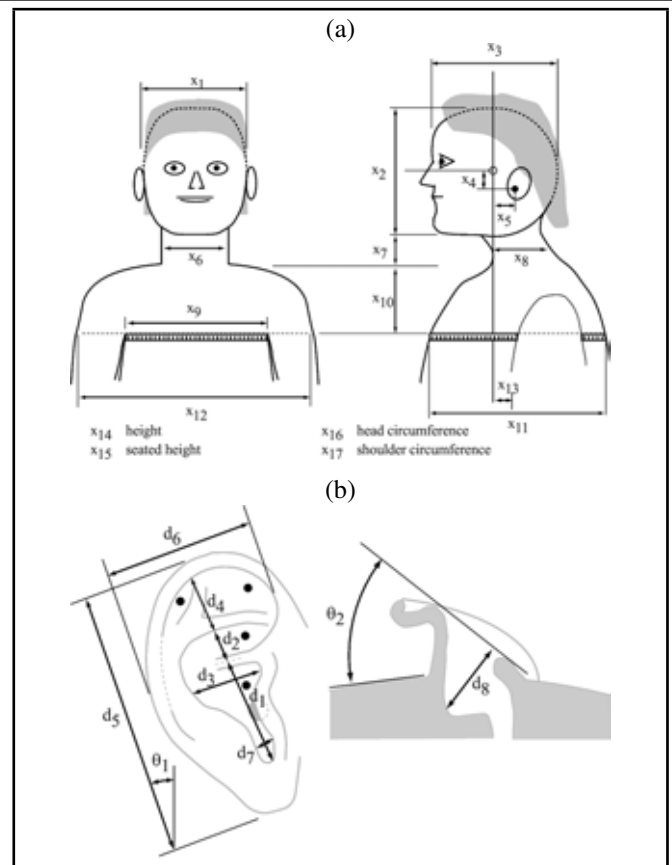


**Figure 1.** Anthropometric measurements of CIPIC database:<sup>17</sup> (a) head and torso measurements, and (b) pinna measurements.

ric measurements consist on 17 for the head and torso (Fig. 1a), and 10 for each pinna (Fig. 1b). In the present study were only included these 35 subjects that have both HRIRs as anthropometric parameters.

### 2.2. Preprocessing

The corresponding HRTFs were obtained by performing the discrete Fourier transform of the HRIRs (zero-padded up to 256 samples). As the bandwidth under study was 0–15 kHz,<sup>18</sup>  $N = 88$  frequency components were selected (from 0 to 14.987 kHz with a resolution of about 172 Hz).

Of the 35 subjects selected, a randomly chosen group of  $Q = 5$  (called S5) was separated to validate the personalized HRTFs by both methods. For the  $P = 30$  remaining subjects (called S30), the mean  $\mu_h$  across all subjects, positions and both ears of the base 10 log-magnitude responses of the HRTFs was calculated.<sup>18</sup> This value was subtracted from each HRTF to eliminate common characteristics of the group S30, thus obtaining the preprocessed HRTFs  $h_p$  for the subject  $p$ . Then, the principal component analysis (PCA) method was applied to this group. The PCA transforms a number of correlated variables into the same number of non-correlated variables (principal components, PCs). In addition, by reducing its dimensionality, it highlights common characteristics and reveals hidden patterns in the group.<sup>19</sup>

The application of this method results in an  $N \times N$  orthonormal transformation matrix  $\mathbf{C}$ , which contains the PCs, and a  $P \times N$  weight matrix  $\mathbf{W}$  for each position and each ear. Any HRTF of a subject  $p$  for a specific position  $(\theta, \phi)$  can be com-

**Table 1.** List of anthropometric measurements included in the CIPIC database.<sup>17</sup>

Variable	Measurement	Variable	Measurement	Variable	Measurement
$x_1$	Head width	$x_{10}$	Torso top height	$d_2 \times 2$	Cymba concha height
$x_2$	Head height	$x_{11}$	Torso top depth	$d_3 \times 2$	Cavum concha width
$x_3$	Head depth	$x_{12}$	Shoulder width	$d_4 \times 2$	Fossa height
$x_4$	Pinna offset down	$x_{13}$	Head offset forward	$d_5 \times 2$	Pinna height
$x_5$	Pinna offset back	$x_{14}$	Height	$d_6 \times 2$	Pinna width
$x_6$	Neck width	$x_{15}$	Seated height	$d_7 \times 2$	Integral incisure width
$x_7$	Neck height	$x_{16}$	Head circumference	$d_8 \times 2$	Cavum concha depth
$x_8$	Neck depth	$x_{17}$	Shoulder circumference	$\theta_1 \times 2$	Pinna rotation angle
$x_9$	Torso top width	$d_1 \times 2$	Cavum concha height	$\theta_2 \times 2$	Pinna flare angle

pletely reconstructed by:

$$\mathbf{h}_p(\theta, \phi) = \mathbf{w}_p(\theta, \phi)\mathbf{C} + \mu_{\mathbf{h}} \quad \text{with } p = 1 \dots P; \quad (1)$$

where  $\mathbf{h}_p$  is a vector with length  $N$  that contains the HRTF for any ear of subject  $p$  belonging to S30,  $\mathbf{w}_p$  is the  $p$ -th row vector of matrix  $\mathbf{W}$ , and  $\mu_{\mathbf{h}}$  is the mean calculated above.

Since the PCs derived from group S30 can be considered generic PCs,<sup>8</sup> they were used to obtain another  $Q \times N$  weight matrix  $\mathbf{W}'$  for each position and each ear for the group S5. Taking Eq. (1) into account, it can be expressed as:

$$\mathbf{w}'_q(\theta, \phi) = (\mathbf{h}_q(\theta, \phi) - \mu_{\mathbf{h}})\mathbf{C}^T \quad \text{with } q = 1 \dots Q; \quad (2)$$

where  $\mathbf{h}_q$  contains the HRTF for any ear of subject  $q$  belonging to S5,  $\mathbf{w}'_q$  is the  $q$ -th row vector of matrix  $\mathbf{W}'$ , and  $\mathbf{C}^T$  is the transpose of  $\mathbf{C}$ .

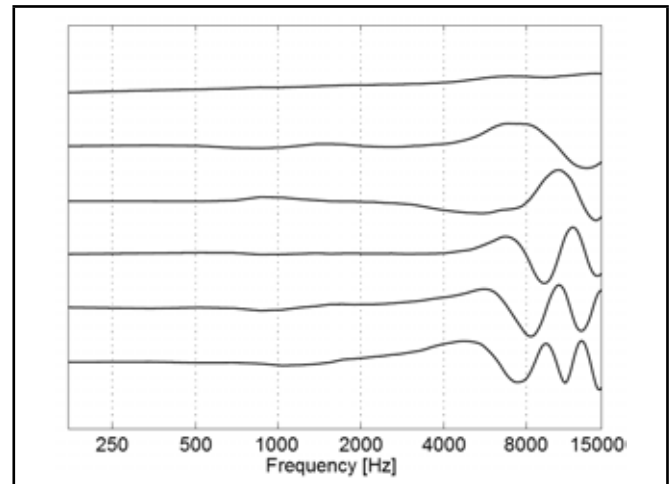
However, to obtain an effective decrease in the original data dimension, a number  $L \ll N$  must be determined so that a given HRTF can be reconstructed within a perceptually acceptable error.<sup>20,21</sup> According to Kistler and Wightman,<sup>18</sup> the first 5 PCs, which express 90% of the total variance of the original log-magnitude HRTFs (according to their database), represent the gradual changes of the HRTFs in the high frequency accompanying the position changes of the sound source.

The first  $L = 6$  PCs were used in this study because its accumulated variance reached up to 90% using the CIPIC database. Figure 2 shows that these PCs are constant and close to zero up to about 2-3 kHz, and, therefore, the personalized HRTFs are independent of the weight values. This suggests that there is no dependence on the direction of incidence of the sound wave in this frequency range. Conversely, PCs variation is noticeable above 3 kHz. These variations contribute to the creation of HRTF peaks and notches, which depend on the direction of the sound waves, and arise due to the pinna dimensions and shapes.<sup>18</sup> Those dimensions are consistent with wavelengths corresponding to frequencies above 3 kHz.

The reconstructed HRTFs for group S5 using  $\mathbf{W}'$  with six PCs will be referred to as  $\text{HRTF}_{\text{ori}}$ .

### 2.3. Anthropometric Parameter Selection

The methodologies for selecting the relevant anthropometric parameters are dissimilar, and the topic is approached almost exclusively as a mathematical problem. In general, the anthropometric parameters selection is based on assuming correlation indexes, higher than a certain arbitrarily adopted value, between these parameters and the log-magnitude of the HRTFs. Certain anthropometric measurements, whose influence in the structure of HRTFs has been demonstrated in the literature, tend to remain excluded. In addition, it calls the attention that the parameters selected by different authors differ, even when


**Figure 2.** High frequency variation of the first 6 PCs (PC#1 at top, PC#6 at bottom).

using the same database.<sup>9,10</sup> In this paper, it is proposed to use those parameters that the literature has demonstrated to be significant in the construction of the HRTFs in the median plane.

Shaw and Teranishi,<sup>22</sup> in 1968, demonstrated the influence of the pinna cavities on the production of characteristic resonances of the external ear and developed an approximate mechanical model using simple geometric shapes.<sup>23,24</sup> In this model, the concha is represented by a cylinder with one of its extremes closed. They proved that the resonance central frequency in 4.2 kHz (called mode 1), present in the HRTFs for all positions, corresponded to  $\lambda/4$ , where  $\lambda$  is the depth of the cylinder (10 mm). From this evidence, the anthropometric measure cavum concha depth ( $d_8$ ) of CIPIC database was used (Table 1). Shaw and Teranishi<sup>22</sup> also demonstrated that if the cylinder is replaced by a rectangular cavity, the first horizontal mode (mode 4 in 12.1 kHz) appears and can be tuned by varying the width of the rectangular cavity ( $\approx 17$  mm). This anthropometric measurement is equivalent to the cavum concha width ( $d_3$ ). To produce the resonances in 7.1 kHz and 14.4 kHz (modes 2 and 5) these authors introduced a barrier in the rectangular cavity which took into account the crus helias. Therefore the following parameters were used of CIPIC database: cavum concha height ( $d_1$ ) and cymba concha height ( $d_2$ ).

The pinna rotation angle ( $\theta_1$ ) was also selected. This parameter is considered to be relevant as it modifies the pinna's orientation in relation to the horizontal plane, which goes through the interaural axis. The impact points of the waves on the posterior wall of the concha change with this angle. According to the reflection theory, the path travelled by the reflections produced in that region determines the notches' central frequencies, which vary systematically with the position of the sound

source and act as the cues that the subject uses to localize a sound source in the median plane.<sup>25-28</sup> The pinna height and width ( $d_5$  and  $d_6$ ), that characterize the pinna size, were also selected.<sup>27</sup>

In summary,  $K = 7$  anthropometric parameters for each ear were selected:  $d_1, d_2, d_3, d_5, d_6, d_8,$  and  $\theta_1$ .

### 3. REGRESSION MODELLING

#### 3.1. Multiple Linear Regression

The method consists of expressing a  $P \times L$  weight matrix  $\mathbf{W}$  (for all the subjects in group S30) for a position  $(\theta, \phi)$  of the sound source as a linear combination of the seven anthropometric parameters selected:

$$\mathbf{W}(\theta, \phi) = \mathbf{X}\mathbf{B}(\theta, \phi) + \mathbf{E}(\theta, \phi); \quad (3)$$

where  $\mathbf{X}$  is the  $P \times K$  matrix of the anthropometric parameters of the subjects of group S30,  $\mathbf{B}$  is the  $K \times L$  regression coefficient matrix, and  $\mathbf{E}$  the  $P \times L$  estimation error matrix.

Then, the regression coefficients are calculated as:<sup>6</sup>

$$\mathbf{B}(\theta, \phi) = (\mathbf{X}^T \mathbf{X})^{-1} \mathbf{X}^T \mathbf{W}(\theta, \phi). \quad (4)$$

With this regression coefficient matrix  $\mathbf{B}$  and the  $Q \times K$  anthropometric parameter matrix  $\mathbf{Y}$  of the subjects of group S5, a  $Q \times L$  weight matrix  $\hat{\mathbf{W}}_{\text{mlr}}$  for these subjects can be estimated as follows:

$$\hat{\mathbf{W}}_{\text{mlr}}(\theta, \phi) = \mathbf{Y}\mathbf{B}(\theta, \phi). \quad (5)$$

Using these estimated weights and Eq. (1), the HRTFs for any subject in group S5 can be reconstructed. These HRTFs will be called  $\text{HRTF}_{\text{mlr}}$ .

#### 3.2. Artificial Neural Networks

An artificial neural network (ANN) is a computational model that is inspired in the human brain, and since one of its main characteristics is its learning capacity, it has been widely used to describe non-linear input/output relationships in different applications. In this case, several ANNs were used to model a non-linear regression between the seven anthropometric parameters and the first six weights of PCA. Feedforward ANNs trained by backpropagation algorithm were implemented.<sup>29</sup> A total of 50 feedforward ANNs for each ear were necessary, i.e., one for each position in the median plane.

Each one of these ANNs has a three-layer architecture with a tan-sigmoid transfer function in the hidden layer and a linear transfer function in the output layer. It has been proven that any continuous function can be uniformly approximated by a backpropagation network with only one hidden layer.<sup>30</sup> The choice of the number of neurons in the hidden layer is very important; however there is no general rule to know this number beforehand. A great number of neurons in this layer offer great flexibility due to the fact that the network has more parameters to be optimized. Yet, if this number becomes too large, it can cause sub-characterization problems and the network has to optimize more parameters than necessary. To estimate this number, the amount of hidden neurons was gradually increased between 5 and 25. The minimum error was reached

with 18 hidden neurons. Therefore, the structure for each ANN was 7-18-6.

The anthropometric parameters and the weights  $\mathbf{w}_p$  of the group S30 were used for the training phase. For the testing phase, the anthropometric parameters and the weights  $\mathbf{w}'_q$  of group S5 were used. In the training and testing phase, both the inputs and outputs were normalized. All the ANNs were trained by the bayesian regularization method for up to 200 iterations to an error goal of 0.02, allowing better generalization. The output performance measurement was the sum of the square errors. This method and the previous one were developed using the MATLAB environment.

The inputs for each network were the seven selected anthropometric measurements, and the outputs were the estimation of first six weights composing the  $Q \times L$  matrix  $\hat{\mathbf{W}}_{\text{ann}}$ .

Now, using the weight matrix  $\hat{\mathbf{W}}_{\text{ann}}$  and Eq. (1), the HRTFs for group S5 were calculated. These HRTFs will be referred to as  $\text{HRTF}_{\text{ann}}$ .

### 4. RESULTS

First, the errors between the  $\text{HRTF}_{\text{ori}}$  and the HRTFs estimated by both methods ( $\text{HRTF}_{\text{mlr}}$  and  $\text{HRTF}_{\text{ann}}$ ) in the median plane were evaluated. The mean square difference of the log-magnitude of the HRTFs was used, i.e., the spectral distortion (SD):<sup>12</sup>

$$\text{SD}(\theta, \phi) = \sqrt{\frac{1}{N} \sum_{i=1}^N \left( h(\theta, \phi, f_i) - \hat{h}(\theta, \phi, f_i) \right)^2} \quad [\text{dB}]; \quad (6)$$

where  $h$  is a frequency component value of the  $\text{HRTF}_{\text{ori}}$ ,  $\hat{h}$  is that estimated ( $\text{HRTF}_{\text{mlr}}$  and  $\text{HRTF}_{\text{ann}}$ ), and  $N = 88$  is the number of frequency components, representing a range of 0–15 kHz.

Figure 3a shows the average SD scores across all subjects of group S5 for all the positions in the median plane and left ear. The SD scores plus/minus one standard deviation obtained by both methods are shown in Fig. 3b. Notice that deviations for the  $\text{HRTF}_{\text{ann}}$  are lower than those for the  $\text{HRTF}_{\text{mlr}}$ . The SD scores obtained with ANNs method are similar, in almost all positions, to those reported by other studies for the horizontal plane.<sup>6,10</sup>

Second, to verify whether any method is significantly better, a  $t$ -test (with significance level  $\alpha = 0.01$ ) to compare one sample mean to an accepted value was carried out for group S5. Given that the average differences of the SD scores of both methods follow a normal distribution, the following hypotheses were stated:

$$\begin{aligned} H_0 &: \overline{\text{SD}}_{\text{ann}} - \overline{\text{SD}}_{\text{mlr}} \geq 0; \\ H_1 &: \overline{\text{SD}}_{\text{ann}} - \overline{\text{SD}}_{\text{mlr}} < 0; \end{aligned} \quad (7)$$

where  $\overline{\text{SD}}_{\text{ann}}$  is the average SD score for the ANNs method and  $\overline{\text{SD}}_{\text{mlr}}$  the average SD score for multiple linear regression. Note that these hypotheses constitute a one-tailed test. The null hypothesis will be rejected if  $\overline{\text{SD}}_{\text{ann}} < \overline{\text{SD}}_{\text{mlr}}$ .

$H_0$  was rejected ( $t = -8.9721, p < 0.01$ ). This implies that the ANNs method has, on average, a significantly lower SD score than that of multiple linear regression for the subjects in group S5. According to this result, the nonlinear regression



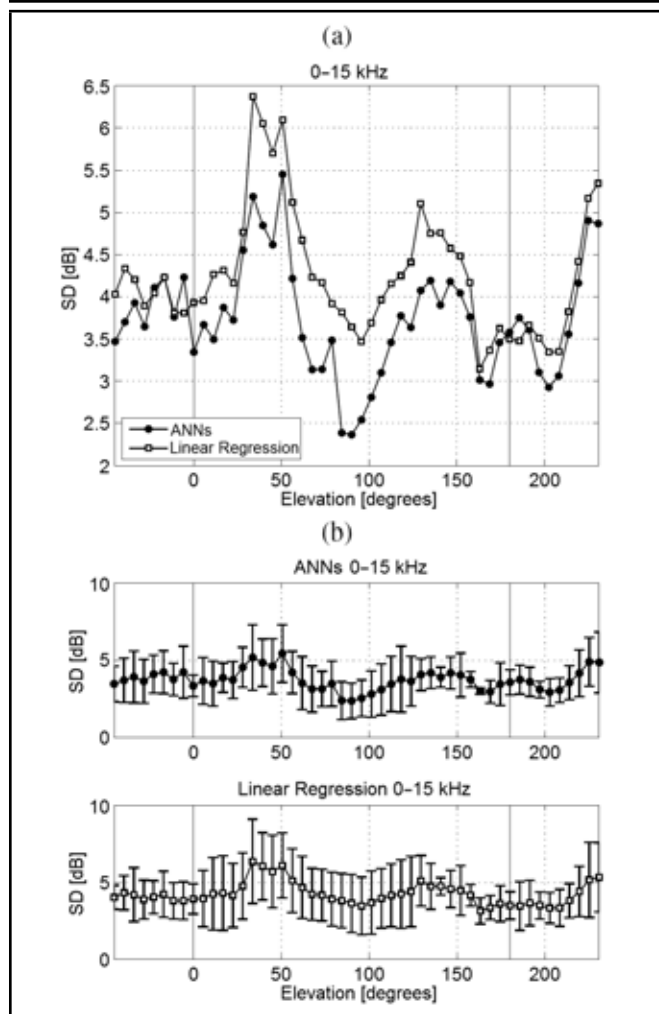


**Figure 3.** (a) Average SD scores across subjects of S5 and (b) standard deviation, for all the positions in the median plane and left ear.

method using ANNs would fit better than the multiple linear regression in the median plane.

### 5. DISCUSSION

In general, and as anticipated by Fig. 3, the SD scores are lower for the  $HRTF_{ann}$  for all the subjects S5 and all the positions analysed. This is because the ANNs are better able to generalize from the examples learned during their training.

Due to the fact that the SD integrates the errors in a specific frequency range, and the results obtained for group S5 differ significantly from subject to subject, it is necessary to analyse the goodness of fit in further detail. Table 2 shows the average and standard deviation (STD) of SD scores of the group S5 for all positions of the median plane for both methods. The subjects with the lowest and the highest average SD (average error), subject 020 and subject 018 respectively, were studied for four selected elevation angles:  $-45^\circ$ ,  $0^\circ$ ,  $+45^\circ$ ,  $+90^\circ$ , i.e., in the frontal hemisphere, below and above the interaural axis.

Figure 4 shows the  $HRTF_{ori}$ , the  $HRTF_{mlr}$ , and the  $HRTF_{ann}$  for subjects 020 and 018 for the selected positions and left ear. As can be seen, the differences in levels of fitting accuracy between the subject’s position and personalization methods are considerable in almost every position and for both subjects. However, the question is whether these differences are significant from the perceptual point of view.

**Table 2.** Average and standard deviation (STD) of SD scores of the group S5 for all positions of median plane and both methods (all values are in dB).

Subject	Linear regression		ANNs	
	Average	STD	Average	STD
027	3.46	1.50	3.13	1.06
020	3.35	1.45	3.08	1.52
018	5.56	1.81	4.69	1.33
010	4.24	1.39	3.76	1.20
003	4.71	1.30	4.01	1.13

Abundant literature has proven the perceptual importance and relevance of the HRTFs spectral profiles in the median plane. The variations of the resonance and notches’ central frequencies with the elevation for frequencies higher than 4 kHz are the important cues the pinna gives to localize a sound source in the median plane.<sup>1,24,25,31,32</sup>

Iida et al.<sup>31</sup> aims at investigating which peaks and notches in the HRTFs spectrum, above 4 kHz, play a predominant role. First of all, the change in the characteristic parameters of the first notch (called N1) and the second one (called N2), such as the central frequencies and levels, are important cues in the perception of elevation. These findings agree with those reported by Hebrank and Wright.<sup>25</sup> Yet, a single peak or a single notch does not provide enough information so as to localize the elevation of a sound source emitting broadband noise.<sup>31</sup> The first peak (called P1), between 4 and 5 kHz, cannot collaborate with the perception of elevation by itself. However, it seems that the auditory system might use P1 as reference information to analyse N1 and N2 notches.

Peak P1 and notches N1 and N2 for the group S5 will be analysed below.

### 5.1. Characteristic Resonance

All graphs of Fig. 4 have the good fit in the low frequencies below 4 kHz in common. The reason for this is that the first six PCs only include the behavior of the HRTFs in high frequencies (Fig. 2) and, consequently, the HRTFs variations in low frequencies (where torso and shoulder influence is relevant) cannot be seen.<sup>16,18,33</sup>

Figure 4 clearly reproduces the central frequency of a wide resonance in about 4 kHz (P1). The central frequency differences for the characteristic resonance between the  $HRTF_{ori}$ , and the HRTFs estimated for both methods ( $HRTF_{mlr}$  and  $HRTF_{ann}$ ) are in the order of the thresholds determined by Moore et al.<sup>34</sup> ( $< 5.6\%$ ). Shaw<sup>24</sup> called it mode 1 and described it as independent of the direction of incidence (omni-directional). Additionally, the sound pressure differences are lower to the thresholds established also by Moore et al., who concluded that the threshold to discriminate a change of sound pressure level from a peak overlapped to broadband noise is 2–3 dB. Therefore, for most positions, the reproduction of P1 is acceptable for both methods and subjects.

### 5.2. Characteristic Notches

The notches, between 5 and 15 kHz, are produced by the interaction of a direct wave, which reaches the entrance of the ear canal and the reflections caused in different regions of the pinna. They are another important spectral characteristic in the median plane.

The first notch (N1) is the result of reflections produced in the posterior wall of the concha.<sup>25,26,31,32</sup> The central frequency varies systematically with the position between  $-45^\circ$

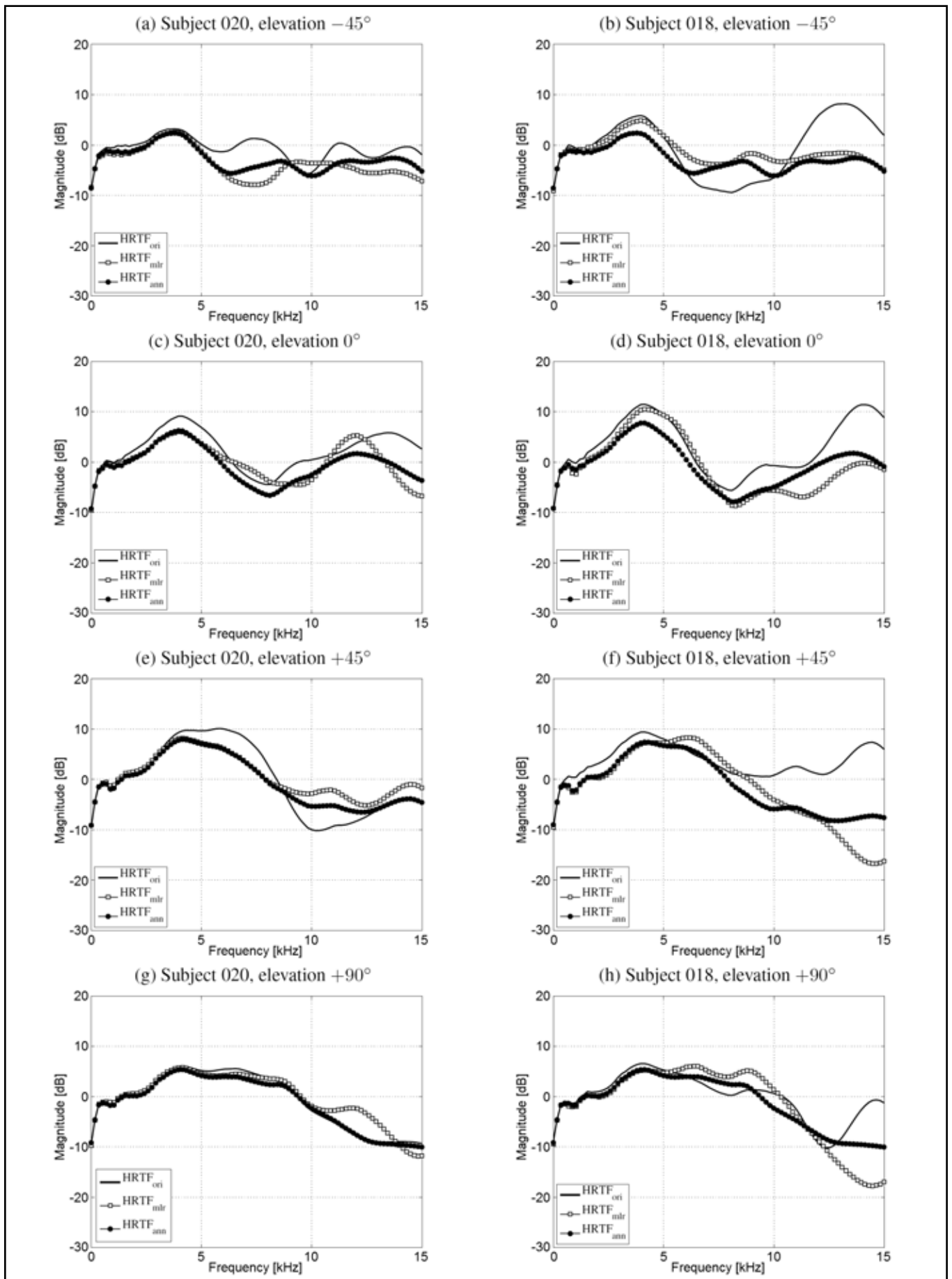


Figure 4. HRTF<sub>ori</sub>, HRTF<sub>mlr</sub> and HRTF<sub>ann</sub> for subjects 020 (left column) and 018 (right column).

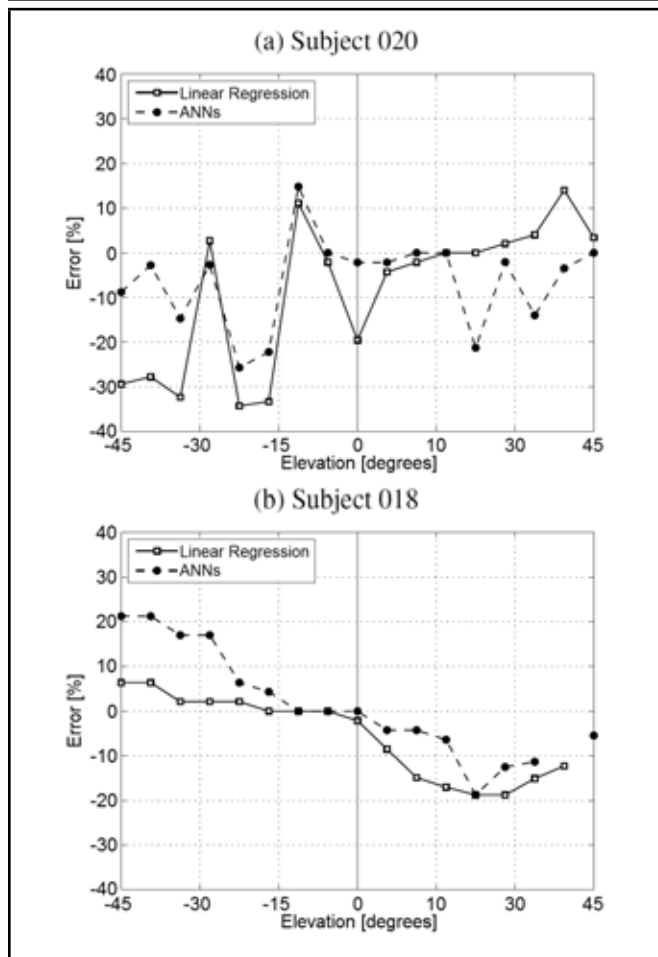


Figure 5. Errors of central frequencies of N1 notches for subjects 020 and 018.

and +45°. The second notch (N2) appears between -45° and 0°, whose frequency is almost constant and may be caused by the presence of the crus helias and the fossa in the concha.<sup>26,33</sup>

The error of central frequencies and of sound pressure values of N1 notches for both subjects between -45° and +45° was measured. The error of central frequencies was calculated as a percentage of center frequency of the HRTF<sub>ori</sub>. Negative errors imply that the central frequency of notches of the personalized HRTFs shifted to the high frequencies, while positive errors mean the opposite.

The results obtained for the left ear of both subjects (Fig. 5) are completely dissimilar. For subject 020, the errors for N1 notches are negative for most positions and both methods. This would cause a systematic shift in the perception of the position of a static sound source, provided that the difference of the N1 central frequencies can be discriminated. Moore et al.<sup>34</sup> have investigated the detection and discrimination of a single spectral notch overlapped to a broadband noise, both for the central frequency and for the sound pressure value. They established that differences higher than 8.3% can be discriminated. There are positions in Fig. 5 in which this value is largely exceeded for both personalization methods. The perceptual consequences for subject 018 might still be more serious. In the -45° to 0° range, the error is positive for both methods, and the fit is better for the linear method (< 8.3%). However, in the proximity of 0° and up to +45° the error changes sign and increases its absolute value. This might produce severe errors when judging the position of a static source and a change of

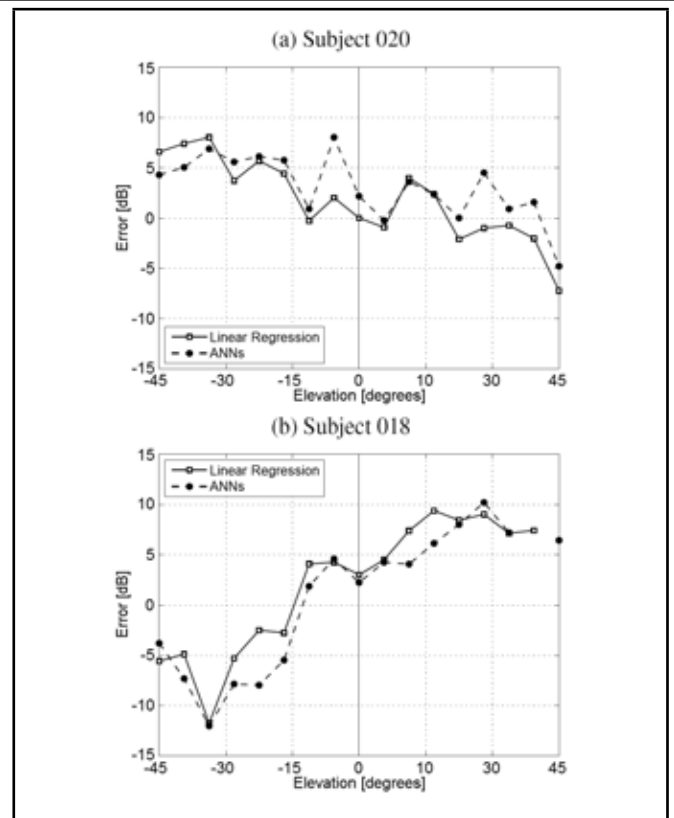


Figure 6. Errors of sound pressure levels of N1 notches for subjects 020 and 018.

direction at 0° for a dynamic source that moves from bottom to top and vice versa.

Figure 6 shows the errors of sound pressure values in the notches for the left ear (difference between the HRTF<sub>ori</sub> and the HRTF<sub>mlr</sub> and HRTF<sub>ann</sub> levels in the N1 notch frequencies). Both subjects exhibit a systematic error variation with the position, but in different directions. In some positions, the error changes sign and, for most positions, it is higher than the just-noticeable difference (jnd) measured by Moore et al. (2–3 dB).<sup>34</sup> N2 could not be evaluated because this notch is not present in the personalized HRTFs, for most analysed positions.

Despite the fact that the SD scores of ANNs are lower than those of the multiple linear regression and are in the range validated by other authors, it has been proven that the errors obtained from analysing the notches' central frequencies and levels could be discriminated theoretically.

On the other hand, some authors propose methods to correct the notches' central frequencies,<sup>5,35</sup> which consist of correlating them with pinna measurements, and choose those with the highest values. Then the central frequencies are estimated by multiple linear regression. The purpose of this is to find the closest local minimum of the personalized HRTF to the notches' central frequencies considered. Finally, the notches' central frequencies in the personalized HRTF are modified by using the estimated ones from the subject's pinna parameters.

Nowadays, the trend is to use different methods to generate the resonances and the notches. It is assumed that notches are originated from destructive interference between the direct and reflected waves produced in specific areas of the pinna. In 2010, Spagnol et al.<sup>36</sup> determined the possible reflection paths of the pinna. Thus, they determined the time delays be-

tween the direct and reflected wave at the entrance of the ear canal, which depend on elevation. From these results, it was possible to design comb filters to generate the notches of personalized HRTFs. In a recent article,<sup>37</sup> the same authors, implemented a model for real-time HRTF synthesis that extracts the pinna contours from a picture and, by means of ray-tracing, direction-dependent distances (and time delays) are estimated. Finally, based on the anthropometry-based pinna model,<sup>38</sup> they proposed a model, extended to a wider region of the frontal hemisphere, which includes multiple reflection paths using a multi-notch filter suitable for anthropometric parameterization.

## 6. CONCLUSIONS

In order to analyse the validity of SD as a measure of the quality of the HRTF personalization in the median plane, a procedure that performs PCA to the CIPIC HRIR database was used. The weights of PCA for a group of 30 subjects were estimated by two methods: multiple linear and non-linear (ANNs) regressions, using seven anthropometric measurements selected. The personalized HRTFs for this group with six PCs resulting from both methods were compared with the reconstructed HRTFs of five subjects outside the previous group.

From this study, it was concluded that the ANNs are better than multiple linear regression for HRTF personalization in the median plane, taking into account the SD scores. However, from the objective analysis carried out on two subjects (lowest and highest SD mean), it is impossible to figure out which method is better. The error values of the central frequency and level of the characteristic peak and notches in the median plane, between the HRTFs measured and those estimated, could be discriminable and might produce localization errors. Neither conclusions could be inferred from the fact that the personalized HRTFs of the subject with the lowest SD mean fits better than those of the subject with the highest SD mean. Thus, the SD, that is, the euclidean distance between both spectra integrated in a specific frequency range, is not a reliable indicator to assess the goodness of fit in the median plane, from the localization point of view, where the spectral notches are highly significant. However, the potential usefulness of the SD should be noted as a measure to assess differences in sound timbre between the measured and the personalized HRTF, for which it is necessary to perform subjective studies.

The construction of personalized HRTFs requires further knowledge of which anthropometric parameters are involved in the generation of the spectral cues. It is not clear yet which measurements of the anatomical features are the most dominant in the HRTFs characteristics, nor the selection method. Using unidimensional measurements from the pinna cavities could be appropriate to estimate some of the characteristic resonances of the external ear.<sup>22,24</sup> However, it is crucial to have the anatomical form of the pinna to precisely determine the central frequencies of characteristic notches.<sup>25,26,28</sup>

In our laboratory, the subject's own HRTFs are measured, and its anatomical features are identified using three-dimensional image processing techniques. These results will enable subjective evaluation in future works.

## ACKNOWLEDGMENTS

This research was supported by the National Technological University (UTN) and the National Scientific and Technical Research Council (CONICET) from Argentina. The authors thanks Oscar Bustos and Mariano Araneda for contributions and suggestions to this paper. The authors also thank V. Ralph Algazi for allowing the reproduction of the figures of CIPIC anthropometric measurements.

## REFERENCES

- <sup>1</sup> Blauert, J. *Spatial hearing: the psychophysics of human sound localization*, MIT Press, Cambridge, MA, USA, (1997).
- <sup>2</sup> Kleiner, M., Dalenbäck, B. I., and Svensson, P. Auralization—an overview, *Journal of the Audio Engineering Society*, **41** (11), 861–875, (1993).
- <sup>3</sup> Wenzel, E. M., Arruda, M., Kistler, D. J., and Wightman, F. L. Localization using nonindividualized head-related transfer functions, *Journal of the Acoustical Society of America*, **94** (1), 111–123, (1993).
- <sup>4</sup> Xu, S., Li, Z., and Salvendy, G. Individualization of head-related transfer function for three-dimensional virtual auditory display: A review, *Virtual Reality*, R. Shumaker, Ed., Springer, Berlin, Heidelberg, (2007), 397–407.
- <sup>5</sup> Rodríguez, S. G. and Ramírez, M. A. Linear relationships between spectral characteristics and anthropometry of the external ear, *Proc. 11th Meeting of the International Conference on Auditory Display*, 336–339, Limerick, Ireland, (2005).
- <sup>6</sup> Hu, H., Zhou, L., Zhang, J., Ma, H., and Wu, Z. Head related transfer function personalization based on multiple regression analysis, *Proc. 2006 International Conference on Computational Intelligence and Security (CIS)*, **2**, 1829–1832, Guangzhou, China, (2006).
- <sup>7</sup> Hwang, S. and Park, Y. HRIR customization in the median plane via principal components analysis, *Proc. AES 31st International Conference: New Directions in High Resolution Audio*, London, UK, (2007).
- <sup>8</sup> Hwang, S., Park, Y., and Park, Y. S. Modeling and customization of head-related impulse responses based on general basis functions in time domain, *Acta Acustica united with Acustica*, **94** (6), 965–980, (2008).
- <sup>9</sup> Xu, S., Li, Z., and Salvendy, G. Identification of anthropometric measurements for individualization of head-related transfer functions, *Acta Acustica united with Acustica*, **95** (1), 168–177, (2009).
- <sup>10</sup> Hu, H., Zhou, L., Ma, H., and Wu, Z. HRTF personalization based on artificial neural network in individual virtual auditory space, *Applied Acoustics*, **69** (2), 163–172, (2008).
- <sup>11</sup> Huang, Q. H. and Fang, Y. Modeling personalized head-related impulse response using support vector regression, *Journal of Shanghai University (English Edition)*, **13** (6), 428–432, (2009).

- <sup>12</sup> Nishino, T., Kajita, S., Takeda, K., and Itakura, F. Interpolating head related transfer functions in the median plane, *Proc. 1999 IEEE Workshop on Applications of Signal Processing to Audio and Acoustics*, 167–170, New Paltz, NY, USA, (1999).
- <sup>13</sup> Avendano, C., Duda, R. O., and Algazi, V. R. Modeling the contralateral HRTF, *Proc. AES 16th International Conference on Spatial Sound Reproduction*, Rovaniemi, Finland, (1999).
- <sup>14</sup> Silzle, A. Selection and tuning of HRTFs, *Proc. AES 112th Convention*, 1–14, Munich, Germany, (2002).
- <sup>15</sup> Mahé, G., Gilloire, A., and Gros, L. Correction of the voice timbre distortions in telephone networks: method and evaluation, *Speech Communication*, **43** (3), 241–266, (2004).
- <sup>16</sup> Algazi, V. R., Duda, R. O., Thompson, D. M., and Avendano, C. The CIPIC HRTF database, *Proc. 2001 IEEE Workshop on Applications of Signal Processing to Audio and Electroacoustics*, 99–102, New Paltz, NY, USA, (2001).
- <sup>17</sup> The CIPIC HRTF Database files, Retrieved from <http://interface.cipic.ucdavis.edu/sound/hrtf.html> (Accessed February 25, 2014).
- <sup>18</sup> Kistler, D. J. and Wightman, F. L. A model of head-related transfer functions based on principal components analysis and minimum-phase reconstruction, *Journal of the Acoustical Society of America*, **91** (3), 1637–1647, (1992).
- <sup>19</sup> Shlens, J. A tutorial on principal component analysis, Technical report, Systems Neurobiology Laboratory, University of California at San Diego, (2005).
- <sup>20</sup> Ramos, O. A., Calvo, G., and Tommasini, F. C. Modelo acústico de cabeza y torso mediante análisis de componentes principales, *Mecánica Computacional*, **XXVI**, 46–58, (2007).
- <sup>21</sup> Ramos, O. A. and Tommasini, F. C. Simplificación de las funciones de transferencia de cabeza mediante análisis de componentes principales, *Mecánica Computacional*, **XXVII**, 431–442, (2008).
- <sup>22</sup> Shaw, E. A. G. and Teranishi, R. Sound pressure generated in an external-ear replica and real human ears by a nearby point source, *Journal of the Acoustical Society of America*, **44** (1), 240–249, (1968).
- <sup>23</sup> Teranishi, R. and Shaw, E. A. G. External-ear acoustic models with simple geometry, *Journal of the Acoustical Society of America*, **44** (1), 257–263, (1968).
- <sup>24</sup> Shaw, E. A. G. Acoustical features of the human external ear, *Binaural and Spatial Hearing in Real and Virtual Environments*, R.H. Gilkey and T.R. Anderson, Eds., Lawrence Erlbaum Associates, Mahwah, NJ, USA, (1997), 25–47.
- <sup>25</sup> Hebrank, J. and Wright, D. Spectral cues used in the localization of sound sources on the median plane, *Journal of the Acoustical Society of America*, **56** (6), 1829–1834, (1974).
- <sup>26</sup> Lopez-Poveda, E. A. and Meddis, R. A physical model of sound diffraction and reflections in the human concha, *Journal of the Acoustical Society of America*, **100** (5), 3248–3259, (1996).
- <sup>27</sup> Fels, J. and Vorländer, M. Anthropometric parameters influencing head-related transfer functions, *Acta Acustica united with Acustica*, **95**, 331–342, (2009).
- <sup>28</sup> Raykar, V. C., Duraiswami, R., and Yegnanarayana, B. Extracting the frequencies of the pinna spectral notches in measured head related impulse responses, *Journal of the Acoustical Society of America*, **118** (1), 364–374, (2005).
- <sup>29</sup> Wythoff, B. J. Backpropagation neural networks: A tutorial, *Chemometrics and Intelligent Laboratory Systems*, **18** (2), 115–155, (1993).
- <sup>30</sup> Hecht-Nielsen, R. Kolmogorov’s mapping neural network existence theorem. *Proc. IEEE First International Conference on Neural Networks*, **3**, 11–14, San Diego, CA, USA, (1987).
- <sup>31</sup> Iida, K., Itoh, M., Itagaki, A., and Morimoto, M. Median plane localization using a parametric model of the head-related transfer function based on spectral cues, *Applied Acoustics*, **68** (8), 835–850, (2007).
- <sup>32</sup> Asano, F., Suzuki, Y., and Sone, T. Role of spectral cues in median plane localization, *Journal of the Acoustical Society of America*, **88** (1), 159–168, (1990).
- <sup>33</sup> Ramos, O. A., Tommasini, F. C., and Araneda, M. Contribución de la cabeza, el torso y el oído externo en las funciones de transferencia relativas a la cabeza, *Proc. 2do Congreso Internacional de Acústica UNTREF 2010*, Buenos Aires, Argentina, (2010).
- <sup>34</sup> Moore, B. C. J., Oldfield, S. R., and Dooley, G. J. Detection and discrimination of spectral peaks and notches at 1 and 8 kHz, *Journal of the Acoustical Society of America*, **85** (2), 820–836, (1989).
- <sup>35</sup> Hu, H., Chen, L., and Wu, Z. Y. The estimation of personalized HRTFs in individual VAS, *Proc. Fourth International Conference on Natural Computation ICNC ’08*, **6**, 203–207, Jinan, China, (2008).
- <sup>36</sup> Spagnol, S., Geronazzo, M., and Avanzini, F. Fitting pinna-related transfer functions to anthropometry for binaural sound rendering, *Proc. 2010 IEEE International Workshop on Multimedia Signal Processing (MMSP)*, 194–199, Saint Malo, France, (2010).
- <sup>37</sup> Spagnol, S., Geronazzo, M., and Avanzini, F. On the relation between pinna reflection patterns and head-related transfer function features, *IEEE Transactions on Audio, Speech, and Language Processing*, **21** (3), 508–519, (2013).
- <sup>38</sup> Algazi, V. R., Duda, R. O., and Satarzadeh, P. Physical and filter pinna models based on anthropometry, *Proc. AES 122th Convention*, Vienna, Austria, (2007).

# Stability of a Nonlinear Quarter-Car System with Multiple Time-Delays

Raghavendra D. Naik and Pravin M. Singru

Department of Mechanical Engineering, Birla Institute of Technology and Science, Pilani, K. K. Birla Goa Campus, Zuarinagar, Goa, India 403726

(Received 20 March 2013; accepted 4 March 2015)

This paper examines the dynamical behaviour of a nonlinear oscillator which models a two-degree-of-freedom quarter-car system forced by the road profile. The influence of two time delays in the system, which is generally due to the inherent dynamics of the actuator, is studied. The asymptotic and technical stability domain is obtained by using Bogusz's stability criterion for a two-degree-of-freedom system. The results obtained from Lyapunov's and Bogusz's stability criteria are compared. The numerical results obtained are found to be in good agreement with the analytical predictions.

## 1. INTRODUCTION

Li et al. investigated a possible chaotic motion in a nonlinear vehicle suspension system, which is subject to a multi-frequency excitation from a road surface.<sup>5</sup> Litak et al. investigated global homoclinic bifurcation and the transition to chaos in the case of a quarter-car model excited kinematically by a road surface profile.<sup>6</sup> Siewe Siewe investigated resonance, stability, and the chaotic motion of a quarter-car model excited by a road surface profile.<sup>11</sup> All controllers exhibit a certain time-delay during operation. Many researchers have studied the behaviour of delayed differential equations. Zhang et al. studied the stability of the delayed differential equations.<sup>13</sup> Wirkus and Rand investigated the dynamics of two van der Pol oscillators with delay velocity coupling with special attention to the bifurcation accompanying the change in number and the stability of the solutions.<sup>9</sup> Gohary studied the vibration suppression of a dynamical system to multi-parametric excitations via a time-delay absorber.<sup>3</sup> Naik & Singru studied the stability of a single-degree-of-freedom system.<sup>8</sup>

The dynamics of a quarter-car model with nonlinear suspension characteristics was studied by Li et al. and Shen et al.<sup>4,10</sup> Recent efforts by Borowiec et al. have been focused on the excitation of the automobile by a road surface profile with harmful noise components.<sup>2</sup> Hysteretic nonlinear suspension was studied by Yang et al.<sup>12</sup>

This paper deals with the dynamics of a quarter-car model with an active vehicle suspension system. The influence of delay in the system, which is generally due to the inherent dynamics of the actuator, is studied. The time delay systems are usually of infinite dimension; an attempt is made to reduce them to a finite dimension since the operating time delays in the system under consideration are small (Processing Time & Actuator Delays). The technical stability domain is obtained by using Bogusz's stability criterion on the finite time domain. The asymptotic stability is derived for unequal time delays.

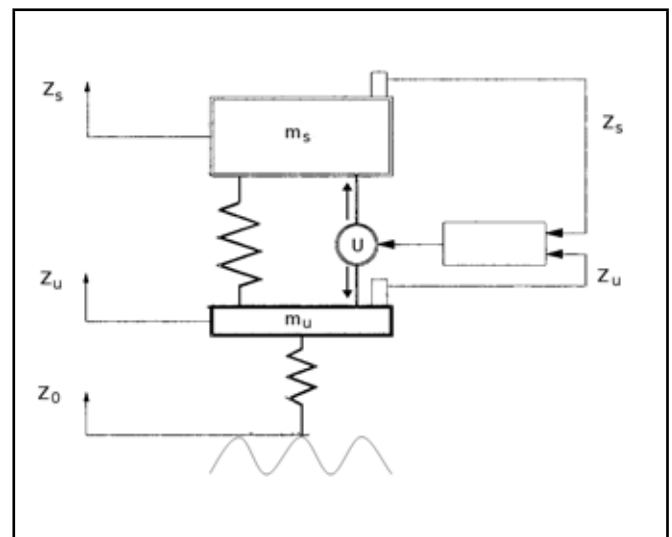


Figure 1. The quarter-car model active control.

The stability of the two models are investigated, and the results are compared. The results are validated by numerical simulations.

## 2. TWO-DEGREE-OF-FREEDOM QUARTER-CAR SYSTEM

Figure 1 shows the closed-loop active control for the vehicle system. This system represents an active vehicle suspension system with non-linearity in the dampers; the parameters considered are similar to that of the single-degree-of-freedom system considered in the previous section.

The equation of motion is assumed to have the following form:

$$\begin{aligned} m_u \ddot{z}_u - k(z_s - z_u) - k_t(z_0 - z_u) + U(t) &= 0; \\ m_s \ddot{z}_s + k(z_s - z_u) - U(t) &= 0; \end{aligned} \quad (1)$$

where  $U(t)$  is the active control force

$$U(t) = -C_2(\dot{Z}_s - \dot{Z}_u)^3 + K_{Au}Z_u(t - \tau_1) + K_{As}Z_s(t - \tau_2) + \dots + C_{Au}\dot{Z}_u(t - \tau_1) + C_{As}\dot{Z}_s(t - \tau_2) - C_1(\dot{Z}_s - \dot{Z}_u); \quad (2)$$

$\omega_u^2 = \left(\frac{k+k_t}{m_u}\right)$ ;  $\omega_s^2 = \left(\frac{k}{m_s}\right)$ ;  $K_1 = \left(\frac{k}{m_u}\right)$ ;  $C_1 = \left(\frac{c_1}{m_u}\right)$ ;  $C_2 = \left(\frac{c_2}{m_u}\right)$ ;  $K_{1u} = \left(\frac{K_{A1}}{m_u}\right)$ ;  $K_{2u} = \left(\frac{K_{A2}}{m_u}\right)$ ;  $C_{1u} = \left(\frac{C_{A1}}{m_u}\right)$ ;  $C_{2u} = \left(\frac{C_{A2}}{m_u}\right)$ ;  $C_3 = \left(\frac{c_1}{m_s}\right)$ ;  $C_4 = \left(\frac{c_2}{m_s}\right)$ ;  $K_{1s} = \left(\frac{K_{A1}}{m_s}\right)$ ;  $K_{2s} = \left(\frac{K_{A2}}{m_s}\right)$ ; and  $C_{1s} = \left(\frac{C_{A1}}{m_s}\right)$ ;  $C_{2s} = \left(\frac{C_{A2}}{m_s}\right)$ ; where  $\omega_u$  = unsprung mass natural frequency,  $\omega_s$  = sprung mass natural frequency,  $K_{Au}$  are semi-active stiffness for unsprung mass,  $K_{As}$  are semi-active stiffness for sprung mass  $C_{Au}$  semi-active damping for unsprung mass,  $C_{As}$  semi-active damping for sprung mass,  $\tau_u, \tau_s$  are the time-delays associated with unsprung and sprung mass, and the parameters are as follows:<sup>1</sup>  $m_s = 200$  kg;  $m_u = 40$  kg;  $k = 9000$  Nm<sup>-1</sup>;  $k_t = 160,000$  Nm<sup>-1</sup>;  $k_2 = -300,000$  Nm<sup>-3</sup>;  $c_1 = 10,000$  Nsm<sup>-1</sup>;  $c_2 = -25,000$  Ns<sup>3</sup>m<sup>-3</sup>;  $C_{As} = 1000$  Nsm<sup>-1</sup>;  $C_{Au} = -10,000$  Nsm<sup>-1</sup>;  $K_{As} = 250000$  Nm<sup>-1</sup>;  $K_{Au} = 50000$  Nm<sup>-1</sup>.

### 3. LYAPUNOV STABILITY FOR TWO-DEGREE-OF-FREEDOM-SYSTEM

The asymptotic stability as  $t \rightarrow \infty$  is studied for the two-degree-of-freedom system, and the results are compared with the technical stability criterion. The time-delay systems are usually infinite dimensional. An attempt is made to reduce them to a finite dimension since the operating time delays in the system under consideration are small (Processing Time & Actuator Delays).

Expanding the function  $U(t)$  into Taylor's series including only the first term of the function  $U(t)$ :

$$U(t) = -C_2(\dot{Z}_s - \dot{Z}_u)^3 + K_{Au}Z_u(t) + \tau_u K_{Au}\dot{Z}_u(t) + K_{As}Z_s(t) + \tau_s K_{As}\dot{Z}_s(t) + \dots + C_{Au}\dot{Z}_u(t) + \tau_u C_{Au}\ddot{Z}_u(t) + C_{As}\dot{Z}_s(t) + \tau_s C_{As}\ddot{Z}_s(t) - C_1(\dot{Z}_s - \dot{Z}_u). \quad (3)$$

Since the non-homogeneous equation's stability is preserved when the stability of the homogeneous equations hold, the stability of the homogeneous equations are investigated, and we neglect the third power. Substituting Eq. (3) into Eq. (1) and considering only linear terms we obtain:

$$(1 + \tau_u C_{1u})\ddot{Z}_u + (K_{1u} + \omega_u^2)Z_u(t) + (C_1 + C_{1u} + \tau_u K_{1u})\dot{Z}_u(t) + (K_{2u} - K_1)Z_s(t) + (\tau_s K_{2u} - C_1 + C_{2u})\dot{Z}_s(t) + \tau_s C_{2u}\ddot{Z}_s(t) = 0; \quad (4)$$

$$(1 - \tau_s C_{2s})\ddot{Z}_s + (\omega_s^2 - K_{2s})Z_s + (C_3 - \tau_s K_{2s} - C_{2s})\dot{Z}_s(t) - (C_3 + \tau_s K_{1s} + C_{1s})\dot{Z}_u(t) + (K_{1s} - \omega_s^2)Z_u - \tau_u C_{1s}\ddot{Z}_u(t) = 0; \quad (5)$$

$$\ddot{Z}_u + \alpha_1 Z_u(t) + \alpha_2 \dot{Z}_u(t) + \alpha_3 Z_s(t) + \alpha_4 \dot{Z}_s(t) + \alpha_5 \ddot{Z}_s(t) = 0; \quad (6)$$

$$\ddot{Z}_s + \beta_1 Z_s + \beta_2 \dot{Z}_s(t) + \beta_3 \dot{Z}_u(t) + \beta_4 Z_u + \beta_5 \ddot{Z}_u = 0; \quad (7)$$

where  $\alpha_1 = \frac{(K_{1u} + \omega_u^2)}{(1 + \tau_u C_{1u})}$ ,  $\alpha_2 = \frac{(C_1 + C_{1u} + \tau_u K_{1u})}{(1 + \tau_u C_{1u})}$ ,  $\alpha_3 = \frac{(K_{2u} - K_1)}{(1 + \tau_u C_{1u})}$ ,  $\alpha_4 = \frac{(\tau_s K_{2u} - C_1 + C_{2u})}{(1 + \tau_u C_{1u})}$  and  $\alpha_5 = \frac{\tau_u C_{2u}}{(1 + \tau_u C_{1u})}$  and  $\beta_1 = \frac{(\omega_s^2 - K_{2s})}{(1 - \tau_s C_{2s})}$ ,  $\beta_2 = \frac{(C_3 - \tau_s K_{2s} - C_{2s})}{(1 - \tau_s C_{2s})}$ ,  $\beta_3 = \frac{(K_{1s} - \omega_s^2)}{(1 - \tau_s C_{2s})}$ ,  $\beta_4 = \frac{(C_3 + \tau_s K_{1s} + C_{1s})}{(1 - \tau_s C_{2s})}$  and  $\beta_5 = \frac{\tau_s C_{1s}}{(1 - \tau_s C_{2s})}$ . Substituting Eq. (6) into Eq. (7) we obtain:

$$\ddot{Z}_u = a_1 Z_u + a_2 Z_s + a_3 \dot{Z}_u + a_4 \dot{Z}_s. \quad (8)$$

Substituting Eq. (7) into Eq. (6) we obtain:

$$\ddot{Z}_s = b_1 Z_u + b_2 Z_s + b_3 \dot{Z}_u + b_4 \dot{Z}_s; \quad (9)$$

where  $a_1 = -\left[\frac{\alpha_1 - \alpha_5 \beta_4}{1 + \alpha_5 \beta_5}\right]$ ,  $a_2 = -\left[\frac{\alpha_2 + \alpha_5 \beta_3}{1 + \alpha_5 \beta_5}\right]$ ,  $a_3 = -\left[\frac{\alpha_3 - \alpha_5 \beta_1}{1 + \alpha_5 \beta_5}\right]$ ,  $a_4 = -\left[\frac{\alpha_4 - \alpha_5 \beta_2}{1 + \alpha_5 \beta_5}\right]$  and  $b_1 = -\left[\frac{\beta_4 + \beta_5 \alpha_1}{1 + \alpha_5 \beta_5}\right]$ ,  $b_2 = -\left[\frac{\beta_1 + \beta_5 \alpha_3}{1 + \alpha_5 \beta_5}\right]$ ,  $b_3 = -\left[\frac{\beta_5 \alpha_2 - \beta_3}{1 + \alpha_5 \beta_5}\right]$ ,  $b_4 = -\left[\frac{\beta_2 + \beta_5 \alpha_4}{1 + \alpha_5 \beta_5}\right]$ . In the state space form

$$\left. \begin{aligned} \dot{x}_1 &= x_3 \\ \dot{x}_2 &= x_4 \\ \dot{x}_3 &= a_1 x_1 + a_2 x_2 + a_3 x_3 + a_4 x_4 \\ \dot{x}_4 &= b_1 x_1 + b_2 x_2 + b_3 x_3 + b_4 x_4 \end{aligned} \right\} \quad (10)$$

where  $x_1 = Z_u$ ,  $x_2 = \dot{Z}_u$ ,  $x_3 = Z_s$  and  $x_4 = \dot{Z}_s$ , and the characteristic determinant associated with the Eq. (10) has the form

$$W = \begin{vmatrix} -\lambda & 0 & 1 & 0 \\ 0 & -\lambda & 0 & 1 \\ a_1 & a_2 & a_3 - \lambda & a_4 \\ b_1 & b_2 & b_3 & b_4 - \lambda \end{vmatrix}.$$

The determinant takes the form

$$W = \lambda^4 - (a_3 + b_4)\lambda^3 - a_1 \lambda^2 + (b_2 + a_1 b_4 - b_1 a_4)\lambda + a_2 b_3 - b_2 a_3 + a_1 b_2 - b_1 a_2. \quad (11)$$

The following characteristic equation is obtained:

$$\lambda^4 + A_3 \lambda^3 + A_2 \lambda^2 + A_1 \lambda + A_0 = 0,$$

where

$$A_3 = -(a_3 + b_4), A_2 = -a_1,$$

$$A_1 = (b_2 + a_1 b_4 - b_1 a_4)$$

and  $A_0 = a_2 b_3 - b_2 a_3 + a_1 b_2 - b_1 a_2$ . The necessary condition for the stability of the system is

$$A_3 > 0, A_2 > 0, A_1 > 0 \text{ and } A_0 > 0. \quad (12)$$

The sufficient conditions of the system require the positiveness of the determinants

$$D_1 > 0, D_2 > 0, D_3 > 0 \text{ and } D_4 > 0; \quad (13)$$

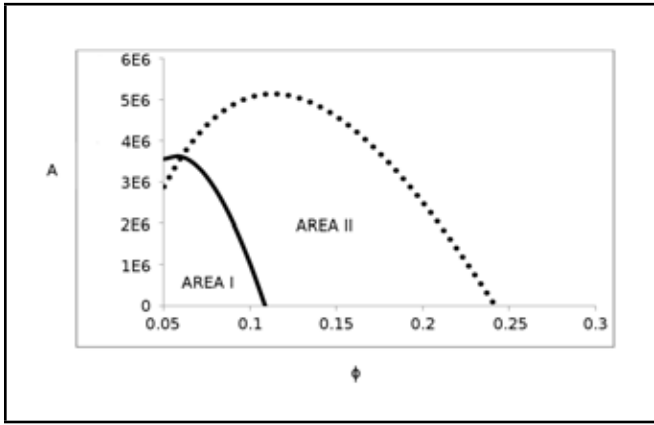


**Figure 2.** The stability region AREA I for  $\tau_u > \tau_s$  and AREA II for  $\tau_s > \tau_u$  (Lyapunovs Stability).

where  $D_1 = A_3, D_2 = \begin{vmatrix} A_3 & 1 \\ A_1 & A_2 \end{vmatrix}$ ,

$$D_3 = \begin{vmatrix} A_3 & 1 & 0 \\ A_1 & A_2 & A_3 \\ 0 & A_0 & A_1 \end{vmatrix} \text{ and } D_4 = \begin{vmatrix} A_3 & 1 & 0 & 0 \\ A_1 & A_2 & A_3 & 1 \\ 0 & A_0 & A_1 & A_2 \\ 0 & 0 & 0 & A_0 \end{vmatrix}.$$

Now consider two cases

(i) The time delay associated with the sprung mass dynamics is greater than that of the unsprung mass dynamics i.e.  $\tau_s > \tau_u$  and

(ii) The time delay associated with the unsprung mass dynamics is greater than that of the sprung mass dynamics i.e.

$$\tau_u > \tau_s,$$

where the delay difference is  $\phi = \tau_s - \tau_u > 0$  for  $\tau_s > \tau_u$  and  $\phi = \tau_s - \tau_u < 0$  for  $\tau_u > \tau_s$ .

The conditions in Eqs. (12) and (13) are plotted by using MATLAB 11 by considering the parameters given in Section 3 above. Figure 2 indicates that the stability regions are the areas below the two curves where A is the amplitude of vibrations. Comparing both of the curves, one can observe that in the case of  $\tau_s > \tau_u$ , the area below the curve (AREA II) is greater than the area for  $\tau_u > \tau_s$  (AREA I). The domain located below the curve, where the control is efficient is greater for  $\tau_s > \tau_u$ . Therefore vibration control is efficient for  $\tau_s > \tau_u$ . It can be easily found from Fig. 2 that for the delay difference  $\phi = \tau_s - \tau_u < 0.24$ , the control is efficient for  $\tau_s > \tau_u$ , and for  $\tau_u > \tau_s$  the control is efficient for  $\phi = \tau_s - \tau_u < 0.11$ .

The nonlinear differential Eq. (1) is numerically simulated to obtain the Poincaré section (plot of velocity v/s displacement) by using the dde23 module of MATLAB with a numerical accuracy of  $10^{-8}$ . Figure 3 indicates the regular motion of the sprung mass for  $\tau_u > \tau_s$  and  $\phi = 0.02$ . Figure 4 and Figure 5 indicate the periodic motion of the sprung mass and the unsprung mass for  $\tau_s > \tau_u$  and  $\phi = 0.2$ . Figure 6 indicates the chaotic motion of the sprung mass for  $\tau_s > \tau_u$  and  $\phi = 0.24$ . Figure 7 indicates the chaotic motion of the sprung mass for  $\tau_u > \tau_s$  and  $\phi = 0.15$ , which is much lower compared to  $\tau_s > \tau_u$ . Figure 8 indicates the chaotic motion of the unsprung mass for  $\tau_u > \tau_s$  and  $\phi = 0.15$ .

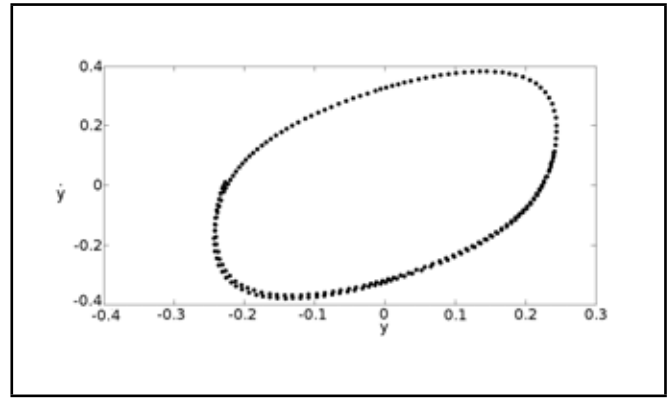


**Figure 3.** Poincaré section of sprung mass for  $\tau_u > \tau_s, \phi = 0.02$  (Period one).

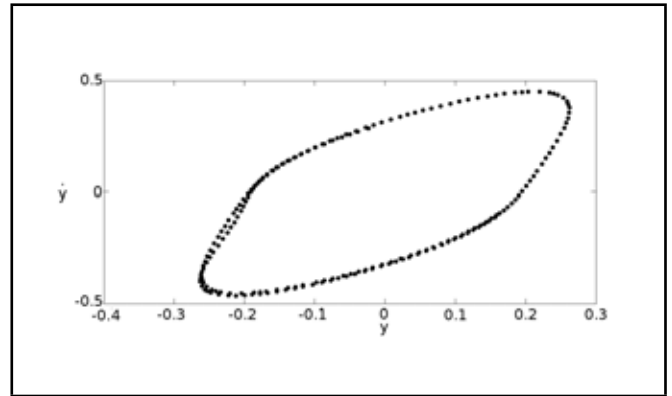


**Figure 4.** Poincaré section of sprung mass for  $\tau_s > \tau_u$  and  $\phi = 0.2$  (Period one).

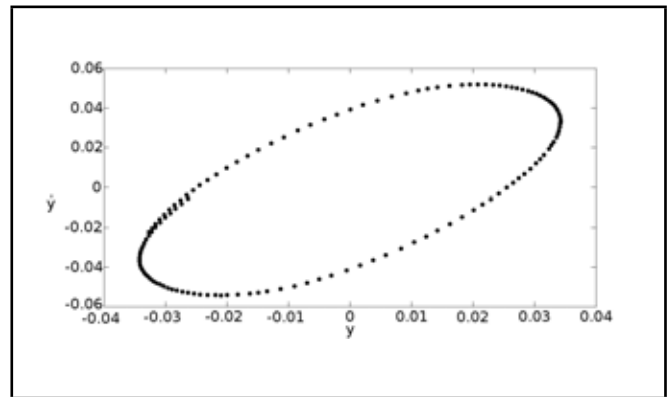


**Figure 5.** Poincaré section of unsprung mass for  $\tau_s > \tau_u$  and  $\phi = 0.2$  (Period one).

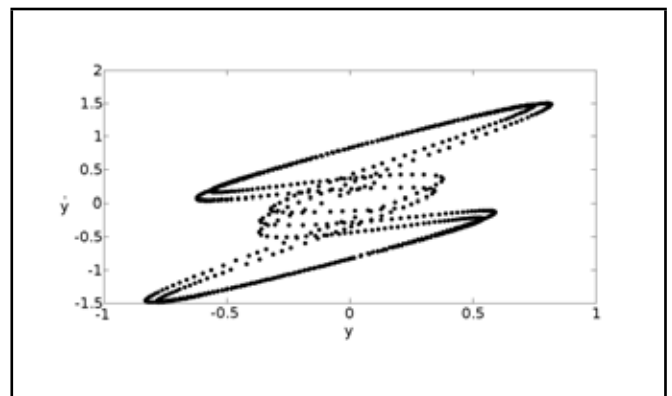


**Figure 6.** Poincaré section of sprung mass for  $\tau_s > \tau_u$  and  $\phi = 0.24$ .



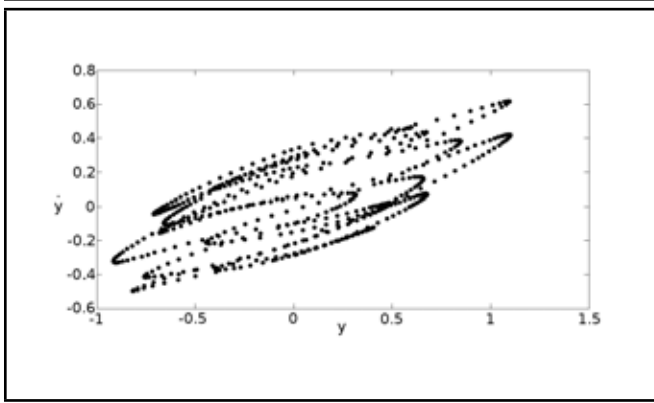


Figure 7. Poincaré section of sprung mass for  $\tau_u > \tau_s, \phi = 0.15$ .

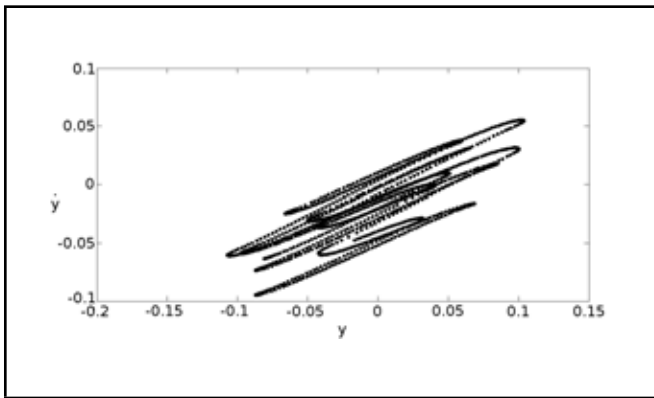


Figure 8. Poincaré section of unsprung mass for  $\tau_u > \tau_s, \phi = 0.15$ .

#### 4. TECHNICAL STABILITY FOR TWO-DEGREE-OF-FREEDOM-SYSTEM

The observation time is often limited and relatively short due to the type of excitation. In such cases, we are interested in the first few seconds of the system's motion.<sup>1</sup> From a practical point of view, the possibility of defining the proximity of the solutions would be advantageous. Let the initial conditions field  $\Gamma$  for  $t = t_0 = 0$  be:

$$\Gamma \equiv \{c_1 x_1^2 + c_2 x_2^2 + c_3 x_3^2 + c_4 x_4^2 < r_0^2\}. \quad (14)$$

The field of acceptable solutions  $\lambda$  for  $t \leq T$ , is assumed as:

$$\lambda \equiv \{c_1 x_1^2 + c_2 x_2^2 + c_3 x_3^2 + c_4 x_4^2 < R_0^2\}; \quad (15)$$

while values  $r_0 < R_0$  so that condition  $\Gamma \in \lambda$  is fulfilled. Bogusz's function will take the form of:

$$V(x_1, x_2, x_3, x_4) = \frac{1}{2} (A x_1^2 + B x_2^2 + C x_3^2 + D x_4^2); \quad (16)$$

where  $A > 0, B > 0, C > 0$ , and  $D > 0$ . If there exists a number  $C_0$  such that

$$C_0 = \inf_{x_i \in \Gamma} [V(x_1, x_2, x_3, x_4)] = \frac{1}{2} (A \cdot r_1^2 + B \cdot r_2^2 + C \cdot r_3^2 + D \cdot r_4^2); \quad (17)$$

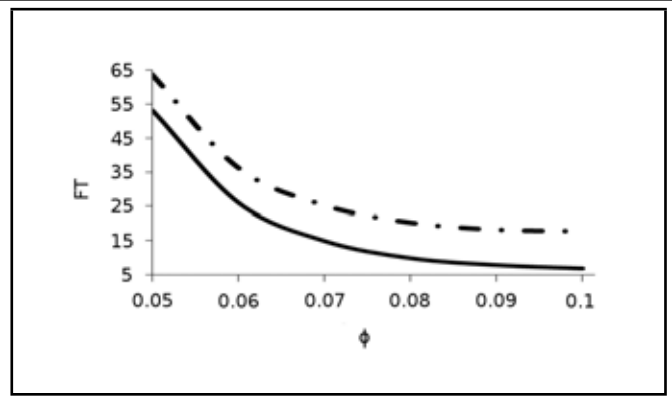


Figure 9. The stability region for  $\tau_u > \tau_s$  is shown by the solid curve, and for  $\tau_s > \tau_u$  it is shown by the dotted curve.

and a number  $C_1$  such that

$$C_1 = \sup_{x_i \in \Gamma} [V(x_1, x_2, x_3, x_4)] = \frac{1}{2} (A \cdot R_1^2 + B \cdot R_2^2 + C \cdot R_3^2 + D \cdot R_4^2); \quad (18)$$

where

$$\frac{\Gamma}{\lambda} \equiv \{r_1^2 < x_1^2 \leq R_1^2, r_2^2 < x_2^2 \leq R_2^2, r_3^2 < x_3^2 \leq R_3^2, r_4^2 < x_4^2 \leq R_4^2\}.$$

The derivative of Bogusz's function along the solutions of the studied system

$$\frac{dV}{dt} = \frac{\partial V}{\partial x_1} \dot{x}_1 + \frac{\partial V}{\partial x_2} \dot{x}_2 + \frac{\partial V}{\partial x_3} \dot{x}_3 + \frac{\partial V}{\partial x_4} \dot{x}_4. \quad (19)$$

Calculating the derivative of Eq. (19) by using Eq. (10) we obtain:

$$\begin{aligned} \frac{dV}{dt} = & C \cdot a_3 \cdot x_3^2 + D \cdot b_4 \cdot x_4^2 + D \cdot b_1 \cdot x_1 \cdot x_4 \\ & + (A + C \cdot a_1) \cdot x_1 \cdot x_3 \\ & + C \cdot a_2 \cdot x_2 \cdot x_3 + (B + D \cdot b_2) \cdot x_2 \cdot x_4 \\ & + (C \cdot a_4 + D \cdot b_3) \cdot x_3 \cdot x_4. \end{aligned} \quad (20)$$

The condition of the system's stability at the stationary state fulfils the following inequality:

$$\sup_{x_i \in \Gamma/\lambda, t_1 \leq t \leq t_1+T} \left\{ \frac{dV}{dt} \right\} < (C_1 - C_0)/T. \quad (21)$$

The technical stability is defined by the factor  $FT$

$$FT = \frac{(C_1 - C_0)}{T} - \frac{dV}{dt}. \quad (22)$$

If  $FT$  is maximum (positive) then the system is stable.

Figure 9 shows two curves;  $\tau_u > \tau_s$  is shown by the solid curve, and  $\tau_s > \tau_u$  is shown by the dotted curve. The curve for  $\tau_s > \tau_u$  occupies a higher position in the plot, indicating better stability conditions. Figure 3 indicates that  $FT$  is lower for  $\tau_u > \tau_s$ . The control is efficient and is greater for  $\tau_s > \tau_u$ .

## 5. RESULTS AND DISCUSSION

Technical stability within definite time in Bogusz's sense was studied for finite time. Then the asymptotic stability was studied by using the Lyapunov method. We have considered two cases (i)  $\tau_s > \tau_u$  and (ii)  $\tau_u > \tau_s$ , where the delay difference is  $\phi = \tau_s - \tau_u < 0$  for  $\tau_s > \tau_u$ .

It was found that the vibration control is efficient for  $\tau_s > \tau_u$  by using the Lyapunov stability criterion. It can be easily found that for the delay difference  $\phi = \tau_s - \tau_u < 0.24$ , the control is efficient for  $\tau_s > \tau_u$ , and for  $\tau_u > \tau_s$  the control is efficient for  $\phi = \tau_s - \tau_u < 0.11$ . Therefore the control domain is better for  $\tau_s > \tau_u$ .

The chaotic and unstable motion of sprung and unsprung mass was found for  $\tau_u > \tau_s$  and  $\phi = \tau_s - \tau_u > 0.11$ . The periodic motion of sprung and unsprung mass was obtained for  $\tau_s > \tau_u$ . The stability region is higher for higher a value of FT in the case of Bogusz's stability criterion. FT is higher in the case of  $\tau_s > \tau_u$  and lower for  $\tau_u > \tau_s$ . The control is efficient and is greater for  $\tau_s > \tau_u$ . The above results are verified by using numerical simulations.

## 6. CONCLUSION

We are interested in the stability of the vehicle for finite time. Vibration control is efficient for  $\tau_s > \tau_u$ . Both Lyapunov's and Bogusz's stability criterion are useful for defining the stability of the given system. The present quarter-car model is able to capture the major dynamics that occur in the vehicle system.

## REFERENCES

- <sup>1</sup> Andrzejewski, R., and Awrejcewicz, J. *Nonlinear Dynamics of Wheeled Vehicle*, Springer, (2005).
- <sup>2</sup> Borowiec, M., Hunicz, J., Sen, A.K., Litak, G., Koszalka, G., and Niewczas, A. Vibrations of a vehicle excited by real road profiles, *Forschung im Ingenieurwesen*, **74**, 99–109, (2010).
- <sup>3</sup> Gohary, H. A., and El-Ganaini, W. A. A. Vibration suppression of a dynamical system to multi-parametric excitations via time-delay absorber, *Applied Mathematical Modeling*, **36**(1), 35–45, (2012).
- <sup>4</sup> Li and Yang, S. Chaos in vehicle suspension system with hysteretic nonlinearity, *Journal of Vibration, Measurement & Diagnosis*, **23**, 86–89, (2003).
- <sup>5</sup> Li, Yang, S., and Guo, W., Investigation on chaotic motion in hysteretic non-linear suspension system with multi-frequency excitations, *Mechanics Research Communications*, **31**, 229–236, (2004).
- <sup>6</sup> Litak, G., Borowiec, M., Friswell, M., and Szabelski K. Chaotic vibration of a quarter-car model excited by the road surface profile, *Communications in Nonlinear Science and Numerical Simulation*, **13**, 1373–1383, (2008).
- <sup>7</sup> Litak, M., Borowiec, M.I., Friswell, W., Przystupa Chaotic response of a quarter-car model excited by the road surface profile with a stochastic component, *Chaos, Solitons & Fractals*, **39**, 2448–2456, (2009).
- <sup>8</sup> Naik and Singru Stability and Hopf bifurcation of a nonlinear oscillator with multiple time-delays, *Chaos, Solitons & Fractals*, **45**, 1387–1396, (2012).
- <sup>9</sup> Wirkus and Rand, R. The dynamics of two coupled van der Pol oscillators with delay coupling, *Nonlinear Dynam.*, **30**, 205–221, (2002).
- <sup>10</sup> Shen, S., Yang, E., Chen and Xing, H. Dynamic analysis of a nonlinear system under semi-active control, *Journal of Vibroengineering*, **18**, 219–222, (2005).
- <sup>11</sup> Siewe Siewe M., Resonance, stability and period-doubling bifurcation of a quarter-car model excited by the road surface profile, *Physics Letters A*, (2010).
- <sup>12</sup> Yang, S., Li, and Guo, W. Chaotic motion in hysteretic non-linear suspension system to random excitation, *Journal of Vibration, Measurement & Diagnosis*, **25**, 22–25, (2005).
- <sup>13</sup> Zhang L., Yang C. Y., Chajes M. J., Cheng A. H. D. Stability of active-tendon structural control with time delay, *Journal of Eng. Mech. Div. ASCE*, **119**, 1017–1024, (1993).

---

---

# Automatic Selection of the WPT Decomposition Level for Condition Monitoring of Rotor Elements Based on the Sensitivity Analysis of the Wavelet Energy

**Cristina Castejón, María Jesús Gómez, Juan Carlos García-Prada, Alberto Junior Ordoñez and Higinio Rubio**

*MAQLAB Group, Mechanical Dept. Universidad Carlos III de Madrid, Av. de la Universidad, 30, 28911, Madrid, Spain*

(Received 25 January 2013; accepted 24 February 2014)

Vibration signals are a widely used technique for machine monitoring and fault diagnostics. However, it is necessary to select a suitable pattern that represents the condition of the machine. Wavelet Packet Transform (WPT) provides a high potential for pattern extraction. Several factors must be selected and taken into account in the wavelet transform application such as the level of decomposition, the suitable mother wavelet, and which frequency bands (obtained from the decomposition process) contain the necessary information for the diagnosis system. The selection of the parameters commented above is a complex task that depends on many factors. Most of the works found in the literature select these factors based on experience, graphical methods, or trial and error methods. In this work, a method based on the relative wavelet energy is developed in order to automatically select the parameter defined by the WPT. The selection allows for the efficient extraction of the most suitable patterns for a later classification and fault detection process. In order to prove the soundness of the method proposed, a Jeffcott rotor model with four crack levels will be developed, and the vibratory signals provided by this model will be used for the monitoring condition.

---

## NOMENCLATURE

WT	Wavelet Transform
FT	Fourier Transform
MRA	Multiresolution Analysis
ANN	Artificial Neural Network
CWT	Continuous Wavelet Transform
DWT	Discrete Wavelet Transform
WPT	Wavelet Packets Transform
Db6	Daubechies 6
RBF	Radial Basis Function Neural Network

## 1. INTRODUCTION

The study of the vibration signal is a main technique in the study and diagnosis of the failures in rotator and structural elements, which is one of the main objectives in condition-based maintenance. The concepts, procedures, and challenges of this kind of maintenance are consolidating for real industrial practice.<sup>1</sup> There are several methods focused in the fault detection, mainly with the intention of extracting behaviour patterns able to identify a failure. Among them, the Wavelet Transform (WT) is one of the techniques that has been adopted by a vast amount of applications, frequently replacing the conventional Fourier Transform (FT); however, sometimes it is still used in combination with other techniques as intelligent classifiers, as in the case of Wang and Chen.<sup>2</sup> Peng et al. carried out a bibliographical review on the application of WT on vibration signals to monitoring and fault diagnosis in machines.<sup>3</sup> Researchers such as Douka et al. have developed a method of crack identification for structures based on the continuous wavelet analysis.<sup>4</sup>

Adewusi<sup>5</sup> presented an experimental study, using the wavelet analysis in vibratory signals provided by a rotor. In this previous work, the configuration was performed in a cantilever and with a V-notch of 4 mm, propagating a transversal crack.

Specifically for industrial maintenance, the diagnostics of cracked rotors is a critical subject. This area has focused the attention of many researchers in the last decades. A lot of studies about the dynamics of cracked rotating machinery have been carried out with different methods in order to detect the effects of cracks. Concretely, dynamics and modelling of cracked shafts have been highly developed; however, the inverse problem of the identification of cracks has not been commonly included.<sup>6</sup> A lot of studies have tried to characterize the behaviour of rotors.<sup>7,8</sup> Some wide reviews about the behaviour and modelling of cracked rotating machinery can be consulted,<sup>9,10</sup> as well as more recent studies about this issue.<sup>11</sup> The most common cracks are superficial and transversal that breathe, i.e., that open and close during rotation. There are a lot of theoretical works that propose models of the breathing phenomena.<sup>6</sup> Some classical approximations are the Gash function<sup>12</sup> and the Mayes and Davies function.<sup>13</sup> A review of the classical and modern breathing functions can also be consulted.<sup>14</sup>

Related to rotatory elements, WT theory combined with intelligent classification systems has been applied with success in the last decade in vibration signals from rotors<sup>15</sup> rolling bearing elements using the Continuous Wavelet Transform (CWT)<sup>16</sup> or Discrete Wavelet Transform (DWT).<sup>17,18</sup> In all cases, the selection of the mother wavelet for the transformation is carried out based on experience, and the test of the

most common mother wavelet is used (Morlet, Haar, and the Daubechies family). Related to the level of decomposition, the process is the same, and the authors represent and test different decomposition levels and select the level that presents the biggest differences between the conditions. With non-stationary signals, that means that we are not sure if the selection is the optimum for our purpose, and, obviously, if the machine condition changes (load, rolling element type, or geometry) the patterns will not be the most representative.

Wavelet Packet Analysis (WPT) is based in the DWT analysis, and consists of an improvement of the MRA. Wavelet Packets coefficients can be directly used as features, and they present a high sensibility to failures.<sup>19</sup> In summary, many kinds of fault characteristics can be obtained, principally with the Wavelet coefficients or the Wavelet energy. Since the Wavelet coefficients will highlight the changes in signals, which often predict the occurrence of the fault, the Wavelet coefficients-based features are suitable for early fault detection. However, because slight changes on signals often have small energy, these changes will be easily masked in Wavelet energy-based features.

In the present work, the energy of the coefficients obtained from the WPT will be used in order to automatically select the feature pattern that better describes the fault condition. The mother wavelet applied will be the Daubechies 6 (db6). The coefficients obtained will be used to calculate the energy values in many frequency bands, which will help to find failure patterns to make reliable diagnoses. The study also shows a novel methodology to select the most suitable decomposition level for all applications. The methodology allows the automatic selection of this level. The method will be applied to vibratory signals obtained from the startup of a Jeffcott rotor model that includes the Gash breathing function to model the cracks.

## 2. WAVELET PACKETS TRANSFORM

Wavelet packets transform (WPT) is a generalized form of the Discrete Wavelet Transform (DWT). The DWT of a signal  $x = \{x[i]\}$  is decomposed simultaneously using a high-pass filter ( $h$ ) and a low pass filter ( $g$ ) with impulse response. Output gives the detail coefficients (D) from the high-pass filter and the approximation coefficients (A) from the low-pass one.<sup>20</sup> It is important to note that both filters are related one to each other, and they are known as a quadrature mirror filter. However, since half of the frequencies of the signals have now been removed, half of the samples can be discarded according to Nyquist's rule.<sup>21</sup> The filter outputs are then downsampled by two as Eq. (1):

$$\begin{aligned}
 y_{\text{low}}[n] &= \sum_{i=0}^N x[i] g[2n - i]; \\
 y_{\text{high}}[n] &= \sum_{i=0}^N x[i] h[2n - i];
 \end{aligned}
 \tag{1}$$

where  $N$  is the size of the signal  $x$ . This decomposition has halved the time resolution since only half of each filter output characterizes the signal. However, each output has half the frequency band of the input so the frequency resolution has been doubled.

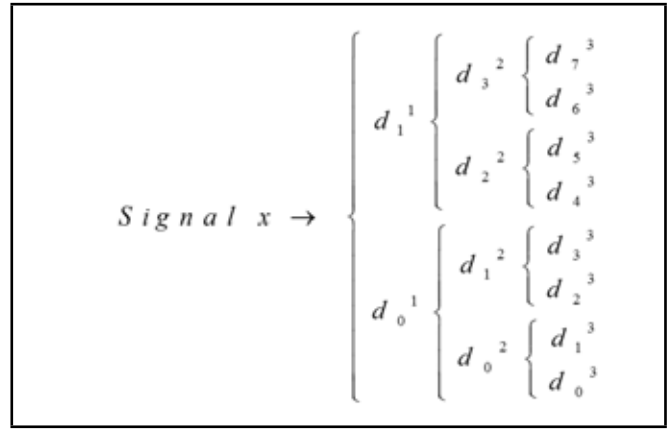


Figure 1. WPT coefficients nomenclature for a decomposition level of 3.

The downsampled signals from the low-pass filter and high-pass filter are referred to as first-level approximation (A) and detail (D) coefficients, respectively. To get the second-level, the application of the filters to coefficients A and D gives as result the approximation of approximation (AA), detail of approximation (DA), approximation of detail (AD), and detail of detail (DD) coefficients, the same procedure is repeated for the rest of levels.

The number of packets generated corresponds to  $2^k$  where  $k$  is the decomposition level. As an example, for a decomposition level 3, 8 packets are obtained and for a level 10, 1024 packets will be generated. At every level of decomposition, the frequency resolution is doubled when filtered while the time resolution is halved by downsampling operation. This decomposition is repeated to further increase the frequency resolution and to reduce the amount of approximation coefficients. This is represented as a binary tree with nodes in a sub-space with different time-frequency localization, and it is shown in Fig. 1.

The tree presented is known as a filter bank.<sup>17</sup> At each level, the signal is decomposed into low and high frequencies. For example, using a sample frequency of 5000 Hz, the bandwidth that can be reconstructed is 2500 Hz. In this case, the bandwidth covered by each packet for decomposition level 3 corresponds to 312.5 Hz, while the range of each packet for a decomposition level 10 is 2.4 Hz, which corresponds to a quite narrow band. The reduction of bandwidth as the WPT decomposition level increases can be seen in Fig. 5a. Due to the decomposition process, the input signal must be a multiple of  $2^k$ .

### 2.1. Relative Wavelet Energy

The energy concept used in the WPT analysis is related to the known concept derived from the Fourier theory.<sup>19</sup> As a previous step to the energy calculus, the selection of a mother wavelet  $\psi(t)$  and the decomposition level  $k$  must be done. The energy ( $E_j$ ) of each packet ( $j$ ) at each decomposition level ( $k$ ), is obtained from the energy of the coefficients of each packet that can be represented as  $\mathbf{d}_j^k = \{d_j^k(1), d_j^k(2), \dots, d_j^k(n)\}$ , where  $n$  is the number of coefficients of each packet  $j$ . Then, the energy of each packet is calculated as shown in Eq. (2):

$$E_j = \sum_{i=1}^n |d_j^k(i)|^2.
 \tag{2}$$

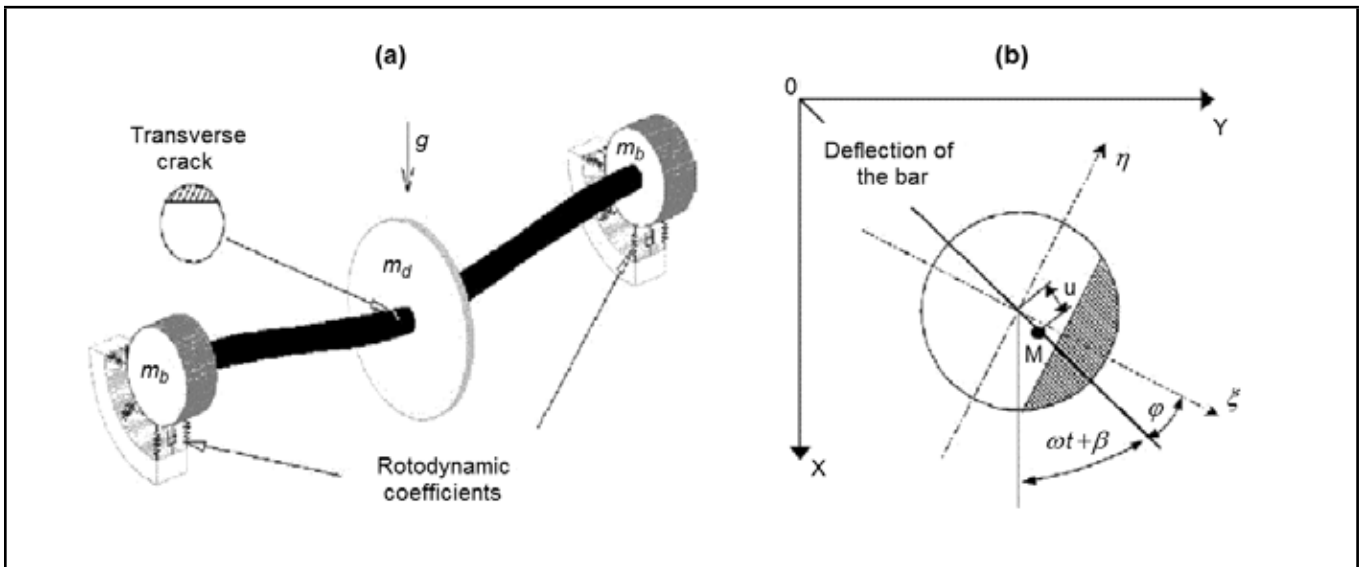


**Figure 2.** (a) Schematic of rotor system with a crack at shaft mid-span indicating disc mass imbalance and crack relative orientations. (b) Coordinate system.

**Table 1.** Jeffcott model parameters.

Case	Shaft Diameter	Shaft Length	Disc Ratio	Disc Mass	Imbalance Mass	Nat. Freq. Flex	$\beta$	$\Delta K_1$	$\Delta K_1$ (Range)
1	0.0157 m	0.3225 m	0.05 m	1.8 kg	$2.10^{-4}$	48 Hz	$0^\circ$	0.0	[0.00:0.001:0.011]
2							$90^\circ$	0.05	[0.038:0.002:0.060]
3							$180^\circ$	0.12	[0.108:0.002:0.13]
4							$270^\circ$	0.22	[0.206:0.002:0.228]

In order to obtain the relative energy, the whole signal energy must be calculated before decomposition by means of Eq. (3):

$$\mathbf{E} = \sum_{i=1}^N E_j; \quad (3)$$

where  $N$  is the number of packets and is  $N = 2^k$ . Finally, relative energy is defined by Eq. (4):

$$\rho_j = \frac{E_j}{\mathbf{E}}, \quad j = 0, \dots, N - 1; \quad (4)$$

where:

$$\sum_j \rho_j = 1. \quad (5)$$

### 3. TEST VIBRATORY SIGNALS

With the aim of obtaining a set of signals to validate the method proposed, a modified Jeffcott rotor has been modelled.<sup>8,22</sup> The model has been developed with the software MATLAB<sup>TM</sup> and Simulink<sup>TM</sup>. The model includes a crack localized in the midspan related to the supports.

In Fig. 2a the Jeffcott rotor can be seen. The crack is oriented in the transversal direction. In Fig. 2b, a transversal section of the crack and the axle is presented. In this figure besides the coordinate system selected an unbalance  $M$  can be positioned in the  $2\pi$  rad of the disc. The fault conditions defined are the following: shaft without crack 0%, slight crack of 12.5% related to the axle diameter, medium crack 25%, and severe crack corresponding to 50%. The stiffness variation is represented in Eq. (6):

$$\Delta K_1 = \frac{\Delta K_\xi + \Delta K_\eta}{K_s}; \quad (6)$$

where  $\Delta K_\xi$  and  $\Delta K_\eta$  are the variation of the stiffness in  $\xi$  and  $\eta$  directions respectively.  $K_s$  is the full axle stiffness. So,  $\Delta K_1 = 0$  corresponds to an axle without a crack,  $\Delta K_1 = 0.05$  to a slight crack,  $\Delta K_1 = 0.12$  to a medium crack, and  $\Delta K_1 = 0.22$  to a severe crack. In order to obtain a complete set of signals with the four subset conditions, two parameters will be modified in the model: the crack depth ( $\Delta K_1$ ) and the unbalance orientation related to the crack ( $\beta$  angulus in Fig. 2b). In Table 1, the summary of all the simulations carried out is presented. The range of the crack depth has been modified in increments of 0.002 and several simulations with four different unbalance orientations have been done.

The four subsets generated are combined with the four unbalance orientations, which are  $\beta = 0$ ;  $\beta = \pi/2$ ;  $\beta = \pi$ ;  $\beta = 3\pi/2$ . A total of 195 signals have been obtained from the different models.

In Fig. 3 the response in  $y$  direction of the four conditions studied in the start-up state (transitory state) are presented versus the speed ratio with respect to the final velocity to reach. In all cases, the final velocity is 2.2 times the critical speed of the system, and the sample frequency used is 5000 Hz (bandwidth 2500 Hz).

### 4. RELATIVE WAVELET ENERGY ANALYSIS

After discussing the theoretical bases and obtaining a set of signatures needed for the test and validation, the process presented in this paper is developed. Vibratory signal corresponds to the first 10 seconds of the actuator start up (transitory state). The signal is decomposed by means of WPT using decomposition levels from 3 to 10. At this stage, packets capacity to contain information to detect and classify defects at any level  $k$  of the WPT is not dismissed. For each packet generated, relative wavelet energy is calculated. At a descendent sort, feature

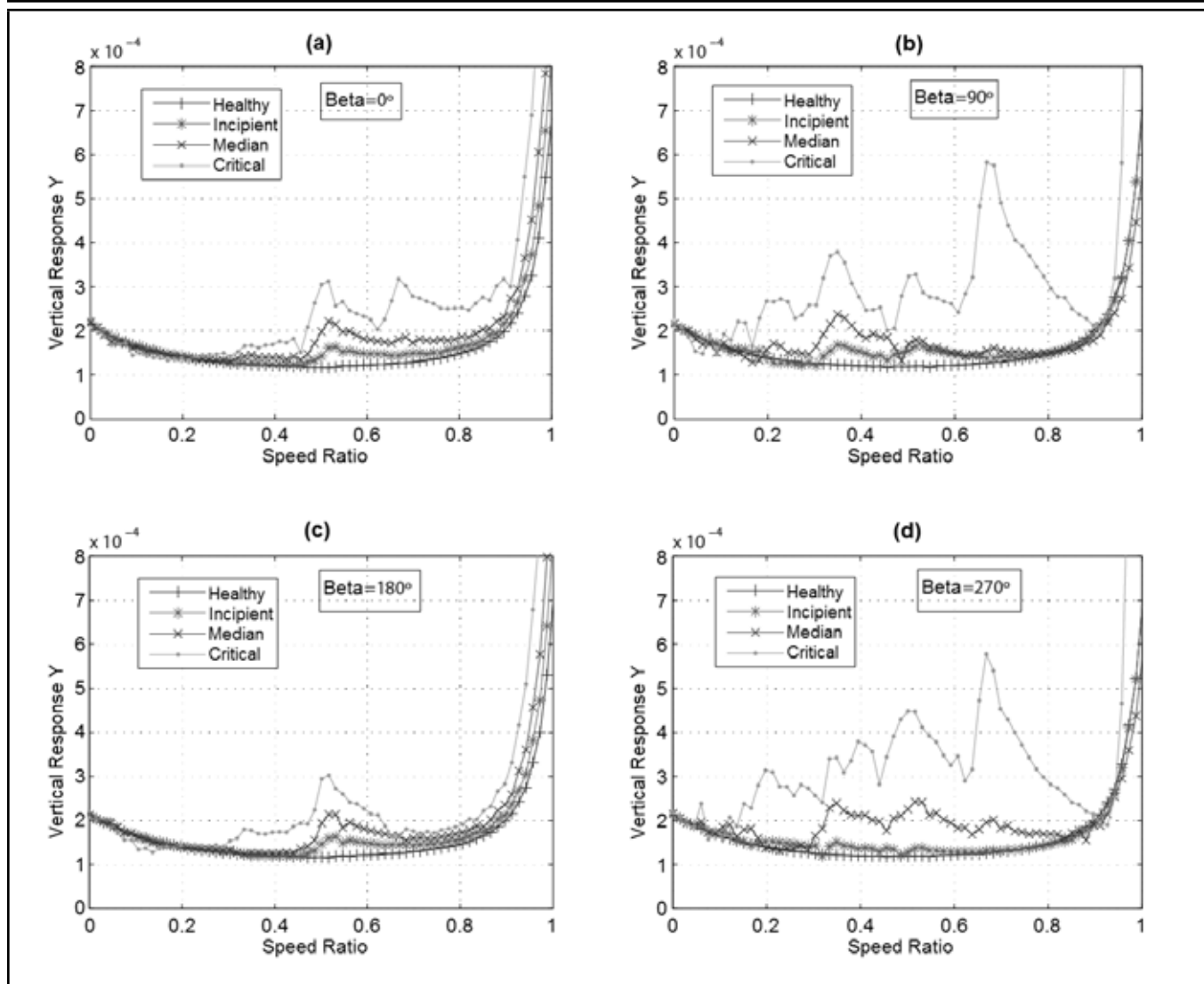


**Figure 3.** Vibratory signatures from the Jeffcott rotor model for different  $\beta$  values and for each shaft condition. Case (a) corresponding to an unbalance orientation respect to the crack of 0 rad, (b) corresponding to an unbalance of  $\pi/2$  rad, (c) and (d) for an unbalance of  $\pi$  and  $3\pi/2$  rad, respectively. Notice that the unbalance orientation of cases (b) and (d) present higher amplitudes.

vectors are generated by the wavelet coefficients included in the first four packets with greater increments in energy. The greater increments in energy are calculated as the bigger differences between the energy of the signals of all the crack conditions studied regarding the case of healthy shaft. These increments of energy when a crack appears are called  $\Delta e$ .

Table 2 shows the procedure for a WPT decomposition level range from 3 to 10, where characteristic patterns are obtained, and ordered by importance. The first column represents the levels of decomposition, the column labeled “First...” which is divided into two columns, corresponds to the packet with the higher relative energy with his frequency band in Hz. At WPT level 3, the biggest changes in the relative energy occur in the package of approximation coefficients or the also called zero level (0). This is because the band has the highest concentration of the most important information, which is at low frequencies, while high frequencies are the details or nuances of the signal. For example, in the case of the human voice, if high frequency components are removed, the voice sounds different, but its message is understood. However, if low frequency components are deleted, the message becomes unrecognizable. In this work, the nuances are due to the presence of cracks, and

in the transformation they are transferred to the high frequency or levels of detail. The level of detail most affected by the presence of the crack will therefore absorb this energy, which indicates the presence of a defect or phenomenon to mention in general. After zero level the following packages with the higher relative energy are 1, 3, and 6 (in the case of WPT level 3). The decomposition continues until level 10 is reached. For the signals used and processed by this method, the levels with higher relative energy changes are 8, 9, and 10.

As can be observed, discarding the zero level in high decomposition levels where the bandwidth is narrower, it can be affirmed that the bigger increments in energy when a crack appears are always in the packet that holds the natural frequency of 48 Hz. The cell that contains the natural frequency at each decomposition level is shaded in all cases in Table 2.

Based on the results, an ANN is used in order to make a smart sort and validate both the performance and efficiency for each decomposition level. In this work a Radial Basis Neural Network (RBF) has been designed<sup>23</sup> to measure the potential of the selected patterns. The training has been conducted with a distribution of input patterns (obtained from the Jeffcott rotor model) corresponding to 75% for training and 25%

**Table 2.** Coefficient number and bandwidth for the four packets with the higher  $\Delta e$  regarding the healthy condition for different decomposition levels.

WPT level	First $\Delta e$ packet		Second $\Delta e$ packet		Third $\Delta e$ packet		Fourth $\Delta e$ packet	
	1st	WideBand [Hz]	2nd	WideBand [Hz]	3rd	WideBand [Hz]	4th	WideBand [Hz]
3	$d_0^3$	0–312.5	$d_1^3$	312.5–625	$d_3^3$	625–937.5	$d_6^3$	1250–1562
4	$d_0^4$	0–156.3	$d_1^4$	156.3–312.5	$d_3^4$	312.5–468.8	$d_2^4$	468.8–625
5	$d_0^5$	0–78.1	$d_1^5$	78.1–156.3	$d_3^5$	156.3–234.4	$d_7^5$	390.6–468.8
6	$d_0^6$	0–39.1	$d_1^6$	39.1–78.1	$d_3^6$	78.1–117.2	$d_2^6$	117.2–156.3
7	$d_0^7$	0–19.5	$d_3^7$	39.1–58.6	$d_1^7$	19.5–39.1	$d_7^7$	97.7–117.2
8	$d_0^8$	0–9.8	$d_6^8$	39.1–48.8	$d_2^8$	29.3–39.1	$d_7^8$	48.8–58.6
9	$d_0^9$	0–4.9	$d_{13}^9$	43.9–48.8	$d_{12}^9$	39.1–43.9	$d_5^9$	29.3–34.2
10	$d_0^{10}$	0.00–2.4	$d_{26}^{10}$	46.4–48.8	$d_{27}^{10}$	43.9–46.4	$d_{10}^{10}$	29.3–31.7

for testing. In Fig. 4, the process of optimization of the RBF neural network can be observed. The network is trained with 22 neurons in the hidden layer and a spread value of 1. The percentage of efficiency is determined for the first three bands with higher  $\Delta e$ , deleting the first one or approximation band, which contains information of energy that lately can be transferred to higher levels. Figure 4a shows the bandwidth for each level of decomposition of the range selected. As can be seen, when the decomposition level increases, the band is reduced (narrowed), refining the area with the highest energy change. In Fig. 4b the success rates of classification depending on the decomposition level are presented. The classification for level  $N = 3$  achieved about a 25% success rate for the three optimal bands. There is an improvement in the levels  $N = 4, 5, 6$ . For the level  $N = 7$  the results are about 97% for the first band and are 100% for the second and third. After that, for levels 8, 9, and 10, a success rate of 100% is achieved also for the first and third band, and 97% for the second one.

The bandwidth is more different with respect to the healthy rotor, in terms of energy, and is 46.4–48.8 Hz. This range covers very precisely the natural frequency of the system, which is 48 Hz. It can be concluded that the presence of a crack significantly affects the energy nearby the natural frequencies.

As the decomposition level decreases, less information is available to detect failure patterns, but also the computational cost is reduced. For this reason, the optimal decomposition level to achieve is the lowest possible that gives a success rate in the classification higher than a limit imposed and that allows locating the failure in a narrow enough bandwidth. For example, in this case, if the limit of classification is set to 98%, and a bandwidth of less than 10 Hz is imposed, the optimal decomposition level is 8.

## 5. CONCLUSIONS AND FUTURE WORK

In this paper, the extraction and automatic selection of patterns through the application of the WPT and analysis of the relative energy of wavelet packets for either incipient fault level or higher has been presented. The method lets selecting the approximation and detail level that can discretize the problem by creating defects codes that are easily adaptable to automatic diagnosis and classification.

This demonstrates that the WPT technique is an excellent tool for the extraction of characteristic patterns of vibration signals, even in the incipient fault diagnosis. Concretely, the energy of WPT has proven its reliability, because the frequency

band that holds bigger differences with the healthy rotor corresponds to the natural frequency, as could be predicted.

Intelligent classification systems are used to optimize the process of analysis and selection of patterns, making comparisons with high sensitivity levels. The best patterns extracted from vibration signals are processed by WPT and classified efficiently using RNA levels of accuracy above 97%.

As future work, the authors think that it would be very interesting to prove the reliability of this method in experimental signals obtained from real systems in order to improve the predictive maintenance of turbomachinery. Also it would be very useful to prove the effectiveness of this methodology in systems that do not reach high speeds.

## ACKNOWLEDGEMENTS

The financial support of the regional government of Madrid and Carlos III University is gratefully acknowledged through the Project MADBOT 2011/00130/001.

## REFERENCES

- Ahmad, R., Kamaruddin, S. An overview of time-based and condition-based maintenance in industrial application, *Computers & Industrial Engineering*, **63**, 135–149, (2012).
- Wang, H., Chen, P. Intelligent diagnosis method for rolling element bearing faults using possibility theory and neural network, *Computers & Industrial Engineering*, **60**, 511–518, (2011).
- Peng, Z., Chu, F. Application of the wavelet transform in machine condition monitoring and fault diagnostics: a review with bibliography, *Mechanical Systems and Signal Processing*, **18**, 199–221, (2004).
- Douka, E., Loutridis, S., Trochidis, A., Crack identification in beams using wavelet analysis, *International Journal of Solids and Structures*, **40**, 3557–3569, (2003).
- Adewusi, S. A. Wavelet analysis of vibration signals of an overhang rotor with a propagating transverse crack, *Journal of Sound and Vibration*, **5**, 777–793, (2001).
- Bachshmid, N., Penacci, P., Editorial, Crack effects in rotordynamics, *Mechanical Systems and Signal Processing*, **22**, 761–762, (2008).

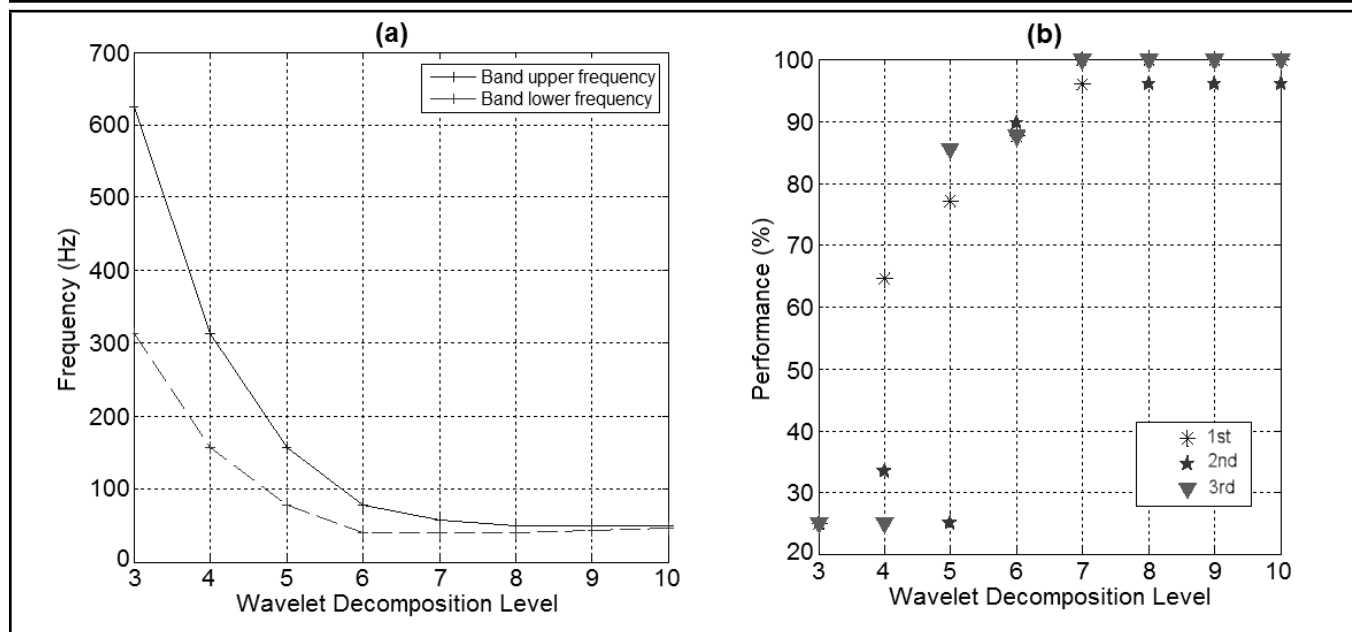


Figure 4. Optimum frequency band and classification performance.

- <sup>7</sup> Chancey, V. C., Flowers, G. T., Howard, C. L. Characterisation of transient behaviours in rotordynamic vibrations from experimental data using harmonic wavelets, *International Journal of Acoustics and Vibration*, **6**, 15–22, (2001).
- <sup>8</sup> Diken, H., Alnefaie, K. Startup dynamic behaviour of a Jeffcott rotor, *International Journal of Acoustics and Vibration*, **10**, 83–88, (2005).
- <sup>9</sup> Gasch, R. Dynamic behavior of the Laval rotor with a transverse crack, *Mechanical Systems and Signal Processing*, **22**, 790–804, (2008).
- <sup>10</sup> Bachschmid, N., Penacci, P., Tanzi, E. Some remarks on breathing mechanism on non-linear effects and on slant and helicoidal cracks, *Mechanical Systems and Signal Processing*, **22**, 879–904, (2012).
- <sup>11</sup> Kulesza, Z., Sawicki, J. T. Rigid finite elements model of a cracked rotor, *Journal of Sound and Vibration*, **331**, 4145–4169, (2012).
- <sup>12</sup> Gash, R. Dynamic behavior of a simple rotor with a cross-sectional crack, *Proc. Institution of Mechanical Engineers Conference on Vibration in Rotating Machinery*, 178/76, Cambridge, UK, (1976).
- <sup>13</sup> Mayes, I. W. and Davies, W. G. R. The vibrational behavior of a rotating shaft system containing a transverse crack, *Proc. Institution of Mechanical Engineers Conference on Vibration in Rotating Machinery*, 168/76, Cambridge, UK, (1976).
- <sup>14</sup> Al-Schudeifat, M. A. and Butcher, E. A. New breathing functions for the transverse breathing crack of the cracked rotor system: Approach for critical and subcritical harmonic analysis, *Journal of Sound and Vibration*, **330**, 526–544, (2011).
- <sup>15</sup> Srinivas, H. K., Srinivasan, K. S., Umesh, K. N. Role of an artificial neural network and a wavelet transform for condition monitoring of the combined faults of unbalance and cracked rotors, *International Journal of Acoustics and Vibration*, **15** (3), 121–127, (2010).
- <sup>16</sup> Li, L., Qu, L., Liao, X. Haar wavelet for machine fault diagnosis, *Mechanical Systems and Signal Processing*, **21**, 1773–1786, (2007).
- <sup>17</sup> Castejón, C., Lara, O., Garcia-Prada, J. Automated diagnosis of rolling bearings using MRA and neural networks, *Mechanical Systems and Signal Processing*, **24**, 289–299, (2010).
- <sup>18</sup> Lei, Y., He, Z., Zi, Y. Application of an intelligent classification method to mechanical fault diagnosis, *Expert Systems with Applications*, **36** (6), 9941–9948, (2009).
- <sup>19</sup> Hu, Q., He, Z., Zhang, Z., Zi, Y. Fault diagnosis of rotating machinery based on improved wavelet package transform and svms ensemble, *Mechanical system and signal processing*, **21**, 688–705, (2007).
- <sup>20</sup> Mallat, S. *A Wavelet Tour of Signal Processing*, Academic Press, (1998).
- <sup>21</sup> Polikar, R. *The Wavelet Tutorial*, Rowan University, College of Engineering, (1996).
- <sup>22</sup> Litak, G., Sawicki, J. T. Intermittent behaviour of a cracked rotor in the resonance region, *Chaos, Solitons & Fractals*, **42** (3), 1495–1501, (2009).
- <sup>23</sup> Lara, O., Castejón, C., Garcia-Prada, J. Bearing fault diagnosis based on neural network classification and wavelet transform, *WSEAS Transaction on Signal Processing*, **2** (10), 1371–1378, (2006).



---

---

# Study of Automobile Suspension System Vibration Characteristics Based on the Adaptive Control Method

**Ruqiang Mou and Li Hou**

*School of Manufacturing Science and Engineering, Sichuan University (610065), Chengdu, China*

**Yiqiang Jiang and Yong Zhao**

*School of Leshan Vocational and Technical College(614000), Leshan, China*

**Yongqiao Wei**

*School of Manufacturing Science and Engineering, Sichuan University (610065), Chengdu, China*

(Received 9 December 2013; accepted 30 May 2014)

An automotive suspension determines both the driving stability and comfort of the vehicle occupants. This paper establishes two kinds of two degrees of freedom for the automobile suspension vibration model and uses the PID controller to establish an automobile suspension adaptive open-loop and closed-loop control system. Respectively, by step interference, white noise and sinusoidal interference for the input, studying the vibration characteristics of the vibration model in the vertical direction. By numerical simulation, we obtain the suspension of the vertical displacement and acceleration-time graphs. The simulation results show that the vibration characteristics of the first model are more in accordance with the actual situation of the car, and the closed-loop control is better than the open-loop control. The adaptive closed-loop control system can reduce the output displacement of automobile suspension to around 1% of the interference road input displacement. The output acceleration value is small, and the acceleration changes smoothly. The results verify the rationality and validity of the automobile suspension model and adaptive control system, which provides a theoretical foundation for the design and optimization of the automobile suspension system.

---

## 1. INTRODUCTION

Suspensions are an important part of the car chassis as they directly determine the car's ride comfort and handling stability, but because of their high costs and high energy demand, their application is restricted. Hence, the semi-active suspension system is now used in the automobile suspension structure.

Over the years, many studies on suspension systems have been done.<sup>1-15</sup> Tomoaki Mori<sup>1</sup> put forward an adaptive damper controller for compensating the nonlinear hysteresis dynamics of the MR damper. Kayhan Gulez,<sup>2</sup> Ali Ahmed Adam,<sup>12</sup> and Hua Li<sup>14</sup> use an algorithm method to research the nonlinear characteristics for the semi-active suspension of automobiles. Enrico Pellegrini<sup>3</sup> and Zhao Cheng<sup>4</sup> build a semi-active suspension system model based on control strategy in order to describe the damper behaviour. Li Shaohua<sup>5</sup> and Liang Shan<sup>6</sup> studied the two degrees of freedom 1/4 automobile suspension model; the former used a multi-scale method to study the combination of multi-frequency excitation resonance characteristics, and the latter researched the suspension model chaotic vibration occurring in road roughness excitation. Ren Chenglong<sup>7</sup> established a single degree of freedom model of automobile suspension under random excitation; the numerical simulation verifies the automobile suspension chaotic vibration characteristic.<sup>7,11</sup> Jiammin Sun and Qingmei Yang<sup>8</sup> established a suspension model and analysed the comfort and

safety based on the adaptive filter theory. Abu-Khudhair,<sup>9</sup> Changizi,<sup>10</sup> and Barr<sup>13</sup> use a fuzzy logic technique to build the semi-active automobile suspension systems control, which has a significantly fewer number of rules in comparison to existing fuzzy controllers. Hung Yichen<sup>15</sup> proposes a functional-approximation based adaptive sliding controller with fuzzy compensation for an active suspension system.

The above studies on automobile suspension do not simultaneously propose two vibration models based on the adaptive control method so they can't prove which model is more suitable for an automobile suspension system. Hence, this paper gives two automobile suspension system vibration models using the adaptive control method and two control algorithms consisting of PID controllers. This paper also studies suspension system vibration characteristics with step input, white-noise input, and sinusoidal input as the external excitation. By numerical simulation, this study obtains the displacement and acceleration characteristics. Comparing the results of the two models, we find that when examining the engine and the suspension as a whole, the suspension system vibration characteristics more closely match the actual conditions, which is conducive for designing the most appropriate automobile suspension model.

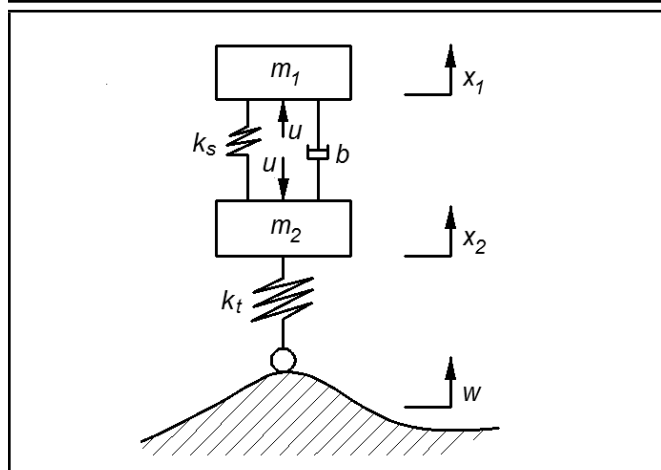


Figure 1. The first model.

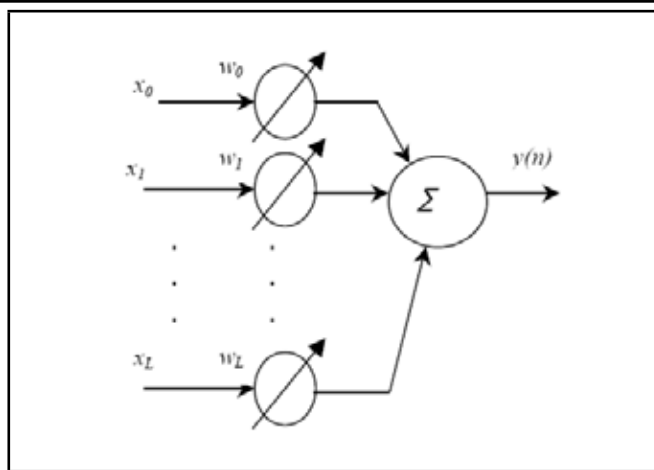


Figure 3. Adaptive linear combiner.

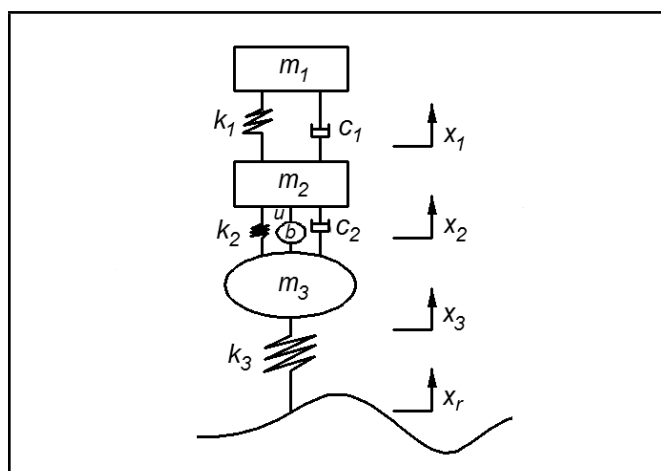


Figure 2. The second model.

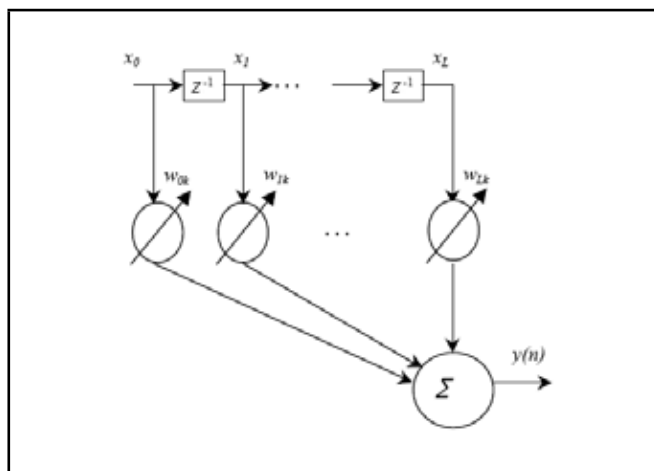


Figure 4. Adaptive transversal filter.

## 2. AUTOMOBILE SUSPENSION SYSTEMS

### 2.1. Vibration System Modelling

A car is mainly composed of wheels, suspension, and engines, and the automobile body vibration will directly affect the handling and safety. The vibration in the vertical direction of the suspension determines the performance of the body. This study establishes two kinds of two degrees of freedom automobile suspension vibration models as shown in Fig. 1 and Fig. 2. The first model depicts the engine and suspension as a whole, the second model considers the engine and suspension separately. Suspension vertical displacement and acceleration is an important indicator of automotive comfort and handling. This article will focus on the suspension vertical displacement and acceleration.<sup>3,5,6,8-10</sup>

According to the vibration model in Fig. 1, the following dynamic differential equation is obtained:<sup>14,15</sup>

$$\begin{cases} m_1 \ddot{x}_1 = k_s(x_2 - x_1) + b \left( \frac{dx_2}{dt} - \frac{dx_1}{dt} \right) + u \\ m_2 \ddot{x}_2 = -k_s(x_2 - x_1) - b \left( \frac{dx_2}{dt} - \frac{dx_1}{dt} \right) - u + k_t(w - x_2). \end{cases} \quad (1)$$

Make  $x = x_1 - x_2$ , by the Laplace transform can be obtained:

$$\begin{cases} X(s) = [U(s) - G_f(s)W(s)] G_p(s) \\ G_f(s) = \frac{m_1 k_t s^2}{(m_1 + m_2)s^2 + k_t} \\ G_p(s) = \frac{m_1 k_t s^2}{m_1 m_2 s^4 + b(m_1 + m_2)s^3 + k_t m_1 s^2 + k_s(m_1 + m_2)s^2 + b k_t s + k_s k_t}. \end{cases} \quad (2)$$

According to the vibration model in Fig. 2, the following dynamic differential equation is obtained:<sup>14,15</sup>

$$\begin{cases} m_1 \ddot{x}_1 + c_1 \left( \frac{dx_1}{dt} - \frac{dx_2}{dt} \right) + k_1(x_1 - x_2) = 0 \\ m_2 \ddot{x}_2 + c_2 \left( \frac{dx_2}{dt} - \frac{dx_3}{dt} \right) + k_2(x_2 - x_3) + \\ \quad c_1 \left( \frac{dx_2}{dt} - \frac{dx_1}{dt} \right) + k_1(x_2 - x_1) - u = 0 \\ m_3 \ddot{x}_3 + c_2 \left( \frac{dx_3}{dt} - \frac{dx_2}{dt} \right) + k_2(x_3 - x_2) + \\ \quad k_3(x_3 - x_r) + u = 0. \end{cases} \quad (3)$$

Make  $x = x_2 - x_3$ , by the Laplace transform can be obtained:

$$\begin{cases} X(s) = [U(s) + G_f(s)X_r(s)] G_p(s) \\ G_f(s) = \frac{k_3 c_2 s + k_2 k_3 - k_3}{s^2 + k_3} \\ G_p(s) = \frac{t_8 s^8 + t_7 s^7 + t_6 s^6 + t_5 s^5 + t_4 s^4 + t_3 s^3 + t_2 s^2}{n_{10} s^{10} + n_9 s^9 + n_8 s^8 + n_7 s^7 + n_6 s^6 + n_5 s^5 + n_4 s^4 + n_3 s^3 + n_2 s^2 + n_1 s + n_0}. \end{cases} \quad (4)$$

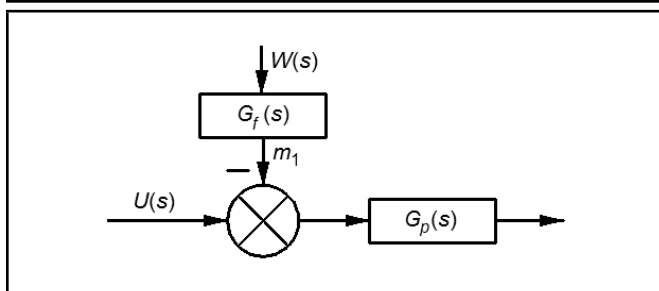


Figure 5. The automobile suspension open-loop control system (without PID).

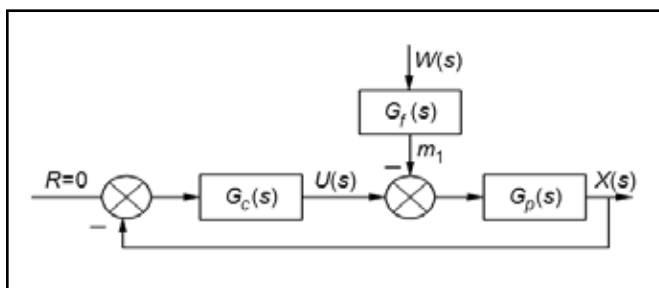


Figure 6. The automobile suspension closed-loop control system (with PID).

## 2.2. Adaptive Control Method

The adaptive control method is useful when great changes have taken place with the input signal or disturbance signal and the system automatically adjusts to maintain the output that meets the necessary requirements. The adaptive linear combiner structure shown in Fig. 3,  $x_0, x_1, \dots, x_L$  are signal vectors, and  $w_0, w_1, \dots, w_L$  is a set of adjustable weight. Fig. 3 depicts an input corresponding to an adjustment of weight and the final output of the system of linear combinations of the input. As can be seen from this figure, the system is linear.<sup>8</sup>

From the adaptive control method and Fig. 3, the following equation can be established:<sup>8</sup>

$$\begin{cases} X^T(n) = [x(n), x(n-1), \dots, x(n-L+1)] \\ W^T = [w_1, w_2, \dots, w_L] \\ y(n) = \sum_{j=1}^L w_j x(n-j+1) = W^T X(n) \\ e(n) = d(n) - y(n) \\ E[e^2(n)] = E[d^2(n)] - 2R_{xd}^T W + W^T R_{xx} W; \end{cases} \quad (5)$$

where  $X^T$  is input vector,  $W^T$  is weight vector,  $L$  is the length of filter,  $y(n)$  is the output of the filter,  $e(n)$  is the error signal,  $R_{xd}$  is the cross-correlative function of  $x(n)$  and  $d(n)$ , and  $R_{xx}$  is the auto-correlative function of  $x(n)$ .

When an input of a filter is formed from a series of delayed samples of some signal, such filter structure is called adaptive transversal filter structure,<sup>8</sup> as shown in Fig. 4.

The following equation<sup>8</sup> can be established according to Fig. 4:

$$\begin{cases} W(n+1) = W(n) - \mu \nabla e^2(n) \\ \Delta e^2(n) = -2e(n)x(n) \\ y(n) = W^T X(n) \\ e(n) = d(n) - W^T X(n) \\ W(n+1) = W(n) + 2\mu e(n)X(n); \end{cases} \quad (6)$$

where  $W(n+1)$  is the next moment that equals the weight value of  $w(n)$ ,  $\mu$  is the gain constant, which controls adaptive speed and stability,  $\nabla e(n)$  is the error function, and  $\Delta e(n)$  is the error gradient function.

## 2.3. Constructed Automobile Suspension Control System

Random road is the disturbance input of the suspension system, which decides the car driving performance. So it is important to build a useful control system to reduce or eliminate bad interference. The following control system is built on the assumption that the system's expected output is  $X = 0$ .<sup>1,2,12,13</sup>

$$G_c = \frac{K_d s^2 + K_p s + K_i}{s} \quad (7)$$

where  $G_c$  is PID controller.  $K_d = 5$ ,  $K_i = 8$ ,  $K_p = 95$ , Fig. 7 is the Bode diagram of  $G_c$ .

Figure 7 gives the suspension system bode diagram without correction, with correction, and after correction. From the figure, it can be obtained that without correction, the system phase changes dramatically near degree 180, and at that time, if the system is to increase the gain or suffer some kind of disturbance, the system phase may become negative, making the system unstable. After the correction, the system phase beats near degree 0, which effectively improves the stability of the system.

## 3. AUTOMOBILE SUSPENSION VIBRATION MODEL RESPONSE

### 3.1. Step Disturbance Response Characteristics in the First Model

Take the system parameters:  $m_1 = 2500$  kg,  $m_2 = 320$  kg,  $k_s = 10000$  N/m,  $b = 140000$  Ns/m into Eq. (2). The simulation results as shown in the Fig. 8 and Fig. 9.

As can be seen from Fig. 8 and Fig. 9, the response speed of the open-loop control system is faster than that of the closed-loop system, but the closed-loop system has the function of adaptive control, the timely adjustment of the deviation of system, the reduction of the vibration of the system, and the improvement of the car's stability and security.

### 3.2. Step Disturbance Response Characteristics in the Second Model

Take the system parameters:  $m_1 = 100$  kg,  $m_2 = 200$  kg,  $m_3 = 30$  kg,  $k_1 = 400000$  N/m,  $k_2 = 20000$  N/m,  $k_3 = 180000$  N/m,  $c_1 = 4000$  Ns/m,  $c_2 = 500000$  Ns/m into Eq. (4) and the simulation results as shown in Fig. 10 and Fig. 11

From Fig. 10 and Fig. 11, we can see that the response of two models is similar. The amplitude of closed-loop control system is smaller than the open-loop system, and the closed-loop control system response speed is slower than that of the open-loop system. At the time of automobile start, the amplitude of the automobile is 0, which indicates that the system has good stability, and ensures a smooth start of the car. But shortly after running the car, there will be a more serious jitter, which greatly affects the normal running of the car.

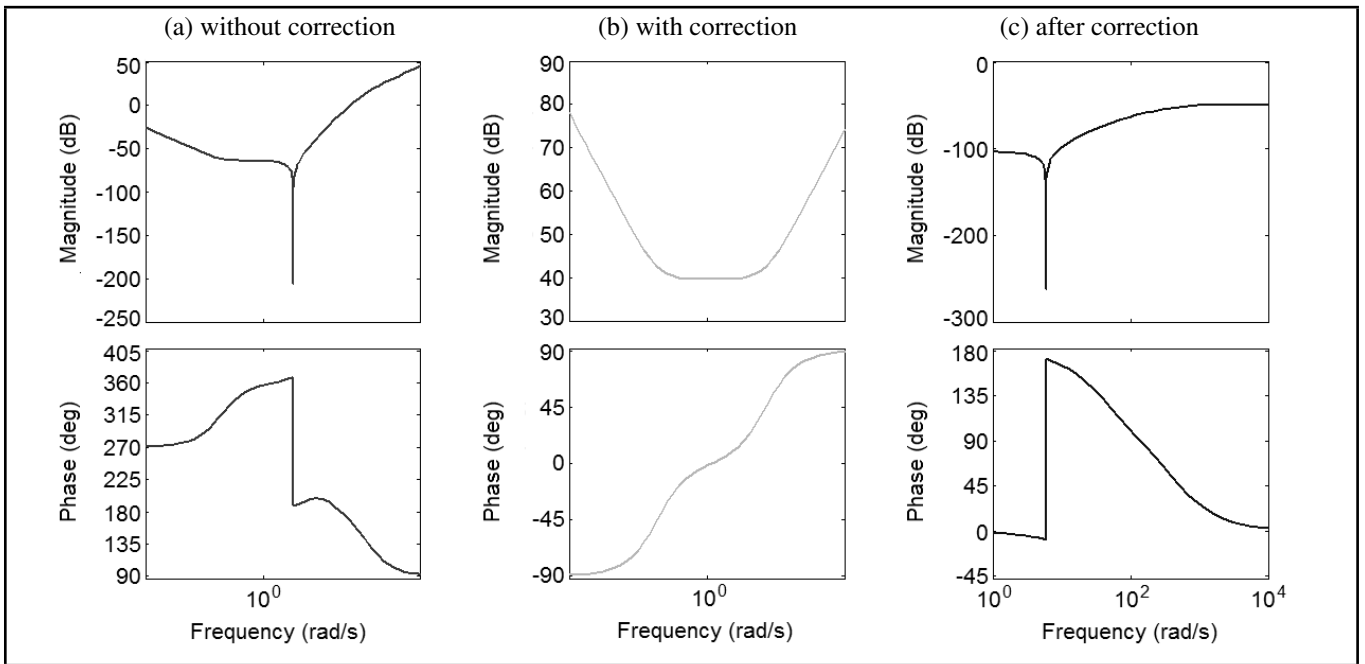


Figure 7. The bode diagram.

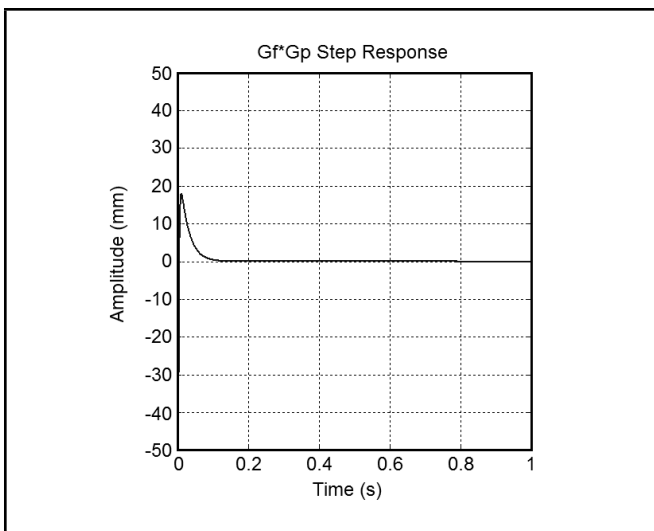


Figure 8. Step interference open-loop system response.

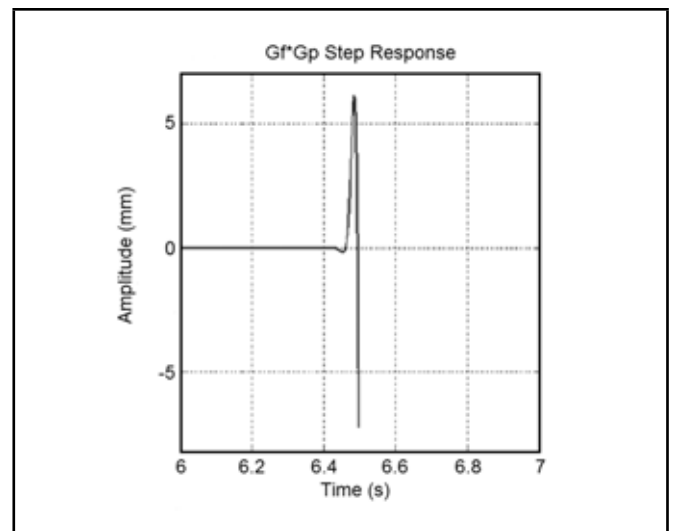


Figure 10. Step interference open-loop system response.

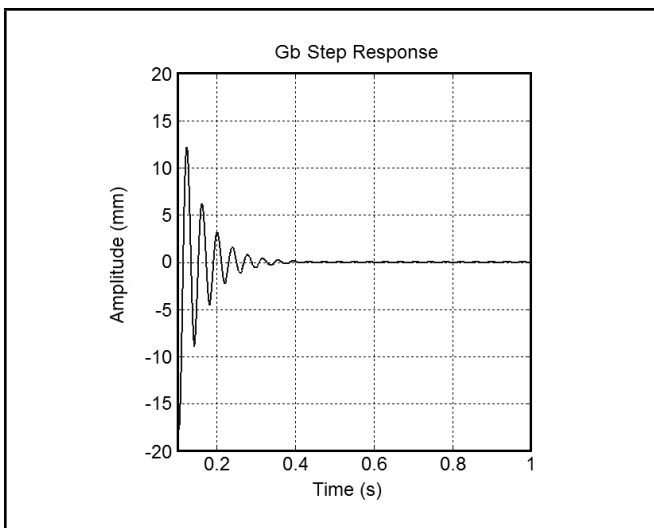


Figure 9. Step interference closed-loop system response.

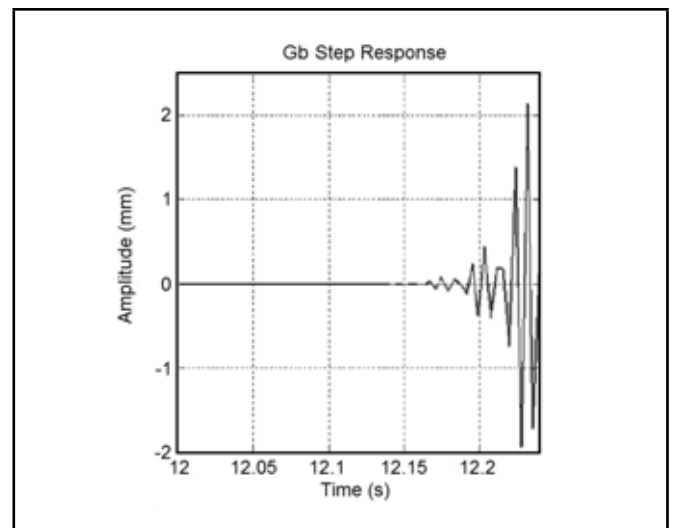


Figure 11. Step interference closed-loop system response.

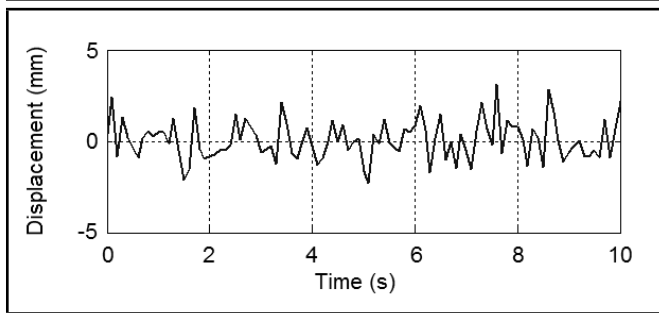


Figure 12. White-noise signal.

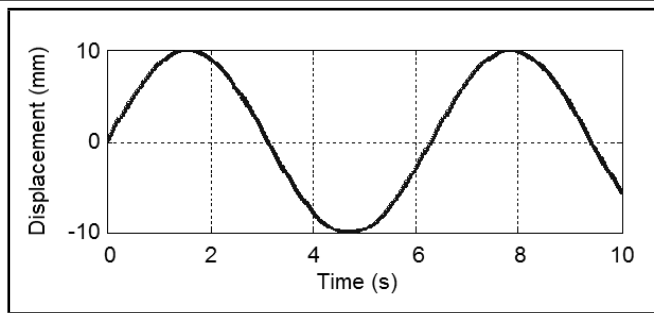


Figure 16. Sinusoidal interference signal.

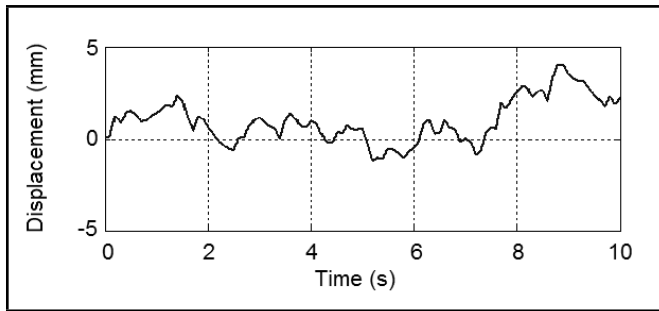


Figure 13. Integral white-noise signal.

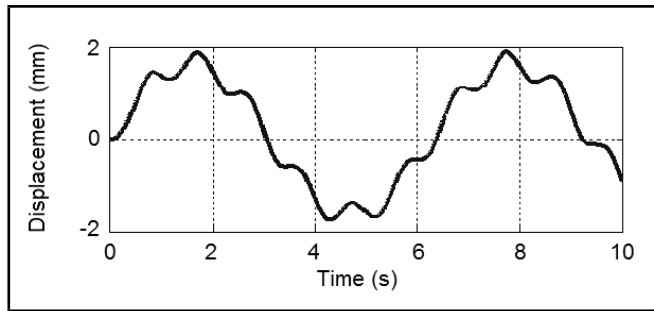


Figure 17. Integral sinusoidal interference signal.

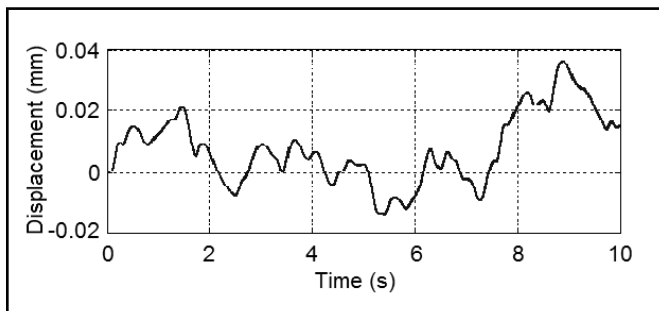


Figure 14. Automotive suspension displacement-time curve under white noise.

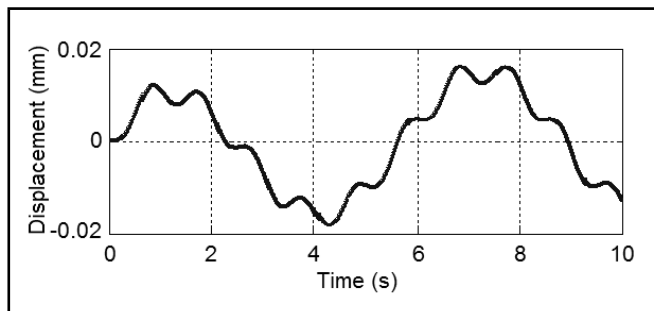


Figure 18. Automotive suspension displacement-time curve under the sinusoidal interference signal.

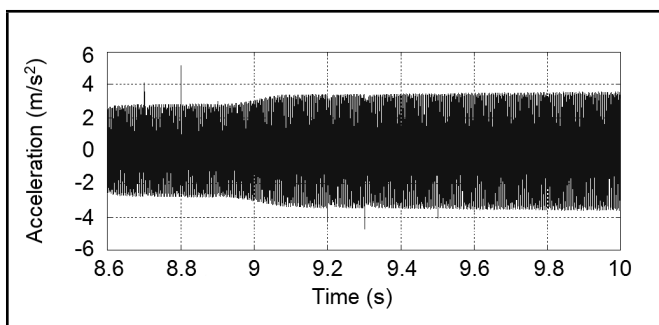


Figure 15. Automotive suspension acceleration-time curve under white noise.

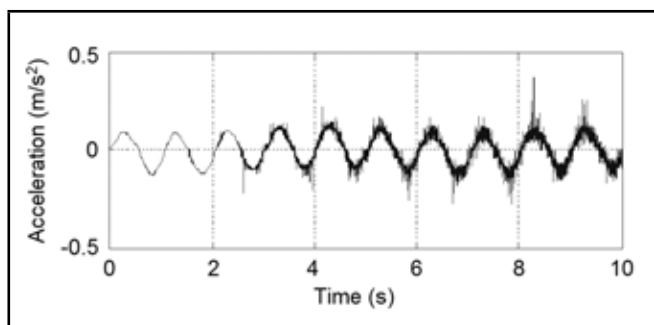


Figure 19. Automotive suspension acceleration-time curve under the sinusoidal interference signal.

By comparing the two models, it can be found that in the first model a serious quiver appears at first, but the jitter time is short, and the car can realize the adaptive control within a few minutes, quickly reducing the car jitter, and ensuring that the car is moving. The first model better reflects the vibration characteristics of a vehicle suspension system, so this paper will do further research of this model.

As the interference of the system-step response has already been studied, the following will study the vehicle suspension

system response characteristics under white noise and sinusoidal excitation.

Figure 12 to Fig. 15 shows the suspension system in the white noise excitation. By the adaptive closed-loop control, the amplitude of the suspension system is reduced to about 1% of the excitation, the acceleration of the suspension is about  $4 \text{ m/s}^2$ , the acceleration change is relatively stable, and larger acceleration values occur at only very few moments. The adaptive closed-loop control system has a good white-road noise

interference protective effect, affectively reducing the amplitude and acceleration of the suspension, guaranteeing the car to drive normally.

Figure 16 to Fig. 19 depict the suspension system in the sinusoidal interference signal excitation. In these figures it can be seen that the maximum displacement of the vertical direction is reduced to about 1% of the disturbance input. The acceleration of the overall image changes as a sinusoidal, and the maximum acceleration is  $0.4 \text{ m/s}^2$ . Relative to the high-speed operation of the car, the car's acceleration has little effect on normal driving. By comparing the results, we can find that the adaptive closed-loop control system being used in sinusoidal interference signal excitation is more effective than in white-noise interference excitation, and the results once again validate the practicality and effectiveness of the adaptive closed-loop control system.

## 4. CONCLUSIONS

(1) This paper establishes two kinds of two degrees of freedom automobile suspension vibration models; two models responses are studied under step and white-noise interference in both an open and closed-loop system. By contrast and analysis, the numerical simulation results show that the engine and suspension as a whole suspension vibration model is more likely to meet the needs for the actual operation of the automobile.

(2) This paper uses proportional, integral, and differential elements to form the PID controller, and makes up the adaptive closed-loop control system to study the vertical displacement and acceleration response of the automobile suspension system.

(3) Numerical simulation results show that the adaptive closed loop control system can reduce the vertical direction amplitude of the suspension to 1% of the original interference input displacement, while the maximum acceleration is no more than  $5 \text{ m/s}^2$ , and the acceleration changes smoothly. The results demonstrate the rationality and effectiveness of the design of the adaptive closed-loop control system and provide a theoretical basis for the design of automobile suspension control systems.

## REFERENCES

- <sup>1</sup> Mori, T., Nilkhamhang, I., and Sano, A. Adaptive semiactive suspension system by linearly parameterized controller, *Proc. SICE Annual Conference 2007*, 1275–1280, Takamatsu, Japan, (2007).
- <sup>2</sup> Adam, A. A., Gulez, K., Aliskan, I., Altun, Y., Guclu, R., and Metin, M. Steering DTC algorithm for IPMSM used in electrical automobile (EV)- with fast response and minimum torque ripple, *Proc. 11th IEEE International Workshop on Advanced Motion Control*, 279–283, Nagaoka, Japan, (2010).
- <sup>3</sup> Pellegrini, E., Spirk, S., Pletschen, N., and Lohmann, B. Experimental validation of a new model-based control strategy for a semi-active suspension system, *Proc. 2012 American Control Conference Fairmont Queen Elizabeth*, 516–518, Montreal, Canada, (2012).
- <sup>4</sup> Zhao, C., Hu, Z., and Chen, D. Sliding mode varying structure control of semi-active suspension, *China Journal of Highway and Transport*, **20** (3), 109–113, (2007).
- <sup>5</sup> Li, S. and Yang, S. Investigation on Combination Resonance in a Nonlinear Vehicle Suspension System with Multi-frequency Excitations, *Journal of Shijiazhuang Railway Institute*, **16** (1), 20–23, (2003).
- <sup>6</sup> Liang, S., Zheng, J., Zhu, Q., and Liu, F. Numerical and Experimental Investigations on Chaotic Vibration of A Nonlinear Vehicle Model Over Road Excitation, *Journal of Mechanical Strength*, **34** (1), 7–11, (2012).
- <sup>7</sup> Ren, C. and Zhang, Y. Chaos Characteristics of Automobile Suspension Vibration, *Journal of Jinan University (Science and Technology)*, **24** (2), 198–200, (2010).
- <sup>8</sup> Sun, J. and Yang, Q. Comfort and safety analysis of automotive active suspension based on adaptive filter theory, *Proc. 4th IEEE Conference on Industrial Electronics and Applications ICIEA 2009*, 1730–1733, Xi'an, China, (2009).
- <sup>9</sup> Abu-Khudhair, A., Muresan, R., and Yang, S. X. Fuzzy control of semi-active automotive suspensions, *Proc. 2009 IEEE International Conference on Mechatronics and Automation*, 2118–2121, Changchun, China, (2009).
- <sup>10</sup> Changizi, N., Rouhani, M., and Sheiie, N. Using fuzzy logic to control one quarter-car suspension system, *Proc. 2010 International Conference on Computer, Mechatronics, Control and Electronic Engineering (CMCE)*, 530–532, Changchun, China, (2010).
- <sup>11</sup> Ren, C. Chaos characteristics of suspension vibration under quasi-impulse excitation, *Noise and Vibration Control*, **8** (4), 43–44, (2012).
- <sup>12</sup> Adam, A. A. and Gulez, K. Hybrid filter topology to minimize harmonics and EMI noise in PMSM with HDTC, *Proc. 35th Annual Conference of IEEE Industrial Electronics IECON'09*, 1583–1585, Porto, Portugal, (2009).
- <sup>13</sup> Barr, A. J. and Ray, J. I. Control of an active suspension using fuzzy logic, *Proc. Fifth IEEE International Conference on Fuzzy Systems*, **1**, 42–47, (1996).
- <sup>14</sup> Li, H., Tang, C., Yang, D., and Tao, X. Simulation of semi-active air suspension based on neural network-adaptive control algorithm, *Proc. 2009 Second International Conference on Intelligent Computation Technology and Automation*, **2**, 237–239, Changsha, China, (2009).
- <sup>15</sup> Chen, H.-Y. and Huang, S.-J. Adaptive sliding controller for active suspension system, *Proc. 2005 International Conference on Control and Automation (ICCA'05)*, **1**, 282–287, (2005).

# Vibrations of Completely Free Rounded Regular Polygonal Plates

C. Y. Wang

Departments of Mathematics and Mechanical Engineering Michigan State University, East Lansing, MI 48824

(Received 28 February 2013; accepted 5 March 2014)

The vibrations of completely free polygonal and rounded polygonal plates are important for large floating or space platforms. The problem is solved by an improved Ritz method on a class of homotopy shapes. The first five frequencies are determined, and interesting evolutions of mode shapes are shown.

## 1. INTRODUCTION

Vibration of elastic plates is essential in structural mechanics. Basic data (frequencies, mode shapes) of plate vibrations can be found in the works of Leissa<sup>1</sup> and Blevins.<sup>2</sup> Exact solutions exist for the vibration of circular and annular plates, some simply supported triangular plates, and rectangular plates with two simply supported opposite edges.<sup>3</sup> For all other shapes or boundary conditions numerical means are necessary.

The vibrations of regular polygonal plates have also been studied, notably Conway<sup>4</sup> using point match, Shahady et al.<sup>5</sup> using conformal mapping, Irie et al.<sup>6</sup> using membrane analogy, Liew and Lam<sup>7</sup> using a Ritz method, and Ghazi et al.<sup>8</sup> using finite elements. These sources however, only consider simply supported or clamped edges.

We are interested in the vibration of completely free plates, i.e. all edges are free. The study is important in the design of very large ocean floating structures (e.g.<sup>9</sup>) and also large structures in space, such as platforms and solar panels (e.g.<sup>10</sup>). These structures have nominal dimensions in kilometres, much larger than their thicknesses, thus can be modelled as thin plates.

Aside from the data presented by Leissa,<sup>1</sup> the vibrations of completely free rectangular plates includes Leissa<sup>11</sup> using the Ritz method, Gorman<sup>12</sup> using a superposition method, Behnke and Mertins<sup>13</sup> using the Ritz method, and Mochida and Ilanko<sup>14</sup> using superposition and finite differences. The free triangular plate was considered by Leissa and Jaber<sup>15</sup> and the free trapezoidal plate by Qatu et al.,<sup>16</sup> both sources using the Ritz method. However, the natural vibration of the free regular polygonal plate has not been fully investigated.

The purpose of the present note is to study not only the vibrations of completely free regular polygonal plates, but also the more general class of rounded regular polygonal plates, which includes the polygonal plates as special cases. Rounding the corners of a polygonal plate has definite advantages in terms of savings in material, weight, and boundary length, while it changes little in the structural strength or vibration properties.

## 2. THE HOMOTOPY SHAPES

The homotopy shapes are first introduced by Wang<sup>17</sup> and applied to the vibration of membranes. The homotopy transform

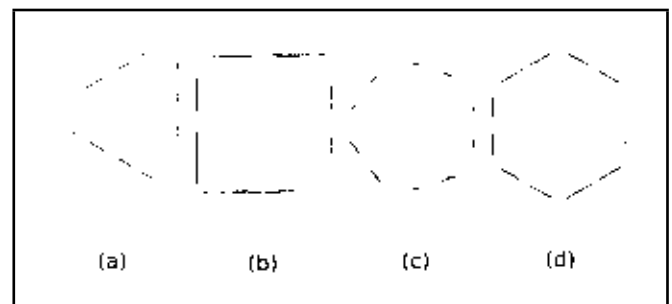


**Figure 1.** (a) Rounded triangular plate. From outside,  $\alpha = 0, 0.01, 0.05, 0.2, 0.5, 1$ . (b) Rounded square plate. From outside,  $\alpha = 0, 0.01, 0.05, 0.15, 0.3, 0.6, 1$ . (c) Rounded pentagonal plate. From outside,  $\alpha = 0, 0.05, 0.2, 0.5, 1$ . (d) Rounded hexagonal plate. From outside,  $\alpha = 0, 0.05, 0.2, 1$ .

is briefly described as follows: Let all lengths be normalized by the radius of the inscribing circle of the polygon; for a rounded equilateral triangular plate we set

$$H = \alpha(1 - x^2 - y^2) + (1 - \alpha)(1 - x) \left[ \left(1 + \frac{x}{2}\right)^2 - \frac{3}{4}y^2 \right] = 0; \quad (1)$$

where  $\alpha = 0$  is an equilateral triangle of edge length  $2\sqrt{3}$ , and  $\alpha = 1$  is a circle of radius one. The homotopy, as  $\alpha$  is increased from 0 to 1, gives a family of rounded triangles shown in Fig. 1(a). The maximum distance from the centroid is found to be

$$l = \frac{2}{1 + \sqrt{\alpha}}. \quad (2)$$

The degree of rounding is represented by the distance  $d$  to the original corner

$$d = 2 - l. \quad (3)$$

For a rounded square plate (Fig. 1(b)) we set

$$H = \alpha(1 - x^2 - y^2) + (1 - \alpha)(1 - x^2)(1 - y^2). \quad (4)$$

The maximum distance and degree of rounding are

$$l = \sqrt{\frac{2}{1 + \sqrt{\alpha}}}, d = \sqrt{2} - l. \quad (5)$$

The rounded regular pentagonal plate is shown in Fig. 1(c).

The boundary is given by

$$H = \alpha(1 - x^2 - y^2) + (1 - \alpha)(1 - x) \left[ \left( 1 + \frac{y_2 - y_1}{y_1 x_2 - y_2} x \right)^2 - \left( \frac{x_2 - 1}{y_1 x_2 - y_2} y \right)^2 \right] \times \left[ \left( 1 - \frac{x}{x_3} \right)^2 - \left( \frac{x_2 - x_3}{y_2 x_3} y \right)^2 \right]. \quad (6)$$

Here

$$y_1 = \tan(\pi/5), x_2 = -\sec(\pi/5) \cos(2\pi/5), \\ y_2 = \sec(\pi/5) \sin(2\pi/5), x_3 = -\sec(\pi/5). \quad (7)$$

There is no closed form solution for the maximum distance  $l$ . For each  $\alpha$  we set  $y = 0$  in  $H = 0$ . The smallest root is  $x = -l$ . Then

$$d = \sec(\pi/5) - l. \quad (8)$$

Fig. 1(d) shows the rounded regular hexagonal plate given by

$$H = \alpha(1 - x^2 - y^2) + (1 - \alpha)(1 - x^2) \cdot \left[ \left( 1 + \frac{x}{2} \right)^2 - \frac{3}{4} y^2 \right] \left[ \left( 1 - \frac{x}{2} \right)^2 - \frac{3}{4} y^2 \right]. \quad (9)$$

We find

$$l = \frac{1}{3} \sqrt{\frac{12 - 4\alpha - 4\sqrt{\alpha(3 + \alpha)}}{1 - \alpha}}, \quad d = \frac{2}{\sqrt{3}} - l. \quad (10)$$

Rounded regular polygons of more than six sides can be described similarly, but there are not considered in this paper.

### 3. THE RITZ METHOD

The total energy functional for a thin, isotropic (Kirchhoff) vibrating plate is as in (11)<sup>17,18</sup>

Here  $\rho$  is the density,  $h$  is the thickness,  $\omega$  is the frequency,  $w$  is the deflection,  $D$  is the flexural rigidity,  $\nu$  is the Poisson ratio ( $\nu = 0.3$  in all our computations), and  $\Omega$  is the domain with boundary  $S$  of the plate. The last integral is the work done on the boundary, where  $\hat{M}_n$  is the applied moment,  $\hat{V}_n$  is the applied edge force per length,  $n$  is the unit normal to the boundary and  $s$  is the unit tangent. The minimization of  $E$  is equivalent of setting its variation to zero. From Eq. (11), after some work, see (12).

In (13) and (14), where  $k = \omega L^2 \sqrt{\rho h / D}$  is the normalized frequency, and  $n_x, n_y$  are the direction normals. Since  $\delta w$  is arbitrary in the interior, we recover the governing plate equation

$$\nabla^4 w - k^2 w = 0. \quad (15)$$

For completely free boundaries,  $M_n = \hat{M}_n = 0$  and  $V_n = \hat{V}_n = 0$ . Thus the displacement  $w$  and its normal derivative should be arbitrary on the edges. Solving Eq. (15) is equivalent to minimizing Eq. (11) with the line integral in Eq. (11) set to zero.

For the Ritz method, we express the deflection in terms of a linear sum of Ritz functions taken as integer powers of  $x$  and

$y$ . They are independent but need not be orthogonal. For the completely free plate, there are no constraints for Ritz functions. Since the polynomials are complete, the variational solution converges to the true solution as the number of terms  $N$  is increased. Let

$$w = \sum_{i=1}^N c_i \varphi_i(x, y); \quad (16)$$

where  $\varphi_i(x, y)$  are the Ritz functions and  $c_i$  are the weights to be determined.

Now Eq. (16) is substituted into Eq. (11) with the last boundary integral set to zero. In order to minimize  $E$ , a necessary condition is

$$\frac{\partial E}{\partial c_j} = 0, j = 1 \text{ to } N. \quad (17)$$

After some work, Eq. (17) reduces to

$$\sum_{i=1}^N (A_{ji} - k^2 B_{ji}) c_i = 0, j = 1 \text{ to } N; \quad (18)$$

Here

$$A_{ji} = A_{ji} = \iint_{\Omega} [\varphi_{ixx} \varphi_{jxx} + \varphi_{iyy} \varphi_{jyy} + 2(1 - \nu) \varphi_{ixy} \varphi_{jxy} + \nu(\varphi_{ixx} \varphi_{jyy} + \varphi_{jxx} \varphi_{iyy})] dx dy; \quad (19)$$

$$B_{ji} = B_{ij} = \iint_{\Omega} \varphi_i \varphi_j dx dy. \quad (20)$$

Equation (18) is a set of linear homogeneous algebraic equations. For non-trivial  $c_i$ , the determinant of the coefficient matrix is set to zero

$$|A_{ji} - k^2 B_{ji}| = 0. \quad (21)$$

This is a characteristic equation for the eigenvalue  $k^2$ . A simple bisection algorithm on Eq. (21) yields the normalized frequencies  $k$ ; the first root would be the first frequency, the second root the second frequency, and so forth. Notice that the area integrals can be performed once and for all, i.e. increasing  $N$  would not affect the previously calculated integrals.

Also, depending on the geometry, we need not take all possible polynomial powers. For plates with an odd number of sides, the vibration modes can be either even in  $y$  or odd in  $y$ . Set

$$\{\varphi_i\} = q\{1, x, x^2, y^2, x^3, xy^2, x^4, x^2y^2, y^4, x^5, x^3y^2, y^4, x^6, x^4y^2, x^2y^4, y^4, \dots\}. \quad (22)$$

For modes even in  $y$ , let  $q = 1$ ; for modes odd in  $y$ , let  $q = y$ . For plates with an even number of sides (or the circle), the modes can be symmetric (even) in both  $x$  and  $y$  (SS mode), anti-symmetric in both  $x$  and  $y$  (AA mode), symmetric in  $x$  and anti-symmetric in  $y$  (SA mode), and anti-symmetric in  $x$  and symmetric in  $y$  (AS mode). Let

$$\{\varphi_i\} = q\{1, x^2, y^2, x^4, x^2y^2, y^4, x^6, x^4y^2, x^2y^4, y^4, x^8, x^6y^2, x^4y^4, x^2y^6, y^8, \dots\}. \quad (23)$$



$$E = \frac{1}{2} \iint_{\Omega} D \left\{ \left( \frac{\partial^2 w}{\partial x^2} + \frac{\partial^2 w}{\partial y^2} \right)^2 + 2(1-\nu) \left[ \left( \frac{\partial^2 w}{\partial x \partial y} \right)^2 - \frac{\partial^2 w}{\partial x^2} \frac{\partial^2 w}{\partial y^2} \right] \right\} dx dy - \frac{\rho h}{2} \omega^2 \iint_{\Omega} w^2 dx dy + \oint_S \left[ \hat{M}_n \frac{\partial w}{\partial n} - \hat{V}_n w \right] ds; \quad (11)$$

$$\delta E = D \iint_{\Omega} (\nabla^4 w - k^4 w) \delta w dx dy + \oint_S (M_n - \hat{M}_n) \delta \left( \frac{\partial w}{\partial n} \right) ds - \oint_S (V_n - \hat{V}_n) \delta w ds = 0; \quad (12)$$

$$M_n = -D \left\{ (1-\nu) \left[ \frac{\partial^2 w}{\partial x^2} n_x^2 + 2 \frac{\partial^2 w}{\partial x \partial y} n_x n_y + \frac{\partial^2 w}{\partial y^2} n_y^2 \right] + \nu \nabla^2 w \right\}; \quad (13)$$

$$V_n = D \left\{ (1-\nu) \frac{\partial}{\partial s} \left[ \left( \frac{\partial^2 w}{\partial x^2} - \frac{\partial^2 w}{\partial y^2} \right) n_x n_y - \frac{\partial^2 w}{\partial x \partial y} (n_x^2 - n_y^2) \right] - \left( \frac{\partial^3 w}{\partial x^3} + \frac{\partial^3 w}{\partial x \partial y^2} \right) n_x - \left( \frac{\partial^3 w}{\partial y^3} + \frac{\partial^3 w}{\partial y \partial x^2} \right) n_y \right\}; \quad (14)$$

Here  $q = 1, xy, y, x$  for the SS, AA, SA, and AS modes respectively. The number of terms  $N$  taken includes the highest homogeneous powers.

Table 1 shows some typical convergence rates. It is seen that for the even number of sides, including the circle,  $N = 28$  is adequate, while for the odd number of sides,  $N = 35$  is adequate for a five-figure accuracy. Table 2 shows a comparison with known results. The frequency for the free circular plate has an exact formula:<sup>3</sup>

$$\left\{ k^{3/2} I_n'(\sqrt{k}) - (1-\nu)n^2 \left[ \sqrt{k} I_n'(\sqrt{k}) - I_n(\sqrt{k}) \right] \right\} \times \left\{ k J_n(\sqrt{k}) + (1-\nu) \left[ \sqrt{k} J_n'(\sqrt{k}) - n^2 J_n(\sqrt{k}) \right] \right\} - \left\{ k^{3/2} J_n'(\sqrt{k}) + (1-\nu)n^2 \left[ \sqrt{k} J_n'(\sqrt{k}) - J_n(\sqrt{k}) \right] \right\} \times \left\{ k I_n(\sqrt{k}) - (1-\nu) \left[ \sqrt{k} I_n'(\sqrt{k}) - n^2 I_n(\sqrt{k}) \right] \right\} = 0; \quad (24)$$

where  $J$  and  $I$  are Bessel functions and modified Bessel functions, respectively. Our Ritz results for the circle are identical to the exact solution. The results for the square are very close to those of Mochida and Ilanko<sup>14</sup> (using finite differences), and the equilateral triangle results are very close to Leissa and Jaber.<sup>15</sup>

After the frequencies are determined, the mode shapes can be obtained from Eq. (18), using an arbitrary amplitude, say  $c_1 = 1$ , and solving for the other weights.

### 4. RESULTS

Table 3 shows the first five frequencies for the rounded triangular plate.  $\alpha = 0$  is the equilateral triangle, and  $\alpha = 1$  is the circle. Tables 4-6 show the first five frequencies for the rounded square plate, rounded pentagonal plate, and rounded hexagonal plate. We note that although some modes are different, the frequencies are same (up to some numerical error

**Table 1.** Typical convergence rates of the frequency. Parentheses indicate the number of terms used.

Circle 3 <sup>rd</sup> mode	Square 2 <sup>nd</sup> mode	Triangle 2 <sup>nd</sup> mode	Pentagon 1 <sup>st</sup> mode
9.1265 (6)	4.9436 (6)	3.0499 (6)	4.5318 (6)
9.0035 (10)	4.8993 (10)	3.0276 (9)	4.5275 (9)
9.0031 (15)	4.8992 (15)	3.0072 (12)	4.5158 (12)
9.0031 (21)	4.8990 (21)	3.0060 (16)	4.4829 (16)
	4.8990 (28)	3.0052 (20)	4.4798 (20)
		3.0052 (25)	4.4798 (25)
			4.4797 (30)
			4.4797 (35)

**Table 2.** Comparison of the first four frequencies. Asterisks denote the exact solution from Eq. (17), square brackets from Mochida and Ilanko,<sup>14</sup> flower brackets from Leissa,<sup>11</sup> and parentheses from Leissa and Jaber.<sup>15</sup>

Circle	Square	Equilateral triangle
5.3583 5.3583*	3.3671 [3.368] {3.372}	2.8565 (2.8566)
9.0031 9.0031*	4.8990 [4.900] {4.947}	3.0051 (3.0052)
12.439 12.439*	6.0676 [6.068] {6.108}	7.0569 (7.0569)
20.475 20.475*	8.7004 [8.700] {8.756}	13.521

in the fifth digit). The means that the modes could be linearly superposed; for example, the first and second modes of the pentagonal and hexagonal plates, and also the fourth and fifth modes of the pentagonal plate could be linearly superposed. Due to symmetry in both  $x$  and  $y$  directions, the fourth frequency or the fifth frequency of the square plate represent both AS or SA modes.

Most interesting is the evolution of the mode shapes as rounding is increased. Figure 2 shows the mode shapes (nodal lines) of the rounded triangular plate. The top row shows the modes corresponding to the first (fundamental) frequency, and the second row the second frequency, and so forth. It is ob-

**Table 4.** The first five frequencies of the free rounded square plate. The mode shape characteristics are indicated by subscripts. ASA means either AS or SA. The degree of rounding  $d$  is in parentheses.

$\alpha = 0$ (0)	$\alpha = 0.01$ (0.0658)	$\alpha = 0.05$ (0.1357)	$\alpha = 0.15$ (0.2134)	$\alpha = 0.3$ (0.2775)	$\alpha = 0.6$ (0.3526)	$\alpha = 1$ (0.4142)
3.3671 <sub>AA</sub>	3.4699 <sub>AA</sub>	3.6913 <sub>AA</sub>	4.0302 <sub>AA</sub>	4.3775 <sub>AA</sub>	4.8721 <sub>AA</sub>	5.3583 <sub>AA</sub>
4.8990 <sub>SS</sub>	4.9097 <sub>SS</sub>	4.9466 <sub>SS</sub>	5.0202 <sub>SS</sub>	5.1058 <sub>SS</sub>	5.2337 <sub>SS</sub>	5.3583 <sub>SS</sub>
6.0676 <sub>SS</sub>	6.2637 <sub>SS</sub>	6.6632 <sub>SS</sub>	7.2333 <sub>SS</sub>	7.7686 <sub>SS</sub>	8.4426 <sub>SS</sub>	9.0031 <sub>SS</sub>
8.7003 <sub>ASA</sub>	8.9515 <sub>ASA</sub>	9.4507 <sub>ASA</sub>	10.156 <sub>ASA</sub>	10.823 <sub>ASA</sub>	11.687 <sub>ASA</sub>	12.439 <sub>ASA</sub>
15.274 <sub>ASA</sub>	15.562 <sub>ASA</sub>	16.167 <sub>ASA</sub>	17.085 <sub>ASA</sub>	18.009 <sub>ASA</sub>	19.282 <sub>ASA</sub>	20.475 <sub>ASA</sub>

**Table 3.** The first five frequencies of the free rounded triangular plate. Subscript A indicates mode shape anti-symmetric with respect to  $y$ , and subscript S indicates symmetric with respect to  $y$ . The degree of rounding  $d$  is in parentheses.

$\alpha = 0$ (0)	$\alpha = 0.01$ (0.1818)	$\alpha = 0.05$ (0.3655)	$\alpha = 0.2$ (0.6180)	$\alpha = 0.5$ (0.8284)	$\alpha = 1$ (1)
2.8565 <sub>S</sub>	3.1356 <sub>S</sub>	3.3913 <sub>S</sub>	3.9212 <sub>S</sub>	4.5838 <sub>S</sub>	5.3583 <sub>S</sub>
3.0051 <sub>S</sub>	3.1360 <sub>A</sub>	3.3913 <sub>A</sub>	3.9212 <sub>A</sub>	4.5838 <sub>A</sub>	5.3583 <sub>A</sub>
3.0051 <sub>A</sub>	3.1601 <sub>S</sub>	3.7869 <sub>S</sub>	5.2141 <sub>S</sub>	7.1317 <sub>S</sub>	9.0031 <sub>S</sub>
7.0569 <sub>A</sub>	7.7653 <sub>A</sub>	8.1649 <sub>A</sub>	9.2045 <sub>A</sub>	10.663 <sub>A</sub>	12.439 <sub>A</sub>
7.0573 <sub>S</sub>	7.7695 <sub>S</sub>	9.1236 <sub>S</sub>	11.000 <sub>S</sub>	11.378 <sub>S</sub>	12.439 <sub>S</sub>

**Table 5.** First five frequencies of the free rounded pentagonal plate. Subscript A indicates mode shape anti-symmetric with respect to  $y$ , and subscript S indicates symmetric with respect to  $y$ . The degree of rounding  $d$  is in parentheses.

$\alpha = 0$ (0)	$\alpha = 0.05$ (0.0820)	$\alpha = 0.2$ (0.1418)	$\alpha = 0.5$ (0.1933)	$\alpha = 1$ (0.2361)
4.4797 <sub>A</sub>	4.6616 <sub>A</sub>	4.8960 <sub>A</sub>	5.1372 <sub>A</sub>	5.3586 <sub>A</sub>
4.4798 <sub>S</sub>	4.6616 <sub>S</sub>	4.8960 <sub>S</sub>	5.1372 <sub>S</sub>	5.3583 <sub>S</sub>
7.4238 <sub>S</sub>	7.7695 <sub>S</sub>	8.1984 <sub>S</sub>	8.6252 <sub>S</sub>	9.0031 <sub>S</sub>
10.597 <sub>A</sub>	10.943 <sub>A</sub>	11.418 <sub>A</sub>	11.937 <sub>A</sub>	12.439 <sub>A</sub>
10.598 <sub>S</sub>	10.943 <sub>S</sub>	11.418 <sub>S</sub>	11.947 <sub>S</sub>	12.439 <sub>S</sub>

vious that there are mode switches between the first column (equilateral triangle,  $\alpha = 0$ ) and the second column (rounded,  $\alpha = 0.01$ ). The first mode of  $\alpha = 0$  morphs to the third mode of  $\alpha = 0.01$ , The second mode of  $\alpha = 0$  turned into the first mode of  $\alpha = 0.01$ , and the third mode of  $\alpha = 0$  becomes the second mode of  $\alpha = 0.01$ . As the rounding is further increased, the modes gradually change into the circular modes. The higher modes also exhibit switching. The fourth modes of  $\alpha = 0$  and  $\alpha = 0.01$  disappear into the sixth mode (not shown) of  $\alpha = 0.05$ , and the sixth mode of  $\alpha = 0.01$  morphs into the fourth mode of  $\alpha = 0.05$ . Similarly there are also a mode switches between the fifth modes of  $\alpha = 0.05$  and  $\alpha = 0.2$ .

Figure 3 shows the mode shapes as the square is rounded to a circle. There are no mode switches for the first five frequen-

**Table 6.** The first five frequencies of the free rounded hexagonal plate. The mode shape characteristics are indicated by subscripts. The degree of rounding  $d$  is in parentheses.

$\alpha = 0$ (0)	$\alpha = 0.05$ (0.0604)	$\alpha = 0.2$ (0.1006)	$\alpha = 0.5$ (0.1318)	$\alpha = 1$ (0.1547)
4.7887 <sub>AA</sub>	4.9262 <sub>AA</sub>	5.0892 <sub>AA</sub>	5.2388 <sub>AA</sub>	5.3583 <sub>AA</sub>
4.7887 <sub>SS</sub>	4.9262 <sub>SS</sub>	5.0892 <sub>SS</sub>	5.2388 <sub>SS</sub>	5.3583 <sub>SS</sub>
8.0045 <sub>SS</sub>	8.2554 <sub>SS</sub>	8.5429 <sub>SS</sub>	8.8008 <sub>SS</sub>	9.0031 <sub>SS</sub>
10.228 <sub>SA</sub>	10.780 <sub>SA</sub>	11.409 <sub>SA</sub>	11.981 <sub>SA</sub>	12.439 <sub>SA</sub>
12.069 <sub>AS</sub>	12.127 <sub>AS</sub>	12.232 <sub>AS</sub>	12.345 <sub>AS</sub>	12.349 <sub>AS</sub>

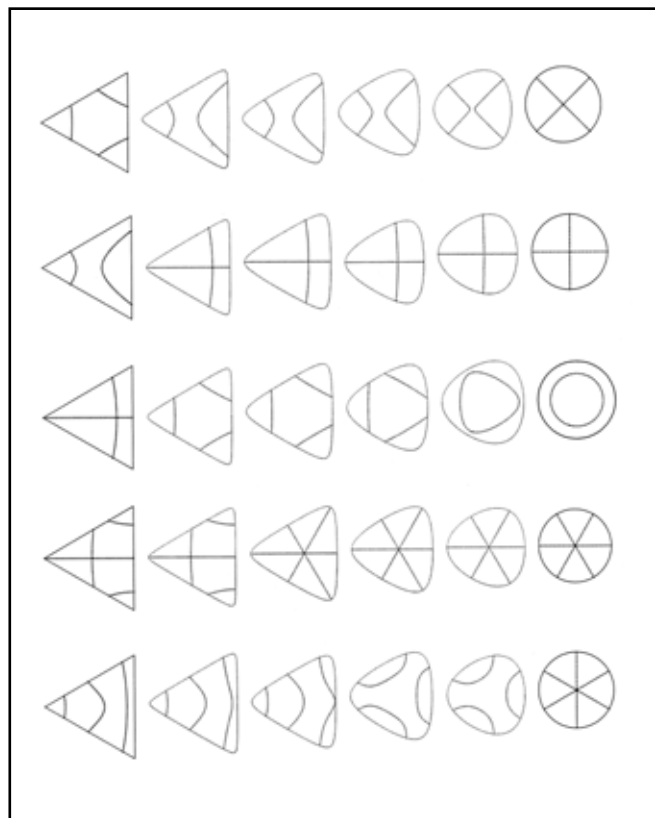


**Figure 2.** Mode shapes of the free rounded triangular plate. Fundamental modes are on top row, successive higher modes on lower rows. Columns from left:  $\alpha = 0, 0.01, 0.05, 0.2, 0.5, 1$ .

cies. Due to the orthotropic symmetry of the rounded square, the fourth and fifth modes all can self- rotate 90 degrees but are classified as the same mode.

Figures 4 and 5 show the mode shapes for the rounded pentagon and the rounded hexagon. There are no mode switches for the first five frequencies.

Mode switches can be explained in terms of the total energy  $E$ . For example, for a given geometry the fundamental vibration mode corresponds to the absolute minimum of  $E$ . Consider free rectangular plates where the aspect ratio changes from much less than unity to much larger than unity. The fundamental mode (with two nodal lines) will always be perpendicular to the long sides for minimum  $E$ , i.e. switches to another direction. We find no mode switches for polygons of four or more sides morphing into a circle. Perhaps the geometry is similar, but the triangle is very sensitive to the rounding of sharp corners. Even a small rounding of  $\alpha = 0.01$  (Fig. 1(a)) switches the fundamental mode.

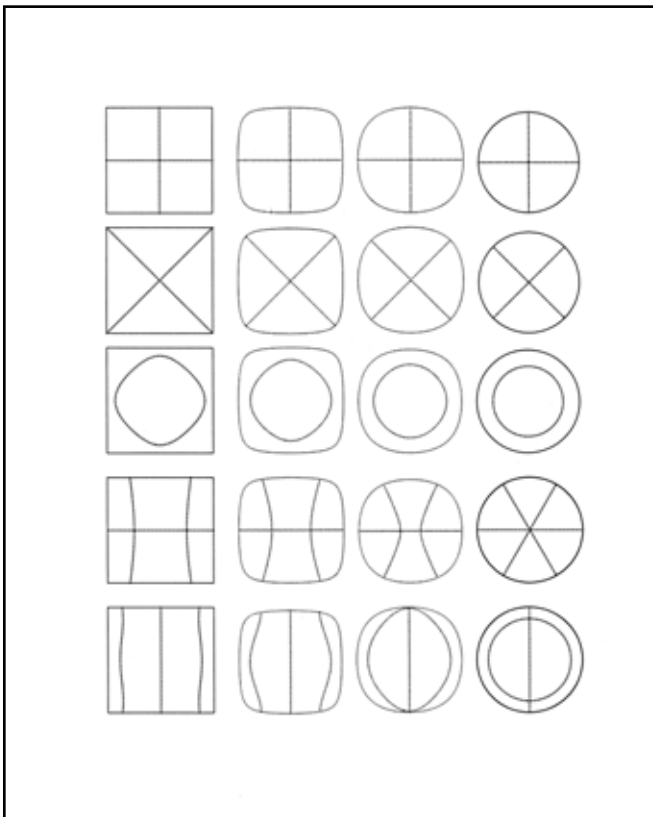


**Figure 3.** Mode shapes of the free rounded square plate. Fundamental modes are on top row, successive higher modes on lower rows. Columns from left:  $\alpha = 0, 0.15, 0.6, 1$ .

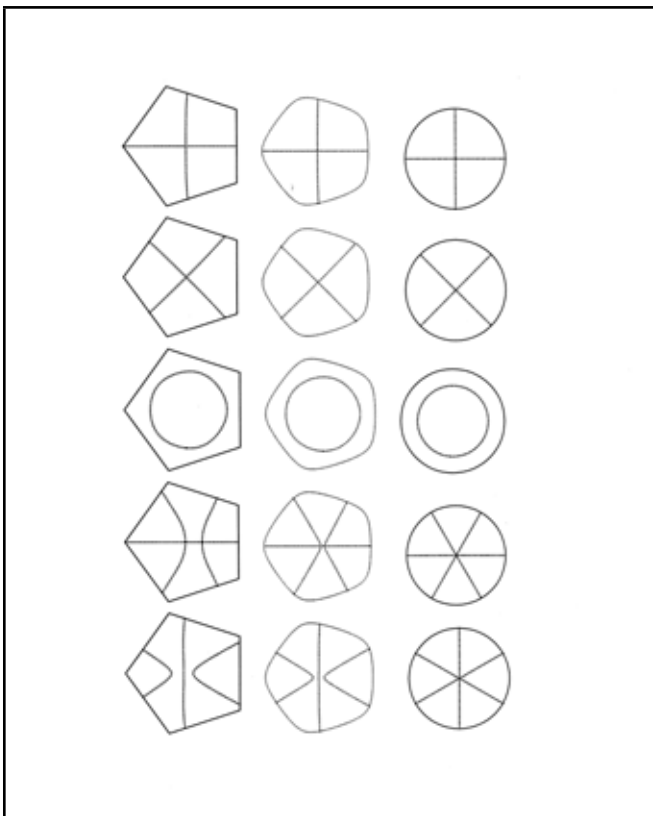


**Figure 4.** Mode shapes of the free rounded pentagonal plate. Fundamental modes are on top row, successive higher modes on lower rows. Columns from left:  $\alpha = 0, 0.2, 1$ .

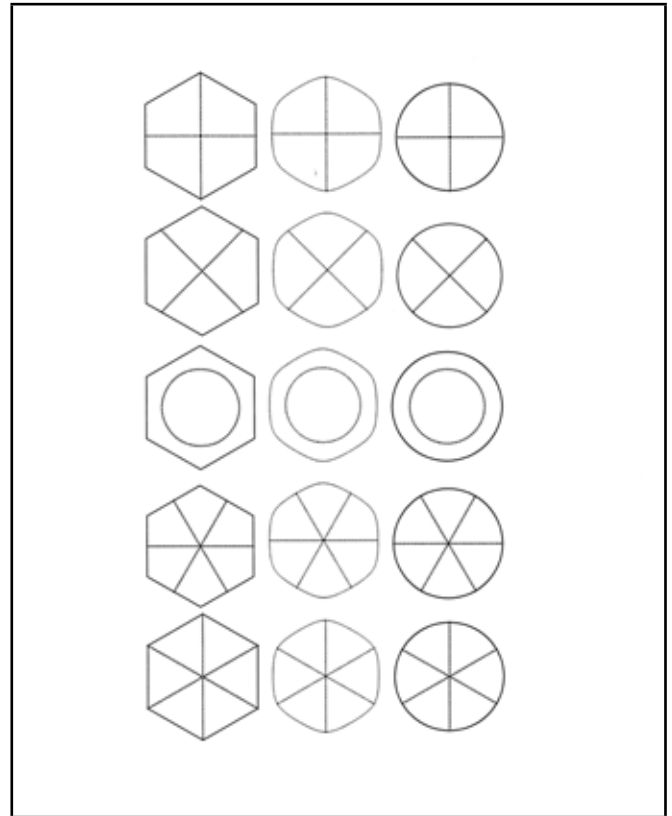


**Figure 5.** Mode shapes of the free rounded hexagonal plate. Fundamental modes are on top row, successive higher modes on lower rows. Columns from left:  $\alpha = 0, 0.2, 1$ .

## 5. DISCUSSION AND CONCLUSIONS

The present paper determines, for the first time, the natural frequencies and mode shapes for the vibration of completely free rounded polygonal plates. The computed results for the regular pentagonal and hexagonal plate are also new.

Using the recently introduced homotopy transformation,<sup>17</sup> rounded polygonal plates can be described analytically. The present plate problem however, is higher order and much more difficult than the previously studied membrane problem.<sup>17</sup>

The Ritz method (not Rayleigh-Ritz<sup>20</sup>) is accurate and efficient. For completely free plates, the tedious conditions of zero moment and zero edge forces are automatically satisfied. In comparison, all other methods including finite differences, finite elements, conformal mapping, superposition, etc. must deal with the boundary conditions and also the scaling problems at the small rounded corners. A further simplification is that, by classifying whether the mode shapes are symmetric or anti-symmetric with respect to the axes, the Ritz sequence is simplified, i.e. not all polynomial powers are needed.

Rounding of the polygonal corners increases the natural frequencies based on the radius of the inscribing circle. Our Tables 3-6 would be useful in the design of completely free plates, which model large space structures.

As rounding parameter  $\alpha$  increases, the plate gradually changes from a regular polygon to a circle. The vibration modes also morph to that of a circular plate. We find several mode switches for the rounded triangular plate, while the rounded square, pentagonal, hexagonal plates have no such mode switches, at least for the first five modes.

Different modes with the same frequency (and the same boundary) can be linearly superposed, creating a profusion of mode shapes, as evidenced by the vibration of a free square plate.<sup>1</sup> Again, by using symmetric or anti-symmetric mode properties, systematic classifications of the fundamental mode shapes are possible, such as those depicted in Figs. 3-5. Waller<sup>21</sup> experimentally found many of the mode shapes of regular polygons, but her classification scheme is more complicated than ours.

## REFERENCES

- <sup>1</sup> Leissa, A. W. *Vibration of Plates*, NASA, Washington D.C., (1969).
- <sup>2</sup> Blevins, R.D. *Formulas for Natural Frequency and Mode Shape*, Krieger, Florida, (1993).
- <sup>3</sup> Wang, C. Y. and Wang, C. M. *Structural Vibration- Exact Solutions for Strings, Membranes, Beams and Plates*. CRC Press, Boca Raton, Florida, (2013).
- <sup>4</sup> Conway, H. D. The bending, buckling and flexural vibration of simply supported polygonal plates by point-matching, *Journal of Applied Mechanics*, **28**, 288–291 (1961).
- <sup>5</sup> Shahady, P. A., Pasarelli, R., and Laura, P. A. A. Application of complex variable theory to the determination of the fundamental frequency of vibrating plates, *Journal of the Acoustical Society of America*, **42**, 806–809 (1967).
- <sup>6</sup> Irie, T., Yamada, G., and Umesato, K. Free vibration of regular polygonal plates with simply supported edges, *Journal of the Acoustical Society of America*, **69**(5), 1330–1336 (1981).
- <sup>7</sup> Liew, K. M., and Lam, K. Y. A set of orthogonal plate functions for flexural vibration of regular polygonal plates, *Journal of Vibration and Acoustics*, **113**, 182–186 (1991).
- <sup>8</sup> Ghazi, S. S. A., Barki, F. A. and Safwat, H. M. Free vibration of penta, hepta-gonal shaped plates, *Computers and Structures*, **62**(2) 395–407 (1997).
- <sup>9</sup> Duan, W. H., Wang, C. M., and Wang, C. Y. Modification of fundamental vibration modes of circular plates with free edges, *Journal of Sound and Vibration*, **317**, 709–715 (2008).
- <sup>10</sup> Wie, B. and Roithmayr, C. M., Attitude and orbit of a very large geostationary solar power satellite, *Journal of Guidance Control and Dynamics*, **28**, 439–451 (2005).
- <sup>11</sup> Leissa, A. W., The free vibration of rectangular plates, *Journal of Sound and Vibration*, **31**(3), 257–293 (1973).
- <sup>12</sup> Gorman, D. J., Free vibration analysis of the completely free rectangular plate by the method of superposition, *Journal of Sound and Vibration*, **57**, 437–447 (1978).
- <sup>13</sup> Behnke, H. and Mertins, U., Eigenwertschranken für das problem der frei schwingenden rechteckigen platte und untersuchungen zum ausweichphanomen, *Zeitschrift für angewandte Mathematik und Mechanik*, **75**, 343–363 (1995).
- <sup>14</sup> Mochida, Y. and Ilanko, S., Bounded natural frequencies of completely free rectangular plates, *Journal of Sound and Vibration*, **311**, 1–8 (2008).
- <sup>15</sup> Leissa, A. W. and Jaber, N. A. Vibrations of completely free triangular plates, *International Journal of Mechanical Sciences*, **34**(8) 605–616 (1992).
- <sup>16</sup> Qatu, M. S., Jaber, N. A. and Leissa, A. W. Natural frequencies for completely free trapezoidal plates, *Journal of Sound and Vibration*, **167**(1), 183–191 (1993).
- <sup>17</sup> Wang, C. Y., Fundamental frequencies of rounded polygonal membranes- A class of homotopy shapes, *Journal of Vibration and Acoustics*, **135**, 014501 (2013).
- <sup>18</sup> Timoshenko, S. and Woinowsky-Krieger, S. *Theory of Plates and Shells*, McGraw-Hill, New York, (1959).
- <sup>19</sup> Washizu, K. *Variational Methods in Elasticity and Plasticity*, Pergamon, Oxford, (1982).
- <sup>20</sup> Leissa, A. W. The historical basis of the Rayleigh and Ritz methods, *Journal of Sound and Vibration*, **287**, 961–978 (2005).
- <sup>21</sup> Waller, M. D. Vibrations of free plates: line symmetry; corresponding modes, *Proceedings of the Royal Society of London, Ser. A*, **211**, 265–276 (1952).

# About the Authors

---

**Umberto Berardi** is an Assistant Professor of Building Science at Ryerson University, Toronto. His researches concern the application of physics and sustainability principles to the built environment. His areas of expertise include green buildings, energy saving technologies, and architectural acoustics. He took an MSc degree in Building Engineering at the Politecnico di Bari (I), a MSc in Sound and Vibration at the ISVR of the University of Southampton (UK), and a PhD in “Product Development & Innovation Management” with a focus in “Building Engineering” at the Scuola Interpolitecnica (I). Umberto has an extensive publication record, which includes 50 peer-reviewed journal papers, and over 40 conference papers presented in 20 countries.



**Birgit Rasmussen** is Senior Researcher in the Construction and Health (CH) of the SBI Danish Building Research Institute. She has more than thirty years of experience in the field of building sound insulation. She has recently chaired the COST Action TU0901 “Integrating and Harmonizing Sound Insulation—Aspects in Sustainable Urban Housing Constructions”. She is also affiliated with The Faculty of Engineering and Science of the Aalborg University.

**Constantine M. Tarawneh** is a professor of mechanical engineering at The University of Texas-Pan American where he has worked since 2003. He obtained his MS and PhD degrees from The University of Nebraska-Lincoln in 1999 and 2003, respectively. He founded the University Transportation Center for Railway Safety in 2013 and serves as the Center Director. His various research and educational activities have resulted in about \$9.5 million in funding from industry and federal sources. He conducts a variety of railroad research with emphasis on bearing condition monitoring techniques. He received 22 teaching, mentoring, and research awards highlighted by the UT System Regents’ Outstanding Teaching Award in 2009. To date he has taught 24 different courses in his discipline.



**Rafael Maldonado** is currently Data Management Product Manager at ENSCO, Inc. where he has worked since 2012. He obtained his BS and MS degrees in mechanical engineering from The University of Texas-Pan American in 2010 and 2011, respectively. During his academic career at UTPA, Rafael worked as a research assistant exploring condition monitoring techniques of railroad bearings. In particular, his thesis was aimed at providing evidence through vibration monitoring techniques of the effect of vibration on bearing temperature. Rafael started at ENSCO as a mechanical engineer assisting in design and data analysis to improve track safety. Soon after, Rafael was promoted to research manager and oversaw various FRA funded research initiatives. He now serves as the data management lead where he is responsible for web-based products ranging from applications that carry out track inspections to data processing of autonomous track inspection systems.

**Arturo A. Fuentes** is a professor of mechanical engineering at The University of Texas-Pan American where he has worked since 2001. He obtained his MS and PhD degrees from Rice University in 1997 and 1999, respectively. He currently serves as the Mechanical Engineering Undergraduate Program Director at UTPA. Among his research interests are: engineering education, functionally graded materials, dynamic response analysis, and non-destructive evaluation.



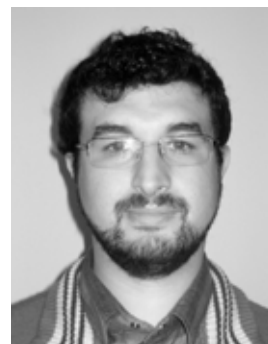
# About the Authors

---



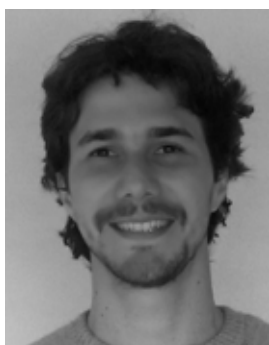
**Javier Kypuros** received a BSE in mechanical engineering from Princeton University in 1996. He later received an MSE and PhD in mechanical engineering in 1998 and 2001 from the University of Texas at Austin. Javier began his career at The University of Texas at El Paso in 2001 and later joined the faculty at The University of Texas-Pan American (UTPA) in 2002. He is currently a professor in the Mechanical Engineering Department and is associate dean for undergraduate affairs in the College of Engineering and Computer Science. He was awarded Faculty Excellence Awards by the College of Engineering and Computer Science at UTPA for teaching in 2011 and service in 2012 and was recognized by the University of Texas System with a Regents' Outstanding Teaching Award in 2014. His research interests include dynamic systems and controls, bond graphs, and vehicle systems.

**Fabián C. Tommasini** received the Dipl.-Ing. degree in information systems engineering from the National Technological University, Cordoba Regional Faculty, Argentina, in 2006, and his PhD degree in engineering science from the National University of Cordoba, Faculty of Exact, Physical and Natural Sciences, Argentina, in 2012. Since 2006 he has been working as a research assistant at the Center for Research and Transfer in Acoustics of National Technological University, Cordoba Regional Faculty. He is currently a postdoctoral fellow at Faculty of Mathematics, Astronomy, and Physics of the National University of Cordoba, Argentina. His research interests include binaural sound localization, signal processing, virtual auditory displays, and real-time applications for virtual reality. He is a member of the Argentine Acoustical Association (AdAA).



**Oscar A. Ramos** received the Dipl.-Ing. degree in electrical engineering from the National University of Cordoba, Faculty of Exact, Physical and Natural Sciences, Argentina, in 1975. He is an adjunct professor at the National Technological University, Cordoba, Argentina, and a Researcher of National Scientific and Technical Research Council (CONICET). He worked in various fields of acoustics at the Center for Research and Transfer in Acoustics of the National Technological University, Cordoba Regional Faculty, and since 2009 he has been the director. His main research interests include virtual acoustics, signal processing, and binaural sound localization. He is a member of the Argentine Acoustical Association (AdAA).

**Mercedes X. Hüg** studied psychology at the National University of Cordoba, Argentina, and received a BSc degree in 2000 and a PhD degree in 2011. She coordinated research projects at the Center for Research and Transfer in Acoustics, National Technological University, Cordoba Regional Faculty, Argentina. She is currently an assistant professor at the National University of Cordoba. Her research interests include sound localization, precedence effect, developmental psychoacoustics, and human echolocation. She is a member of the Argentine Behavioral Sciences Association (AACC).



**Fernando Bermejo** studied psychology at the National University of Cordoba, Argentina, and received a BSc degree in 2006 and a PhD degree in 2014. He is currently a postdoctoral fellow at the Center for Research and Transfer in Acoustics, National Technological University, Cordoba Regional Faculty, Argentina. Also, since 2009, he has been an assistant professor at the National University of Cordoba. His main research interests include psychoacoustics, sound localization, auditory perception, and sensory substitution systems. He is a member of the Argentine Behavioral Sciences Association (AACC).

**Raghavendra D. Naik** is currently a faculty member at Goa College of Engineering. He has completed his PhD in the field of nonlinear vibrations and stability in finite time. His research areas include nonlinear dynamics, stability of structures, and microsystems design. His current research focus is on perturbation methods to obtain approximate solutions to differential equations arising from problems in engineering. He is also interested in differential equations with fractional derivatives, coupled oscillators, delay differential equations, and nonlinear control theory.



**Pravin Singru** obtained his M. Tech. from IIT, Kharagpur and his PhD from Visvesvaraya National Institute of Technology, Nagpur. His doctoral thesis was on "Dynamic and Vibration Response of Pulleys of a Belt Drive." Prof. Singru has more than 21 years of teaching experience. He teaches courses in the areas of mechanics of solids, kinematics and dynamics of machines, and vibrations & MEMS. He has been guiding six research scholars for their research leading to their PhD degrees. He has published more than 29 research papers in international journals and 36 papers in national and international conferences. Prof. Singru is the coordinator of the National Center for MEMS Design.

**Cristina Castejón** is associate Professor at the Department of Mechanical Engineering of the University Carlos III, Madrid. She got her masters degree in industrial engineering in 1998 with laude mention and her PhD degree in industrial technologies at the University Carlos III in 2002. Her research interests cover aspects of mechanics of robots, mechanics of machinery, and the monitoring and diagnosis of rotary elements. She is a member of MAQLAB research group and Pedro Juan de Lastanosa Research Institute, both belonging to Carlos III University. Also, she belongs to AEIM (a Spanish mechanical engineering association) and IFToMM.



**María J. Gómez** collaborates as a researcher in the Department of Mechanical Engineering of the University Carlos III (Madrid). She obtained her masters degree in industrial engineering in 2008 with laude mention, a masters degree in machine and transports engineering in 2011 with laude mention, and her PhD degree in mechanical engineering at the University of Carlos III in 2014. Her areas of expertise are the diagnosis of rotating machines, vibration in rotating machinery, signal processing, biomechanics, and the mechanics of robots. She is member of MAQLAB research group that belongs to the University Carlos III.

# About the Authors

---



**Juan Carlos García-Prada** is Head Professor in the Department of Mechanical Engineering at the University Carlos III, Madrid. He obtained his masters degree in industrial engineering in 1985 at the Polytechnic of Madrid University and his PhD degree in mechanical engineering at The National Distance Education University (UNED) in 1991. His professional activities have been related to mechanism and machines cinematics and dynamics, vibration in rotating machinery, signal processing, and the mechanics of robots. He is member of MAQLAB research group, Pedro Juan de Lastanosa research institute, both belonging to Carlos III University. Also, he belongs to AEIM (a Spanish mechanical engineering association) and IFToMM.

**Alberto Ordoñez** has over ten years of experience in coordination, QC/QA, inspection, testing, expediting activities of components and parts of petroleum and energy industries, welding processes, witness of mechanicals & NDT tests, and expediting projects. He also has experience in factory and site acceptance tests (FAT & SAT) of gas and steam turbines, HRSG, pumps, pressure vessels, heat exchangers, and others. He is an NDT Inspector Level 2 (PT, MT, UT), mechanical vibration specialist, specialist in control and inspection of welding processes SAW, GMAW, SMAW, GTAW, and FCAW under ASME IX. Additionally, he is a researcher at the University Carlos III in mechanical vibrations on rotating machinery, predictive maintenance, defectology, and design of intelligent systems based on neural networks/wavelets and transform/mechanical vibration for defects detection and classification.



**Higinio Rubio Alonso** obtained his masters degree in industrial engineering at the National Distance Education University (UNED) and his PhD degree in industrial technologies at the University Carlos III of Madrid. Currently, he is an associate professor in the Department of Mechanical Engineering at the University Carlos III of Madrid. He has a wide array of experiences in teaching kinematics, dynamics, design, simulation, and maintenance of machines, with several teaching publications. His researching is focused in mechanical engineering and mechatronics, especially in the modelling and simulation of systems: mechanical elements, support system, railway equipment, and mechatronic systems. Additionally, he has a wide knowledge of analysis of vibrations and machine maintenance.

**Ruqiang Mou** received his BSc degree from Sichuan University, Chengdu, China, in 2013, and he will receive his MS degree from Sichuan University in 2016 in mechanical and electronic engineering. He is currently a student in mechanical and electronic engineering..





**Li Hou** received his MS degree from Chongqing University, Chongqing, China in 1992 and his PhD degree from Sichuan University in 2000. He is currently a professor and PhD supervisor at Sichuan University. His research interests cover mechanical transmission, intelligent control and embedded systems, and CAD/CAPP/CAM/PMD.



**Yiqiang Jiang** received his BE in internal combustion engineering in 2000 from Chongqing University, Chongqing, China, and he will receive a DE in mechatronic engineering in 2015 from Sichuan University, Chengdu, Sichuan, China. He is currently an assistant professor of mechanical engineering in the Mechatronics Department at Leshan Vocational & Technical College in Leshan, Sichuan, China. His interests include agricultural mechanical engineering and gear transmission; he has published and presented papers in these area.

**Yong Zhao** received his BE in power engineering in 1993 from Southwest Jiaotong University, Chengdu, Sichuan, China. He is currently an assistant professor of mechanical engineering in the Mechatronics Department at Leshan Vocational & Technical College in Leshan, Sichuan, China. His interests include power engineering and agricultural mechanical engineering, and he has published and presented papers in these area.



**Yongqiao Wei** received his BSc degree from Sichuan University, Chengdu, China in 2012, and he will receive his MS degree from Sichuan University in 2015 in mechanical design and theory. He is currently a student in mechanical design and theory at Sichuan University.

**C. Y. Wang** has a bachelor's degree from Taiwan University and a PhD from Massachusetts Institute of Technology. He is currently a professor in the Departments of Mathematics and Mechanical Engineering at Michigan State University. He has published about 480 papers in fluid, solid, and biomechanics and co-authored two books: Exact Solutions for Buckling of Structural Members and Structural Vibration- Exact Solutions for Strings, Membranes, Beams and Plates.

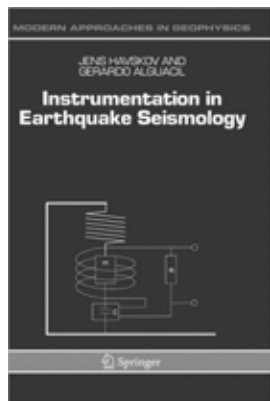


# Book Reviews

## Instrumentation in Earthquake Seismology

By: J. Havskov and G. Alguacil Springer  
Revised print 2010  
Hardcover, XII, 360 p., CD-ROM contains software  
ISBN 78-1-4020-2968-4  
Price: US \$139

Seismology is the scientific study of earthquakes and the propagation of elastic waves through the Earth. A recording of earth motion as a function of time is called a seismogram. The book is intended for seismologists and technicians working with seismological instruments, most of whom, apparently, don't know much about the instruments they use. Either way, it is good to know more about the measuring instruments than just what they read-out. For those of us who know "vibrations," we know the majority of measurements are in the 1 Hz to perhaps 20,000 Hz range. Seismologists measure from about 0.0001 Hz to maybe 1,000 Hz.



This well-illustrated book has ten chapters followed by a lengthy appendix, a section on references, and a thorough index.

Chapter 1 (The Introduction) presents the issues involved in measuring the motion of the Earth from extremely low amplitudes and frequencies, to the extraneous noise, to the relationship between the instrument readout, to the actual motion of the ground. The hope is that this book will allow seismologists to have an understanding of seismic data that accurately reflect ground motion.

Chapter 2 (Seismic Sensors) discusses the transducer, i.e. the device converting motion to some signal that can be read and is the key to accurate and precise data collection. The fact that the sensor is moving with the ground motion also might require the use of an inertial sensor that detects acceleration. The chapter discusses the basic single degree-of-freedom system (mass, spring, dashpot) and the effect of excitation frequency on gain. There is a very readable, yet mathematical, discussion of the theory of the inertial acceleration sensor and the velocity sensor. Additional topics include other types of sensors, including MEMS (micro electro-mechanical systems), feedback systems, and self-noise. Construction and figures describing the types of sensors makes for an interesting and helpful reading.

Chapter 3 (Seismic Noise) discusses instrumentation and external noise, caused by "normal" ground motion. This latter noise, usually higher than instrument noise, is caused by human activities like traffic, wind and ocean motions, and running water.

Chapter 4 (Analog to Digital Converter) provides a rather thorough but brief discussion of A/D conversion to help those unfamiliar understand the complications and limitations of signal processing.

Chapter 5 (Seismic Recorders) explains analog (strip-chart type) and digital recorders. It goes from the basics, that amplitude and time must be recorded simultaneously, to the more complex, involving differential outputs and filtering. The chapter describes field and station recorders with many illustrations.

Chapter 6 (Correction for Instrument Response) addresses the fact that over a frequency range, the output/input ratio may not be constant even for a single degree-of-freedom system. An introduction to the Fourier analysis is included starting from a rather mathematical approach to a combination of responses and, finally, the corrections for instrument response.

Chapter 7 (Seismic Stations) presents what is necessary to equip and install a permanent station, from mounting and orienting the sen-

sor(s), to remote powering, to recording, and maybe transmitting, the output.

Chapter 8 (Seismic Networks) shows how seismic networks are needed if the location of the event is needed. While one sensor will give the magnitude (and direction) at the sensor location, several sensors are needed to determine origin. Communication between and among sensors using the internet is also addressed, and these numerous sensors can be located around the world.

Chapter 9 (Seismic Arrays) discusses how seismic arrays "are a set of sensors with common response functions. . . with the aim of obtaining a coherent spatial sampling of the seismic wavefield in time." This chapter addresses the advantages of multiple sensor locations, where signals are very similar except for local uncorrelated noise and a time (or phase) shift occurs.

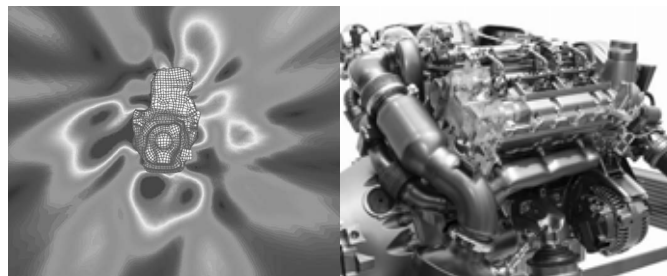
Chapter 10 (Calibration and Testing) addresses what is necessary for field verification of correct operation and true calibration where output is compared to a traceable standard. This chapter is the most useful; while not meant as a complete course on the subject, it will give the reader a concept of what is needed to assure precise instrument output, and therefore knowledge, of the actual ground motion.

Appendix (Basic Electronics) provides a short course (about 28 pages) on electronics: voltage, current, passive and active components, amplifiers, filters, logics, and a practical example on calibration.

Overall, the book is a nice read and is a practical tool with only the amount of theory needed to understand the basic principles. The many illustrations help the reader understand the well-written text. The book answers many practical problems and is highly recommended.

Engineers for Change, Inc.

**Richard J. Peppin**  
Engineers for Change, Inc.



# Actran™

Powerful Acoustic Simulation Software

- Acoustic radiation
- Adaptive meshing technology
- Duct acoustics
- Coupled vibroacoustics
- Absorbing materials
- NHV of trimmed vehicle body
- Aeroacoustics
- Fan noise
- Acoustic fatigue
- Interface with MSC Software solutions (MSC Nastran, Adams, ...)

Learn more on [www.fft.be](http://www.fft.be)



Free Field Technologies, MSC Software Company

$a+r+t=$



**WORK IT OUT.**



**Cadna A<sup>®</sup>**  
State-of-the-art  
noise prediction software



- CNOSSOS-EU (Common Noise Assessment Methods) for industry, road, rail and aircraft noise
- New calculation protocol, display third octave values
- New export functions to ArcView shape format
- Enhanced ObjectTree management

 **DataKustik**

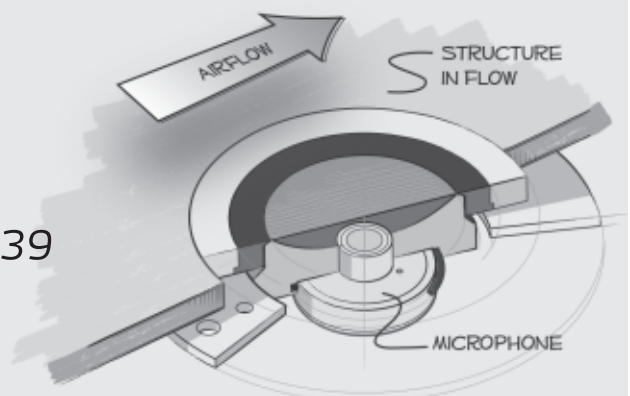
**DataKustik GmbH**  
Gewerbering 5  
86926 Greifenberg

Phone: +49 8192 93308 0  
info@datakustik.com  
www.datakustik.com

# Aeroacoustic at ICSV22

See our unique offerings at booth #B39

**G.R.A.S.**  
SOUND & VIBRATION



We make microphones

**gras.dk**

35 YEARS OF EXPERIENCE IN INDUSTRIAL AND CIVIL SOUNDPROOFING

35 YEARS OF EXPERIENCE IN INDUSTRIAL AND CIVIL SOUNDPROOFING

35 YEARS OF EXPERIENCE IN INDUSTRIAL AND CIVIL SOUNDPROOFING



Via Lago di Levico, 7 · 36015 Schio (VI) · ITALY · tel. +39 0445 575 669 · e-mail info@marvinacustica.it · www.marvinacustica.it



**Maximum quality, minimum price**

Meggitt performance, accuracy and reliability - at the low price and short lead times demanded by today's test professionals

New general purpose Isotron® (IEPE) accelerometers

- › Multiple sensitivities
- › Single- or tri-axial
- › Mounting and connector options

Endevco® test and measurement product line

www.meggittsensingsystems.com • www.meggitt.com



**Odeon** Room Acoustics Software

... brings measurements and simulations together

www.odeon.dk

**SIEMENS**

**LMS SCADAS XS**

On-the-spot noise and vibration testing.

Designed to support fast, on-the-spot noise and vibration testing, the LMS SCADAS XS is geared towards flexibility and reliability.

Small enough to slip into a pocket, it works as a standalone recorder, with a tablet over Wi-Fi, or connected to a PC.

For more information, please visit [siemens.com/plm/lms](http://siemens.com/plm/lms)

Realize innovation.